Fermilab FERMILAB-THESIS-1997-22

Search for the B_c Meson at CDF.

by

Prem P Singh

B.Sc., Bombay University, 1987
M.Sc., Bombay University, 1989

Submitted to the Graduate Faculty of
Department of Physics and Astronomy in partial fulfillment
of the requirement for the degree of
Doctor of Philosophy

University of Pittsburgh
1997

UNIVERSITY OF PITTSBURGH

FACULTY OF ARTS AND SCIENCES

This dissertation was presented

by

Prem P. Singh

It was defended on

January 7, 1997

and approved by

Prof. Paul F. Shepard, Department of Physics and Astronomy

Prof. Eugene Engels Jr., Department of Physics and Astronomy

Prof. Raymond Willey, Department of Physics and Astronomy

Prof. Jeremy Levy, Department of Physics and Astronomy

Prof. David Pratt, Department of Chemistry

sd. Paul F. Shepard

Committee Chairperson.

SEARCH FOR THE B_c MESON AT CDF
Prem P Singh, PhD
University of Pittsburgh, 1997

The bottom-charm meson B_c is predicted by the Standard Model with an expected mass in the range of 6.2 to 6.3 GeV/c^2. We report on the search for the B_c meson in the inclusive decay channel $J/\psi + \mu + X$ in $p\bar{p}$ collisions at $\sqrt{s} = 1.8$ TeV for an integrated luminosity of 110 pb^{-1}. An upper limit on the cross-section times branching ratio of $B_c \rightarrow J/\psi + \mu + X$ relative to $B_u \rightarrow J/\psi K$ as a function of assumed B_c lifetime is presented.

Acknowledgment

I would like to thank my Advisors Prof. Eugene Engels Jr. and Prof. Paul F. Shepard for their support and guidance during my graduate studies. Rajesh Dalal, D. K. Sinha and Prof. A. P. Sathe were my teachers during my high school and undergraduate years. They stimulated my interest in physics and I am ever thankful to them. During the graduate studies I learnt a lot from Todd Huffman, Joe Incandela, J. C. Yun and Joe Boudreau, their guidance and support was crucial to my research. I express sincere gratitude to the members of the CDF collaboration and the technical support staff at Fermilab and the member universities.

I would also like to thank my friends J. Suzuki, D. Stuart, E. Kajfasz, S. Chopra, M. Bhattacharjee, B. Bhattacharjee, B. Chaudhary, K. Connally, S. Ramchandran, Balamurali V, V. Bhatnagar, H. Singh, H. Shankar, A. Kotwal, B. C. Dave, A Barodawala, S. Das and S. Muzumdar for their help and support.

I am specially grateful to the taxpayers of the Republic of India and the United States of America. It is their money which supports education and research. Last but not the least I am thankful to my parents and my wife for their continued support throughout my graduate career.

I dedicate this thesis to my parents; Nirmala Devi and Bharat Singh, and my teachers; Rajesh Dalal and Prof. A.P. Sathe.

TABLE OF CONTENTS

LIST OF TABLES

LIST OF FIGURES

CHAPTER 1.

The B_c Meson

A. Introduction

The B_c meson is the bound state of a b and a c quark and is the last of the family of the B mesons yet to be discovered. It is expected to be produced in $p\bar{p}$ collisions. The Tevatron at Fermilab is the highest energy $p\bar{p}$ collider in the world, and presents an energy regime which makes it a natural place to look for the B_c meson. The B_c meson is made up of a heavy quark and an anti quark of differing flavors. This results in specific production mechanisms and spectroscopy, which allow one to sharpen the quantitative understanding of the QCD dynamics and the study of the parameters of the electroweak theory.

The B_c spectrum can be calculated using non-relativistic potential models (Ref. [1] to [5]), or the QCD sum rules (Ref. [6] to [14]). Studies of the B_c meson can be used to test the self-consistency of the potential models and the QCD sum rules. Its study will also help improve the quantitative understanding of the quark model and the QCD sum rules.

The B_c meson lies between the charmonium and the bottomonium systems both in terms of its mass and the typical separation distance between the two heavy quarks. In the region of the average distances in the $c\bar{c}$ and the $b\bar{b}$ systems the quark potential model has simple scaling properties [4, 15, 16], which states that the kinetic energy of the heavy quarks is almost a constant value and is independent of the quark flavors and the excitation levels in the heavy quarkonium system. This has been studied extensively for the $c\bar{c}$ and the $b\bar{b}$ systems and can be used to study the B_c system.

B. Mass of the B_c

1. The B_c mass from the Potential Model

The B_c mass can be calculated using the framework of the phenomenological potential models for non-relativistic heavy quarks. The masses of the charmonium and the bottomonium systems have been studied experimentally in detail and are described quite accurately in the framework of the potential models. To describe the B_c system, it would be advantageous to use the potentials whose parameters do not depend on the flavor of the constituent quarks of the system. This could be done by using a model which describes both the charmonium and the bottomonium systems accurately. This will not require the interpolation of the parameters of the model, which are obtained experimentally from the charmonium and the bottomonium systems to an intermediate region of the B_c system. Eichten, et al., in Ref. [17], consider four functional forms of the potentials that give reasonable accounts of the $c\bar{c}$ and the $b\bar{b}$ spectra. These are (1) a QCD motivated potential [18] given by Buchmüller and Tye [6], (2) a power law potential [4], (3) a logarithmic potential [5] and (4) a Coulomb plus linear potential [19].

The Schrödinger equation for each of the potentials is solved to determine the position of the $1S$ center of gravity for the $c\bar{c}$, $c\bar{b}$ and the $b\bar{b}$ bound states. The ${}^3S_1 -{}^1 S_0$ splitting of the ground state is given by Equation 1-1 [15]:

$$M({}^3S_1) - M({}^1S_0) = \frac{32\pi\alpha_s\Psi(0)^2}{9m_i m_j} \tag{1-1}$$

The strong coupling constant for each potential is fixed by the hyperfine splitting observed in the charmonium family [20],

$$M(J/\psi) - M(\eta_c) = 117 \text{ MeV/c}^2 \tag{1-2}$$

The variation of α_s with momentum is neglected and the splitting of the $c\bar{b}$ and $b\bar{b}$ is scaled from the charmonium value (Equation 1-2). Table 1-1 (taken from Ref. [17]) lists the resulting vector and pseudo-scalar masses as predicted by the various potentials. Kwong and Rosner [19] have surveyed the techniques for estimating the masses of the $c\bar{b}$ ground state; their results are listed as follows:

$$6.194\ \mathrm{GeV/c^2} < \mathrm{Mass}(B_c) < 6.292\ \mathrm{GeV/c^2} \tag{1-3}$$

and

$$6.284\ \mathrm{GeV/c^2} < \mathrm{Mass}(B_c^*) < 6.357\ \mathrm{GeV/c^2} \tag{1-4}$$

Eichten and Quigg in Ref. [17] take

$$\mathrm{Mass}(B_c) = 6.258 \pm 0.020\ \mathrm{GeV/c^2} \tag{1-5}$$

as the best estimate for the interval in which the B_c meson will be found.

The mass spectrum of the $c\bar{b}$ system with the various splittings is shown in Fig. 1-1. This spectrum was calculated by Eichten and Quigg [17] in the Buchmüller-Tye potential [6]. The spectrum is similar to those calculated by Eichten and Feinberg [21] in the Cornell potential, by Gershtein. et al. [22] in the Martin potential and by Chen and Kuang [23] in a QCD inspired potential developed by them.

2. The B_c mass from the QCD Sum Rules

The mass calculations for the vector and the pseudo-scalar $c\bar{b}$ in the framework of the QCD sum rules agrees with the calculations made from the potential models. The errors of the mass estimates from the QCD sum rules are larger than that from the potential model. This is so because the results obtained from the QCD sum rules depend on the choice of the values of the hadronic continuum threshold energy and the current masses of the constituent quarks.

C. Decays of the B_c

1. Lifetime of the B_c meson

The B_c decay can take place in three ways; (1) the $\bar{b}$-quark decay with the spectator c-quark, (2) the c-quark decay with the spectator $\bar{b}$-quark and (3) the annihilation channel. The diagrams for the three modes of the decay are shown

Table 1-1. Quarkonium ground-state masses (in GeV/c^2) in the Buchmüller-Tye, power law, logarithmic and coulomb plus linear potentials.

Observable	QCD, Ref. [6, 18]	Power Law Ref. [4]	Logarithmic, Ref. [5]	Cornell Ref. [19]
$(c\bar{c})$ 1S	3.067	3.067	3.067	3.067
ψ	3.097	3.097	3.097	3.097
η_c	2.980	2.980	2.980	2.980
$\psi - \eta_c$	0.117^a	0.117^b	0.117^c	0.117^d
$(c\bar{b})1S$	6.137	6.301	6.317	6.321
B_c^*	6.337	6.319	6.334	6.343
B_c	6.264	6.248	6.266	6.254
$B_c^* - B_c$	0.073	0.071	0.068	0.089
$(b\bar{b})1S$	9.440	9.446	9.444	9.441
Υ	9.464	9.462	9.460	9.476
η_b	9.377	9.398	9.395	9.335
$\Upsilon - \eta_b$	0.087	0.064	0.065	0.141

[a] Input value; determines $\alpha_s = 0.36$. [b] Input value; determines $\alpha_s = 0.43$

[c] Input value; determines $\alpha_s = 0.37$. [d] Input value; determines $\alpha_s = 0.31$

in Fig. 1-2. The total width of the decay [24] is summed from the three partial widths,

$$\Gamma(B_c \to X) = \Gamma(b \to X) + \Gamma(c \to X) + \Gamma(\text{ann}) \tag{1-6}$$

If we ignore the quark binding energy inside the B_c then we can arrive at a simplistic estimate of the width. The width due to the b-spectator and the c-spectator can be written as

$$\begin{aligned} \Gamma(b \to X) &= 9\frac{G_F^2|V_{bc}|^2 m_b^5}{192\pi^3}, \qquad (1\text{-}7)\\ \Gamma(c \to X) &= 5\frac{G_F^2|V_{bc}|^2 m_b^5}{192\pi^3} \qquad (1\text{-}8) \end{aligned}$$

respectively. The width of the annihilation channel can be expressed as :

$$\Gamma(\text{ann}) = \sum_i \frac{G_F^2}{8\pi}|V_{bc}|^2 M_{bc} m_i^2 \left(1 - \frac{m_i^2}{m_{B_c}^2}\right)^2 f_{B_C}^2 C_i, \tag{1-9}$$

where $C_i = 1$ for the $\tau\nu_\tau$ channel, $C_i = 3|V_{cs}|^2$ for the $\bar{c}s$ channel and m_i is the mass of the heaviest fermion.

The three widths can be calculated from the known parameters in Equations 1-7, 1-8 and 1-9. From these calculations one can get a rough estimate on the lifetime, which should be of the order of $\tau_{B_c} \approx (2-5) \times 10^{-13}$s. In this estimate, the fractions of the b-quark decay , c-quark decay and the annihilation decay are 45%, 50%, and 5%, respectively [24]. However, these estimates do not take into consideration the strong binding of the quarks in the B_c meson. After incorporating the corrections due to the strong binding of the quarks in the B_c, the three processes for the B_c meson decay result in an approximate estimate for the B_c life time [24], which is quoted as

$$\tau_{B_c} \approx 5 \times 10^{-13}\text{s} \tag{1-10}$$

With this correction, the fractions of the b-quark decay, c-quark decay and the annihilation decay channels are 45%, 37% and 18% respectively. Most of the uncertainty in the B_c life time comes from the choice of the quark masses. The probabilities of the various decays are shown in Table 1-2 (from Ref. [25]).

Table 1-2. The width (in eV) of the inclusive decays of the b and the c quarks in free and bound (B_c) states and the branching ratios (BR in %) of the inclusive B_c decays.

Decay Mode	Free quarks	B_c^+	B.R. in %	Decay Mode	Free quarks	B_c^+	B.R. in %
$b \to \bar{c} + e^+ + \nu_e$	62	62	4.7	$c \to s + e^+ + \nu_e$	124	74	5.6
$b \to \bar{c} + \mu^+ + \nu_\mu$	62	62	4.7	$c \to s + \mu^+ + \nu_\mu$	124	74	5.6
$b \to \bar{c} + \tau^+ + \nu_\tau$	14	14	1.0	$c \to s + u + d$	675	405	30.5
$b \to \bar{c} + \bar{d} + u$	248	248	18.7	$c \to s + u + \bar{s}$	33	20	1.5
$b \to \bar{c} + \bar{s} + c$	13	13	1.0	$c \to d + e^+ + \nu_e$	7	4	0.3
$b \to \bar{c} + \bar{s} + c$	87	87	6.5	$c \to d + \mu^+ + \nu_\mu$	7	4	0.3
$b \to \bar{c} + \bar{d} + c$	5	5	0.4	$c \to du + \bar{d}$	39	23	1.7
$B_c^+ \to \tau^+ + \nu_\tau$	-	63	4.6	$B_c^+ \to c + \bar{s}$	-	162	12.2
$B_c^+ \to c + \bar{d}$	-	8	0.6	$B_c^+ \to$ all	-	1328	100

2. Experimental Signatures

The branching ratio of the $B_c \to J/\psi + X$ is about 17 %. Hence it is a desirable decay channel for the experimental search for the B_c. It can be searched in the exclusive mode $B_c \to J/\psi + \pi$ or the inclusive channel $B_c \to J/\psi + \ell + X$. These two channels have a clean experimental signature. In the exclusive case, one searches for two muons from the J/ψ and a pion track from a displaced vertex. For the inclusive channel, one searches for the two muons from the J/ψ and a lepton (muon or electron) from a displaced vertex. Although the exclusive channel is required to reconstruct the B_c mass, the branching ratio for $B_c \to J/\psi + \pi$ is about 0.24% [25] which makes it more difficult to find. The inclusive channel is most probably the discovery channel. The branching ratio for the $B_c \to J/\psi + \ell + X$ decay channel is about 4.7% [25]. The search for the B_c meson in the $B_c \to J/\psi + \pi$ channel has been done at CDF and the 95% C.L.

upper limit on the relative production of the $B_c \to J/\psi + \pi$ to $B_u \to J/\psi K$ is reported in Ref. [26].

This thesis describes the search for the B_c meson in the inclusive channel $B_c \to J/\psi + \mu + X$.

D. Production of the B_c at the Tevatron

1. Production Cross Section

The calculation of the B_c production in e^-e^+ collisions shows that

$$\sigma(Z^0 \to B_c^{\pm} X) \sim \sigma(Z^0 \to b\bar{b}X) \times 10^{-3} \tag{1-11}$$

This estimate agrees with the Monte Carlo events from HERWIG [27] in which Z^0 decays into $B_c^{\pm}$. Using HERWIG, Lusignoli, et al., in Ref. [28] show that at the Tevatron the $B_c^{\pm}$ production would be about 10^{-3} times the $b\bar{b}$ production cross section.

Masetti, et al. in Ref. [29] showed that the hadronic production of the B_c at high energies is dominated by the subprocesses $gg \to B_c b\bar{c}$. The hadron production cross section can be calculated fully to order α_s^4 in the framework of perturbative QCD (PQCD). This calculation has been performed by several authors [30, 31, 32, 33]. In this estimate the gluon-gluon scattering at lowest order involves 36 diagrams. The 36 diagrams can be obtained from Fig. 1-3 by taking all the combinations of the initial gluon momenta and the final quark flavors. The process $q\bar{q} \to B_c b\bar{c}$ is expected to give a negligible contribution to the hadronic production cross section. The production cross section is estimated for different gluon distribution functions and evolution scale Q^2. Figure 1-4 (from Ref. [29]) shows the differential cross section $d\sigma/dp_T$ for direct B_c production. It is calculated for both the Tevatron and the LHC energies using the MRS(A) gluon distribution for two different evolution scales ($Q^2 = 4M_{B_c}^2$ and $Q^2 = \hat{s}$). Masetti, et al. in Ref. [29] give an estimate for the B_c production cross section in hadronic collisions, including the contribution due to the production of the excited B_c^* state which finally decays into the pseudo-scalar B_c. The total cross section will be,

$$\sigma_{total}(p\bar{p} \to B_c^+ X) \sim 20\ -\ 50\,\mathrm{nb}\ (\mathrm{At\,the\,Tevatron\,energy\,of\,1.8\,TeV}) \tag{1-12}$$

$$\sigma_{total}(p\bar{p} \to B_c^+ X) \sim 0.3\ -\ 0.8\,\mu\mathrm{b}\ (\mathrm{At\,the\,LHC\,energy\,of\,14\,TeV}) \tag{1-13}$$

2. Prospects of Finding the B_c at CDF

The number of $B_c \to J/\psi + \mu + X$ events expected to be observed at CDF can be determined using the estimate

$$\frac{\sigma(B_c^+ B_c^-)}{\sigma(b\bar{b})} \approx 10^{-3} \tag{1-14}$$

We can write the following equation:

$$\frac{(B_c \to J/\psi\mu X)}{(B \to J/\psi X)} \quad = \quad \frac{\sigma(B_c^+ B_c^-)}{\sigma(b\bar{b})} \times \frac{BR(B_c \to J/\psi\mu X)}{BR(B \to J/\psi X)} \approx 5 \times 10^{-3} \tag{1-15}$$

We observe about 40,000 J/ψ's in the CDF data that come from a B decay; of these, 200 J/ψ's would come from $B_c \to J/\psi\mu X$. From Monte Carlo we get the following formula:

$$\frac{\mathrm{Number\,of\,B_c\,events\,picked\,by\,analysis\,code}}{\mathrm{Number\,of\,B_c\,passing\,the\,J/\psi\,trigger}} = .026 \tag{1-16}$$

Using this number, we would expect to observe about 5 $B_c \to J/\psi\mu X$ events in the CDF data. However, this number will have an error in excess of 70% due to the uncertainties in Eq. 1-14 and the branching ratio of $B_c \to J/\psi + \mu + X$.

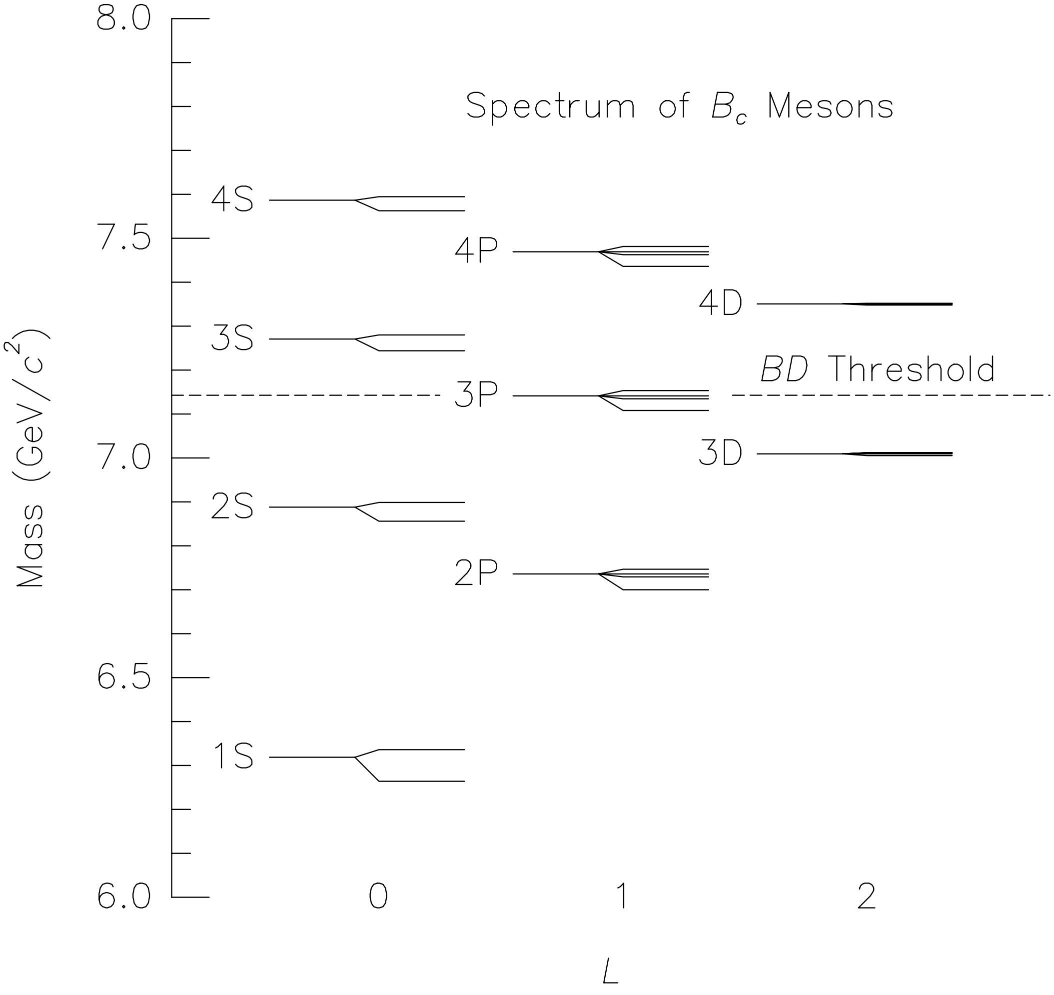

Figure 1-1. Mass spectrum of the $c\bar{b}$ system along with the splittings of the various levels [17].

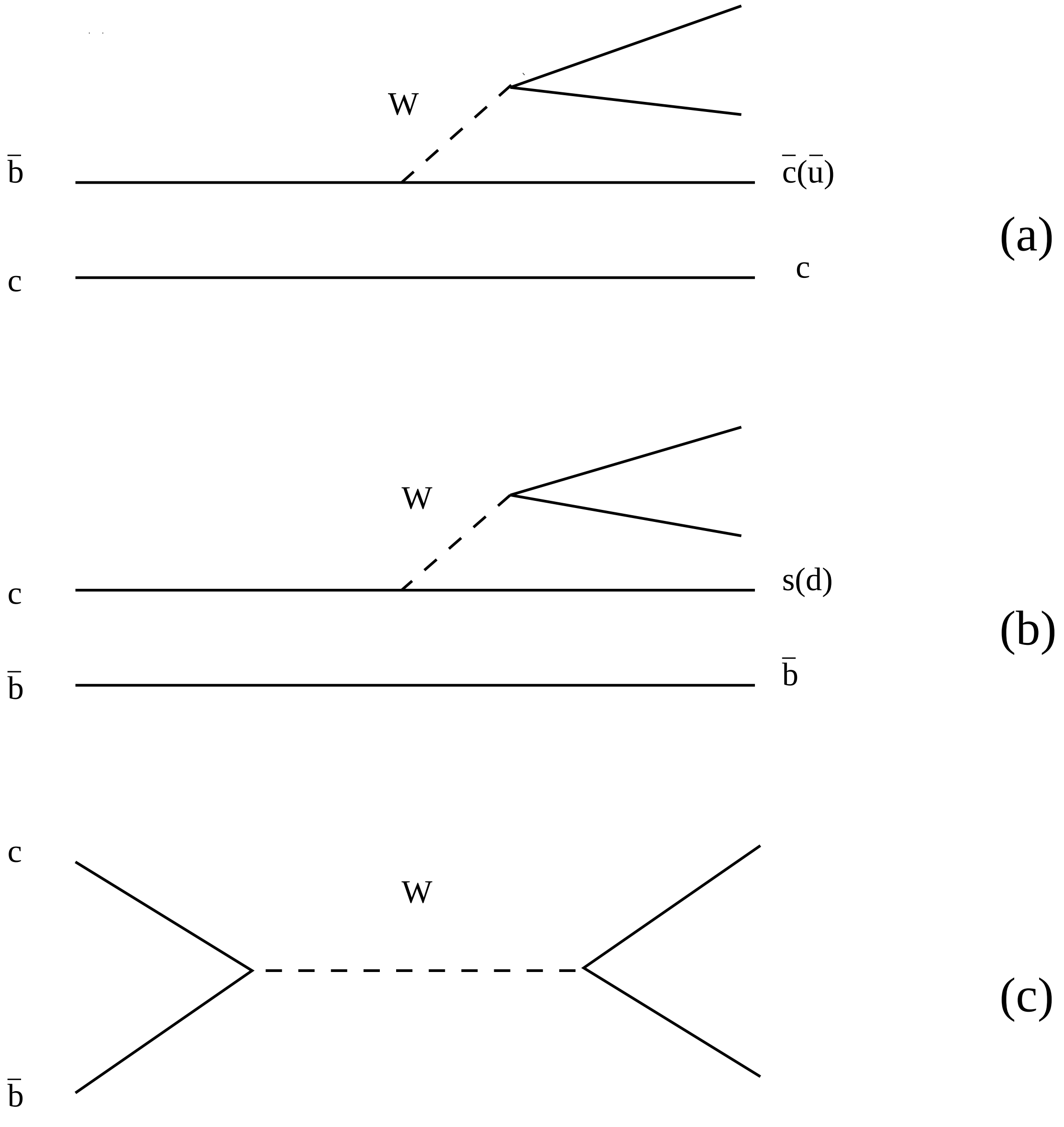

Figure 1-2. The diagrams of the B_c decays; (a) the c-spectator decays; (b) the $\bar{b}$-spectator decays; (c) the annihilation decays.

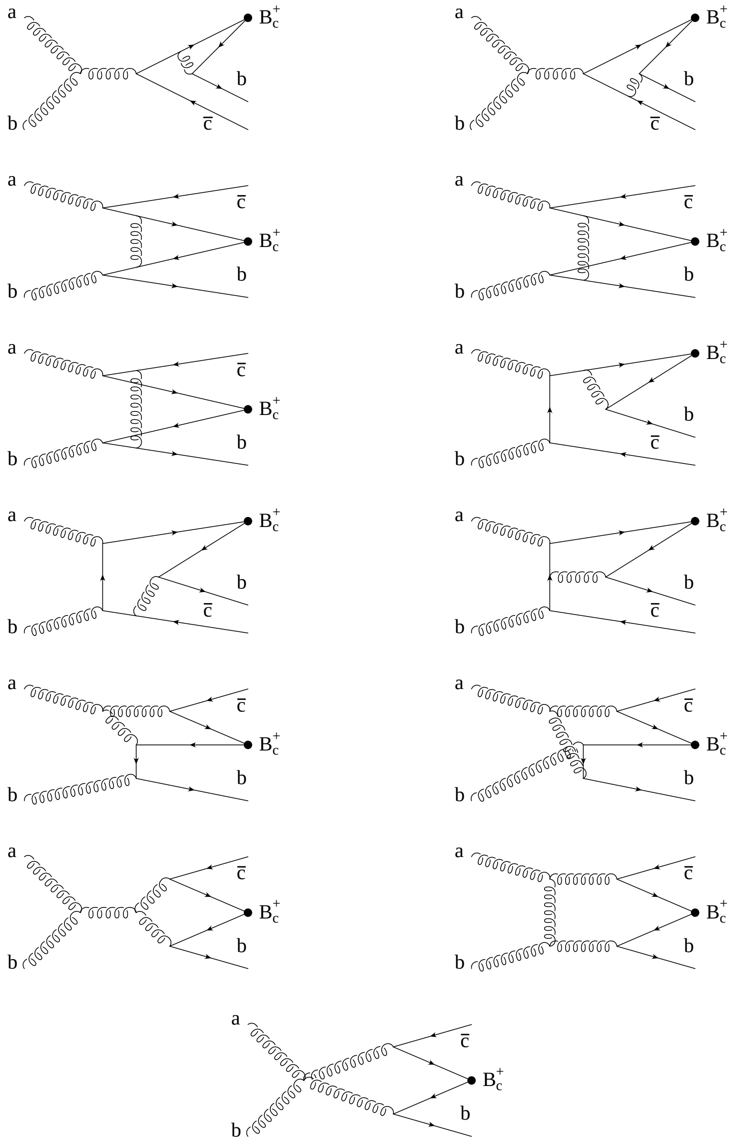

Figure 1-3. Feynman diagrams for $gg \to B_c^+ b\bar{c}$. There are 13 diagrams shown in this figure, the complete set of 36 diagrams can be obtained from the 13 diagrams by performing all the possible combinations of the initial gluon momenta and the final quark flavors.

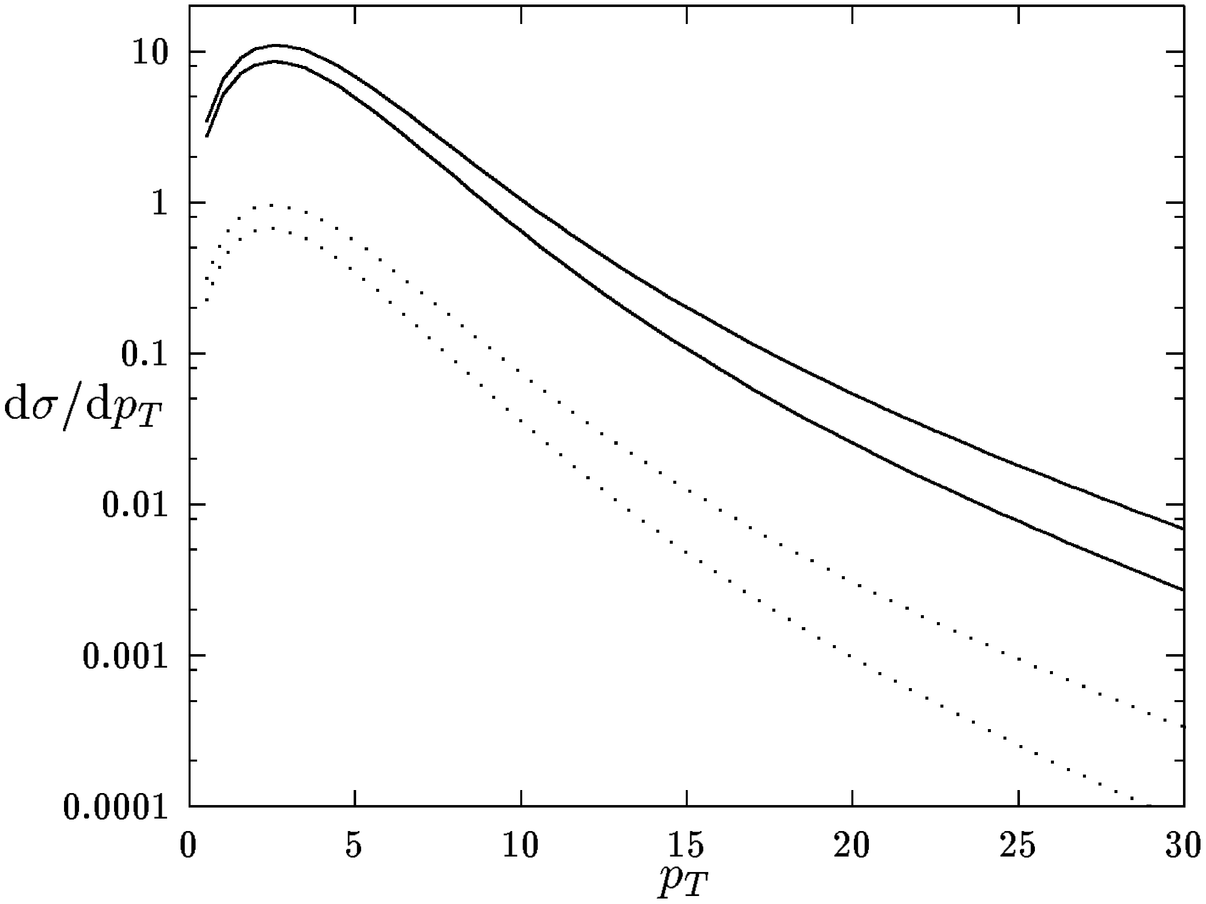

Figure 1-4. Differential cross section $d\sigma/dp_T$ (in nb GeV^{-1}) for direct B_c production calculated with MRS(A) gluon distribution for Tevatron ($\sqrt{s} = 1.8$TeV). The upper dotted line shows the distribution with the evolution scale $Q^2 = 4M_{B_c}^2$ and the lower dotted line shows the distribution with the evolution scale $Q^2 = \hat{s}$. The two solid lines show similar distributions for the LHC ($\sqrt{s} = 14$TeV).

CHAPTER 2.

The Tevatron and the CDF Detector

The experiment described in this thesis was performed using the CDF detector at the Fermilab Tevatron. The Tevatron is a $p\bar{p}$ accelerator and a storage ring facility. The CDF detector is used to study $p\bar{p}$ collisions at the Tevatron. A brief description of the Tevatron and the CDF detector is presented in this chapter. A more thorough description of the detector is given in [36, 37, 38, 39].

A. Tevatron

The Tevatron is currently the highest energy particle accelerator in the world. It can be operated in both "fixed target" and "collider" modes. When operated in the collider mode, the center of mass energy of the the colliding beam is 1.8 TeV. Figure 2-1 shows a schematic diagram of the Tevatron along with the linac, booster, main ring and the anti-proton storage ring.

1. Introduction

Physics processes like high Q^2 QCD scattering, b quark production, top quark production, W production and SUSY production depend critically on the accelerator energy. To obtain high mass or high Q^2, one needs energetic initial state partons. Since the parton distribution in the proton is peaked at small x $(= P_{parton}/P_{proton})$, a high flux of energetic partons requires protons with high energies.

A large number of $p\bar{p}$ collisions must take place to observe processes with small production cross sections. Luminosity is a parameter that gives the rate

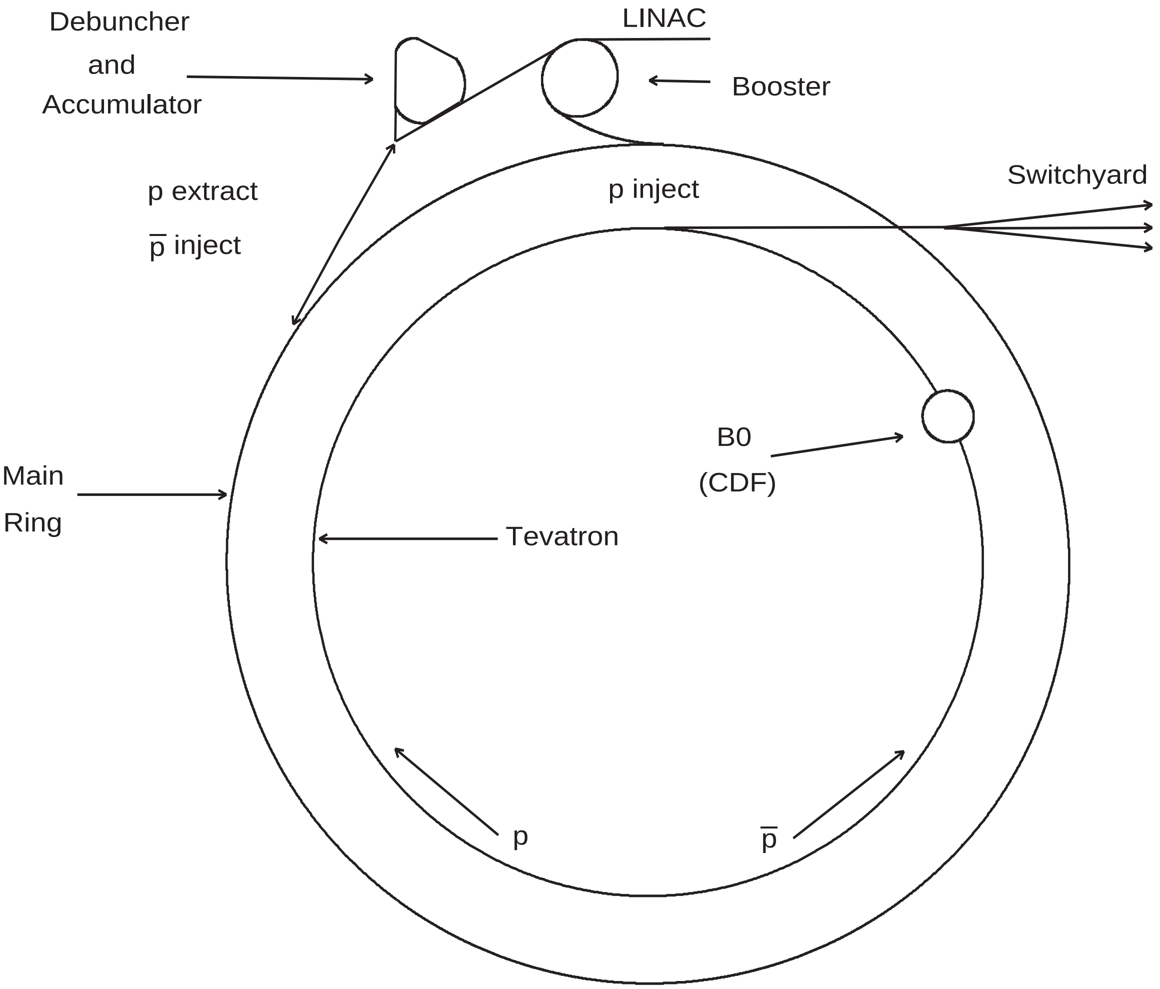

Figure 2-1. Schematic drawing of the beam-lines at Fermilab. The figure shows the Linac, Booster, Main Ring, Tevatron and the Anti-proton storage ring

of collisions. It is given by

$$N = \sigma L, \tag{2-1}$$

where N is the number of events produced per second for a final state, σ is the production cross section for that state and L is the luminosity. The unit of luminosity is the inverse of the unit of cross section. For an accelerator like the Tevatron, which has particles distributed in bunches rather than a continuous beam , the luminosity is defined as

$$L = \frac{N_p N_{\bar{p}} B f_0}{4\pi\sigma^2} \tag{2-2}$$

where N_p and $N_{\bar{p}}$ are the numbers of protons and anti-protons in each bunch. B is number of the bunches of each type, f_0 is frequency of revolution (50 kHz for the Tevatron), and σ is the transverse cross-sectional size of the bunches. The transverse beam size, σ, is determined by the magnetic focusing properties of the accelerator and the characteristics of the beam. It can be expressed as

$$\sigma^2 = \frac{\beta^*}{\pi\gamma}\left(\frac{\epsilon_N^p + \epsilon_N^{\bar{p}}}{2}\right)^2, \tag{2-3}$$

where β^* depends on the configuration of the accelerator's quadrupole magnets and ϵ_N is the invariant beam emittance. Beam emittance ($\epsilon \equiv \int dx'dx$, where $x' = dx/dz$) is the phase space area occupied by the beam; the invariant beam emittance is given by $\epsilon_N = \gamma\epsilon$. In order to maximize the luminosity, β^* and the beam emittance should be minimized and the beam energy (γ) maximized.

2. Operation of the Tevatron

To get proton beams in the collider, one starts with negatively charged hydrogen, which is accelerated in a Cockroft-Walton accelerator to 750 keV. The two electrons are then stripped from the ion and the resulting proton is transferred to the linac (linear accelerator) in bunches. In the Linac the proton bunches are accelerated to 200 MeV. The bunches are then injected into a Booster Ring, which accelerates them to 8 GeV and injects them into the main ring. The main ring accelerates them to 150 GeV and puts them in the Tevatron which accelerates them further to 900 GeV, which is the final energy of the beam. This process is shown in the flow chart in Fig. 2-2. A total of six proton bunches are injected into the Tevatron and collide with six bunches of anti-proton of the same energy coming from the opposite direction. There are six interaction regions for the proton anti-proton collisions. The CDF experiment is located at the interaction region called B0.

The main ring is also used for the production of anti-protons. To produce anti-protons, protons are accelerated in the main ring to 120 GeV and collide with a tungsten target. Anti-protons are created in the ensuing collision. The anti-protons created by the tungsten target are passed through a lithium lens and into a debuncher ring. This cools the beam stochastically and uses bunch rotation techniques to reduce the energy spread and the transverse motion of the anti-protons. The anti-protons are then sent into an accumulator. The accumulator stores the anti-protons until there are enough of them to start the colliding beams in the Tevatron. For the Run 1a and the Run 1b of the Tevatron a stack of about 10^{12} anti-protons was considered to be sizable enough to have an effective collider run.

Once the six bunches of the protons are injected into the Tevatron the accumulator injects six bunches of anti-protons in the main ring. The main ring accelerates them from 8 GeV to 150 GeV and injects them into the Tevatron, which further accelerates them to 900 GeV. The accelerator parameters for Run 1a and Run 1b are listed in Table 2-1.

Table 2-1. The Tevatron parameters during Run 1a and Run 1b

Energy	900 GeV/c^2
Number of Proton Bunches	6
Number of Anti-Proton Bunches	6
Emittance for Protons	$\equiv 25\pi$ mm-mrad
Emittance for Anti-Protons	$\equiv 15\pi$ mm-mrad
β^*	$\equiv 0.5$ m
Luminosity	$\equiv 10 \times 10^{31}$ cm^{-2}s^{-1}

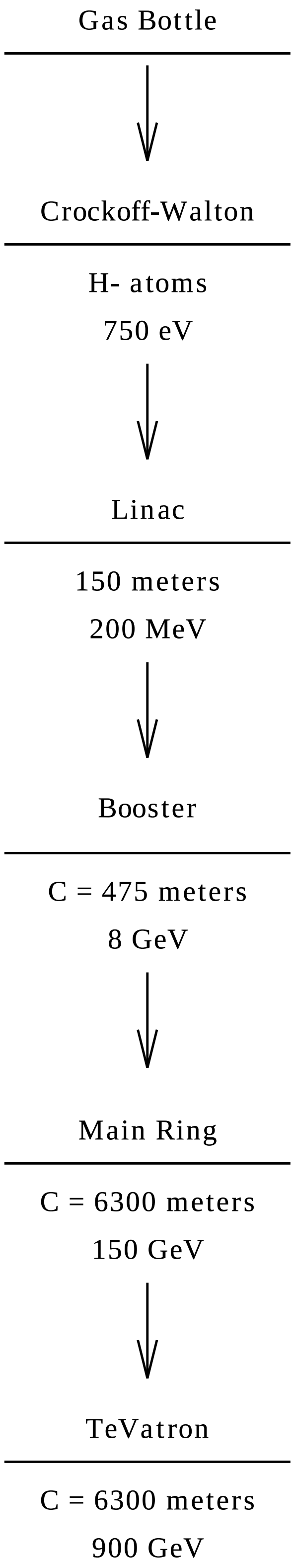

Figure 2-2. Flowchart of the process by which protons are accelerated to 900 GeV/c^2 at the Fermilab Tevatron.

B. The CDF Detector

The CDF detector is a multipurpose detector operating at the B0 interaction region of the Fermilab Tevatron. Figure 2-3 shows a side view cross section of the CDF detector. The protons travel from the east and the anti-protons travel from the west. The direction of the proton beam is assumed to be the z coordinate of the detector and the center of the detector is at the nominal $p\bar{p}$ interaction point at B0.

The CDF detector is azimuthally symmetric and has backward-forward symmetry about the $p\bar{p}$ interaction point. The detector has a central tracking system. The tracking system is contained in a super-conducting solenoid of length 4.8 m and radius 1.5 m. The magnetic field of the solenoid is 1.4 T. The tracking chambers are used to detect charged particles and to measure their momenta. The central tracker consists of a Silicon Vertex Detector (SVX$'$), which is the closest to beamline. The SVX$'$ is surrounded by a Vertex Tracking Chamber (VTX) and the VTX is surrounded by a Central Tracking Chamber (CTC). The central tracking system covers the the central region in the pseudo-rapidity range ± 1.6 . Beyond the CTC lies the super-conducting solenoidal magnet. The magnet is surrounded by sampling calorimeters which measure the electromagnetic and hadronic energies of electrons and jets. Drift chambers beyond the calorimeters detect muons. There are also calorimeters in the plug and forward regions. PEM and PHA in Fig. 2-3 show the Plug Electro-magnetic and the Plug Hadronic calorimeters; FEM, FHA, FMU depict the Forward Electro-magnetic, Forward Hadron and the Forward Muon calorimeters in the same figure. Each detector sub-part, except for the SVX$'$, are described in the following sections. SVX$'$ is described in detail in the following chapter. This additional emphasis on the SVX$'$ reflects the author's contributions to the development, construction and installation of the SVX$'$ detector. SVX$'$ also plays an important role in the search for the B_c analysis.

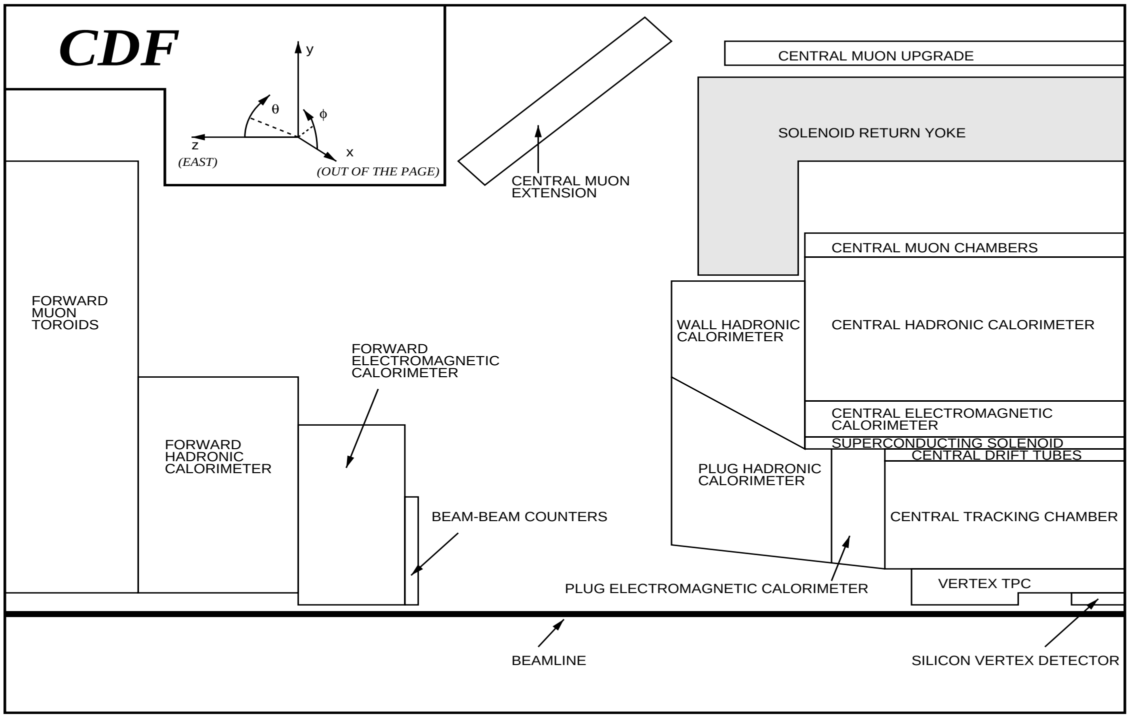

Figure 2-3. A side view cross-section of the CDF detector. The detector has forward and backward symmetry around the interaction region. It also has azimuthal symmetry.

1. VTX - Vertex Tracking Chamber

The VTX is a proportional wire chamber. It consists of eight octagonal modules which are arranged to form a barrel surrounding the SVX$'$. Each wedge of the octagonal module has wires parallel to the base of the wedge. This arrangement enables one to make an accurate measurement of the the primary vertex in z. The chamber is filled with a gaseous mixture of 50% argon and 50% ethane bubbled through alcohol at -7^oC. A charged track makes an ionization trail in the gas mixture. The electron component of the ionization trail is attracted to the wires. The resulting avalanche causes a drop in the wire voltage.

The VTX can measure the z position of the primary vertex to an accuracy of ±2 mm.

2. CTC - Central Tracking Chamber

The CTC is the principal tracking device of the CDF detector. It surrounds the VTX and is itself inside a 1.4 T solenoidal magnet. The barrel of the drift chamber has a diameter of 2.76 m and a length of 3.2 m. There are 36504 sense and field shaping wires extending along the length of the CTC. The chamber is filled with an argon-ethane gas mixture. The wires are arranged into 84 layers which are divided into 9 super-layers, five axial and four stereo (3^o tilt) layers. The axial super-layers have twelve layers of wires and are alternated with the stereo super-layers, each of which has six layers of wire. The wires within a super-layer are grouped in measurement cells so that the maximum drift distance is less than 40 mm, corresponding to 800 ns of drift time. Figure 2-4 shows the diagram of the CTC end-plate showing the arrangement of the blocks which hold the 84 sense wires.The detector resolution is

$$\frac{\delta p_t}{p_t} = 0.0011 \times p_t \tag{2-4}$$

$$\delta(r\phi) = 0.2mm \tag{2-5}$$

$$\delta z = 4mm \tag{2-6}$$

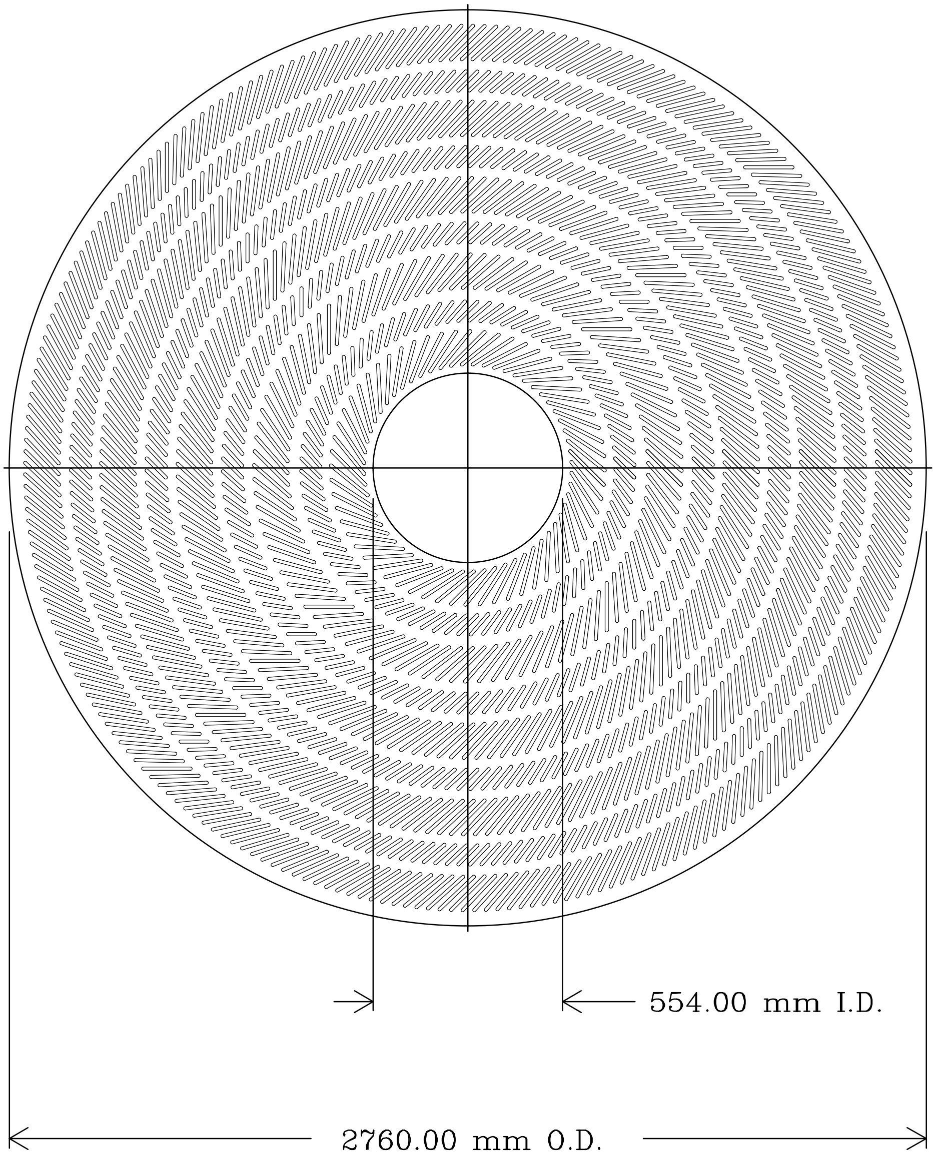

Figure 2-4. The CTC end-plate showing the arrangement of the blocks which hold the 84 sense wires.

3. Calorimetry

The tracking system of the CDF detector is surrounded by various sampling calorimeters. The calorimeters can be divided into central, plug and forward calorimetry. They are segmented in azimuthal and pseudo-rapidity increments to form a projective tower geometry, which points back to the interaction point.

Each region has an electro-magnetic calorimeter and behind it a hadronic calorimeter. The central electro-magnetic calorimeter is called CEM, the plug calorimeter is called PEM and the forward calorimeter is called FEM. The hadronic calorimeter overlapping the CEM is divided into two parts, the central (CHA) and the wall (WHA). The PEM is overlapped by the PHA and the FEM is overlapped by the FHA. The absorber in the hadron calorimeter is iron and in the electro-magnetic calorimeters it is lead. Figure 2-3 show the locations of the various calorimeters. Table 2-2 shows the coverage, thickness and resolution of these calorimeters and Fig. 2-5 shows the coverage in η and ϕ schematically.

The central calorimeter towers are 15^o wide in ϕ and 0.1 units wide in η. They use scintillating polystyrene as active material. In the presence of ionizing radiation this material emits blue light which is collected in an acrylic-doped wave length shifter and is directed to a photo-multiplier tube through clear acrylic light guides. There are the central proportional chambers with strip and wire readout (called the central electro-magnetic strip detector (CES)) at six radiation lengths into the CEM calorimeter. CES provides shower position measurements in both the z and the $r-\phi$ views. The proportional chamber located between the solenoid and the CEM constitutes the central pre-radiator (CPR) detector. CPR samples the early development of the electro-magnetic shower in the material of the solenoidal coil. It provides only the $r-\phi$ information. In the plug and the forward region the active medium is proportional chambers using an argon-ethane gas mixture. Each PEM detector is a torus, 2.8 m in diameter and 50 cm deep. Each PEM consists of 34 layers of conductive plastic proportional tube arrays interleaved with 2.7 mm lead absorber. The cathode readout consists of pads and strips etched out on printed circuit boards which results in a finely segmented projective geometry. The PHA lies just outside the

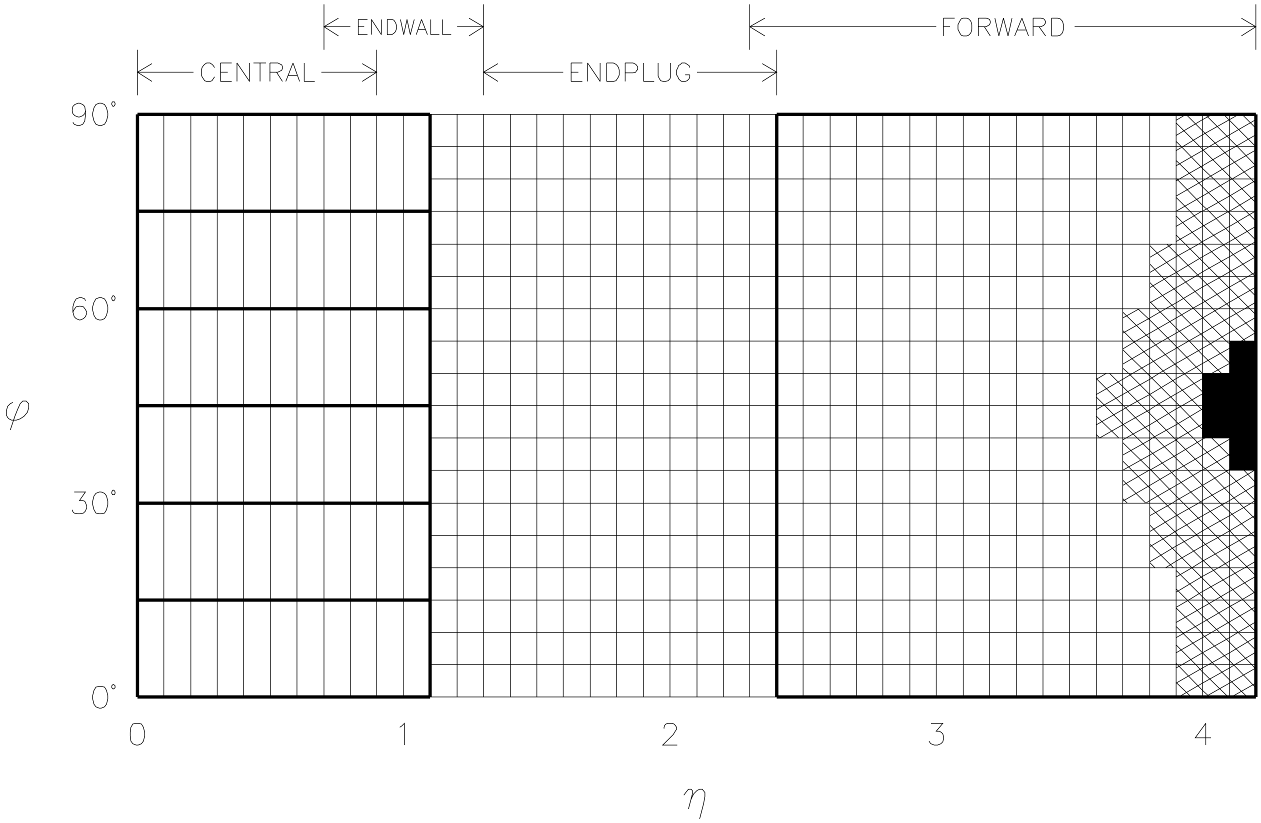

Figure 2-5. The η and ϕ coverage of the various calorimeters at CDF.

Table 2-2. Summary of the CDF calorimeter properties. The symbol $\bigoplus$ implies that the constant term is added in quadrature in the resolution. The energy resolutions for the electro-magnetic calorimeters are for incident electron and photons and for the hadron calorimeters are for incident isolated pions. The unit of energy is GeV. The thickness for the electro-magnetic calorimeters is given in radiation lengths (X_0) and for the hadronic calorimeters it is given in interaction lengths (λ_0)

Calorimeter	Coverage in η	Energy Resolution	Thickness
CEM	$\|\eta\| < 1.1$	$13.7\%/\sqrt{E_t}\bigoplus 2\%$	$18X_0$
PEM	$1.1 < \|\eta\| < 2.4$	$22\%/\sqrt{E_t}\bigoplus 2\%$	18-21X_0
FEM	$2.2\|\eta\| < 4.2$	$26\%/\sqrt{E_t}\bigoplus 2\%$	$25X_0$
CHA	$\|\eta\| < 0.9$	$50\%/\sqrt{E_t}\bigoplus 2\%$	$4.5\lambda_0$
WHA	$0.7 < \|\eta\| < 1.3$	$75\%/\sqrt{E_t}\bigoplus 2\%$	$4.5\lambda_0$
PHA	$1.3 < \|\eta\| < 2.4$	$106\%/\sqrt{E_t}\bigoplus 2\%$	$5.7\lambda_0$
FHA	$2.4 < \|\eta\| < 4.2$	$137\%/\sqrt{E_t}\bigoplus 2\%$	$7.7\lambda_0$

PEM. It is shaped like a cone and is made up of 20 layers of proportional tubes alternated with 5.1 cm thickness iron plates. The FEM detector is composed of 30 layers of proportional tubes alternated with 0.48 cm lead-antimony alloy plates. The FHA has 27 layers of proportional tubes alternated with 5.1 cm iron plates.

4. CMU - Central Muon Chambers.

The central calorimeters act as hadron absorber for the central muon (CMU) detection systems. CMU consists of four layers of drift chambers located outside the central hadronic calorimeters. Each drift chamber measures 6 cm by 2.7 cm by 2.2 mm and has one stainless steel resistive 50 μm sense wire in its center (see Fig. 2-6). The CMU covers $|\eta| < 0.6$ and can be reached by muons with a P_t in excess of 1.4 GeV/c. In the 1992 CDF upgrade, 0.6 m of steel was added behind the CMU for additional hadron absorption and four more layers of drift chambers were added behind the additional steel for muon detection. This system is called the CMP (Central Muon uPgrade.). CMU covers about 84% of the solid angle for $|\eta| < 0.6$. The CMP covers 63% of the solid angle and the overlap of the two covers 53% of the solid angle. The coverage in the central region is extended to the pseudo-rapidity $0.6 < |\eta| < 1.0$ through the addition of four free standing conical arches which hold the drift chambers for muon detection. The drift chambers are sandwiched between scintillator counters which are used for triggering. This extension is called CMX and it covers about 71% of the solid angle for $0.6 < |\eta| < 1.0$. Figure 2-7 shows the η and ϕ coverage schematically.

In addition to the central muon chambers, there are the forward muon chambers (FMU). Three sets of drift chambers make up the FMU. There are large toroids in front of the FMU. The toroids are cast steel and produce a 1.4 T magnetic field at 2.0 m which helps determine the momenta of the charged muon tracks. The FMU has a diameter of 7.6 m which matches the diameter of the toroids. It is segmented in r and ϕ so that the three-dimensional momenta of the muons can be measured.

5. BBC - Beam-Beam Counter.

The Beam-Beam counter (BBC) is situated just in front of the forward calorimeter at 5.8 m from the interaction point and range from 0.32 to 4.47 degrees in θ. The BBC's are small scintillating detectors. They play a crucial role in the experiment. These are used for the level 0 triggering and the luminosity measurements. If tracks don not leave a signal in the both the BBC's within a 15 ns window, the detector is not read out. The luminosity is measured by counting the number of collisions when the BBC's allows the detector readout.

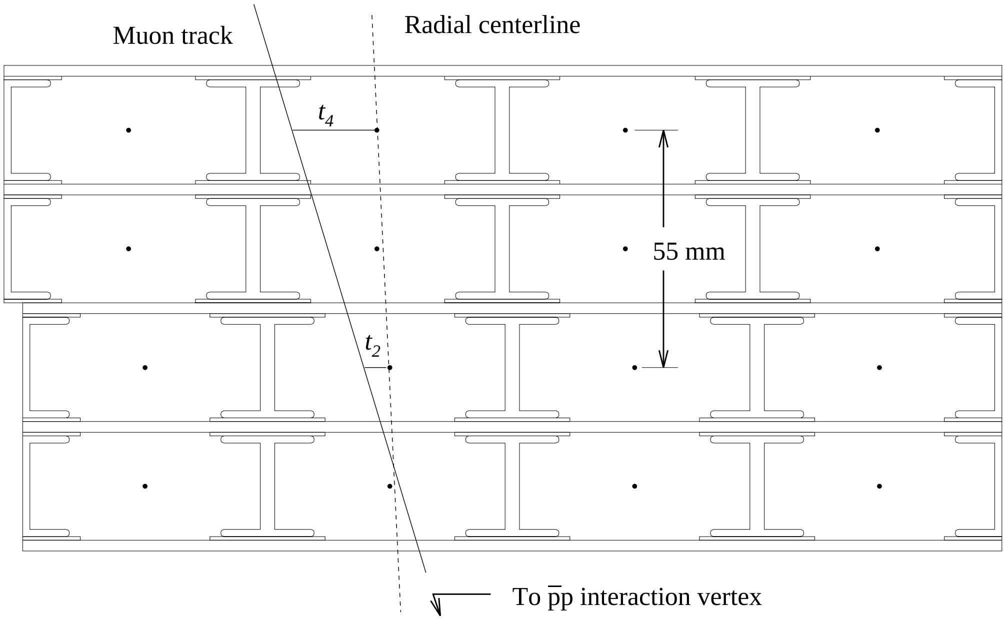

Figure 2-6. The Cross-sectional view of the muon chambers

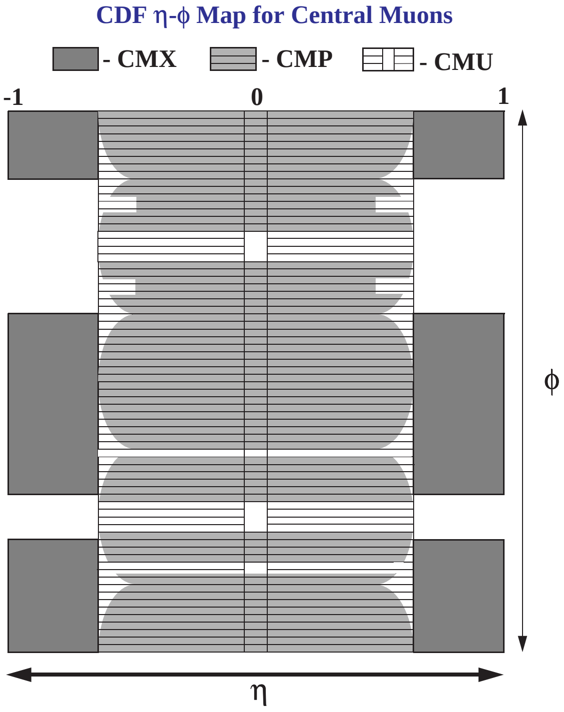

Figure 2-7. The η and ϕ coverage of the various muon chambers at CDF.

CHAPTER 3.

SVX$'$ Detector

A. Introduction

The innermost device of the tracking system of the CDF detector is a silicon vertex detector. The silicon detector was first installed during the 1990 upgrade of CDF. This detector was known as SVX and was used during Run 1a of the Tevatron. For Run 1b the original silicon vertex detector (SVX) was replaced by an upgraded detector called SVX$'$. SVX was the first such detector to be built for a hadron collider. During Run 1a SVX received about 15 kRad of radiation and would not have lasted for the duration of Run 1b; hence, it was replaced by SVX$'$ to ensure good operation throughout Run 1b.

The overall geometric design of SVX$'$ is the same as that of SVX. Compared to the DC coupled silicon strip detectors and radiation-soft read-out chips used in SVX, SVX$'$ had AC-coupled, FOXFET [40] biased silicon strip detectors and radiation hard read out chips. These differences made SVX$'$ a significant improvement over SVX. In this chapter we will mainly be discussing the SVX$'$ detector in detail.

B. Detector Description

1. Geometry

SVX$'$ consists of two independent cylindrical modules of equal length (see Fig. 3-1) These modules are aligned along the beam line (z-axis of the CDF) and are placed on both sides of the center of the CDF detector (z=0) with a gap of about 2.15 cm at z=0. The active length of SVX$'$ is 51 cm which results in an acceptance of $\sim$ 60% of the $p\overline{p}$ collision vertices.

Each module (also referred to as barrel) consists of four concentric layers, numbered from 0 to 3 in increasing radius (see Fig. 3-1). The inner and the outer radii of the barrel are 2.8612 and 7.8658 cm, respectively. The inner radius of SVX$'$ is less than that of SVX by $\sim$ .14 cm and the ladders in layer 0 of SVX$'$ have an additional 1^o rotation along their longitudinal axis. This was done to improve the ϕ coverage of layer 0. There is a 0.17^o (0.24 strip) overlap between the adjacent layer 0 ladders in SVX$'$ compared to a 1.26 degree gap in SVX. The basic building block of the layers is a ladder and is shown in Fig. 3-2. A ladder has three AC coupled, single sided silicon strip sensors. The sensors are made from 300 μm thick silicon wafers.The three sensors are micro-bonded to one another. AC coupling is provided by a 200 nm thick layer of SiO_2 over each strip's p^+ implant. The strip biasing is achieved through FOXFET, where each strip's implant acts as a source and there is a common gate and drain for all the strips on a ladder. Though there was a provision to apply a gate voltage, the gate was grounded during normal operation.

2. Readout Electronics

The readout chip of SVX$'$ (SVXH3-rev3 chip) was fabricated in 1.2 μm radiation hard CMOS technology. It was designed to tolerate more than 1 MRad of radiation. This chip has 20% less noise and 30% more gain than the chip used for SVX (SVXD chip). The typical charge gain for this chip is 21mV/fC.

C. Detector Performance

Each SVX$'$ barrel is divided into 12 wedges of 30^o in ϕ; the wedges are read out independently. To reduce the size of the raw data, only signals above a certain threshold are read out from the detectors. Two such thresholds can be set per wedge. The DC coupling of the SVX to its readout required that the device be operated in a quadruple sample and hold mode. In this mode the charge is

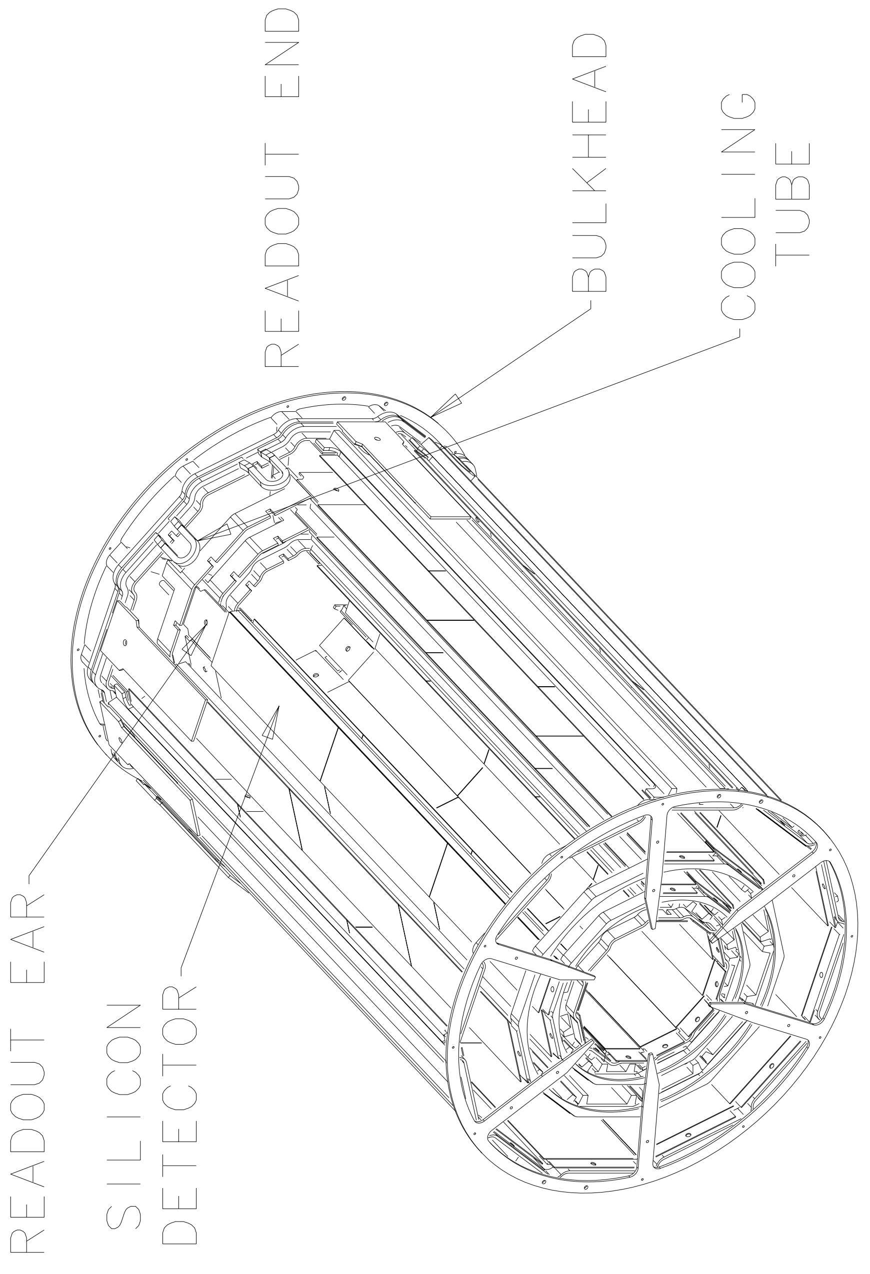

Figure 3-1. Schematic drawing of one of the SVX$'$ barrels

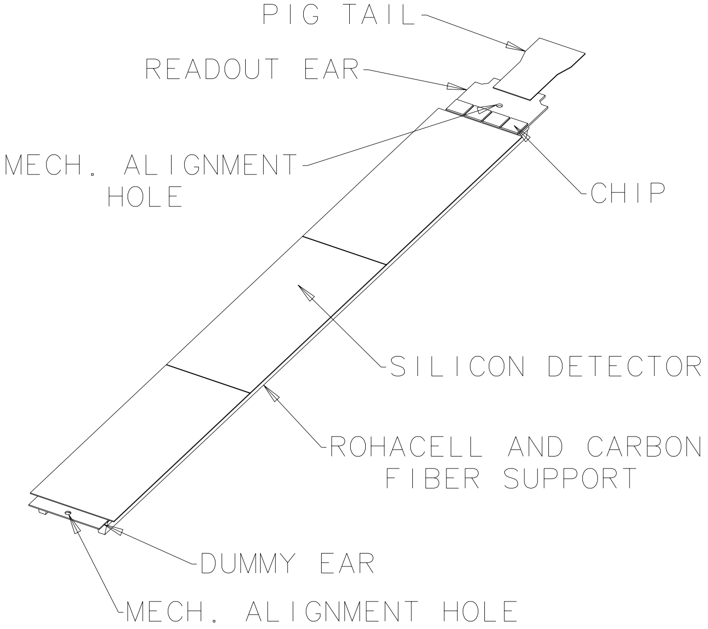

Figure 3-2. Schematic drawing of a SVX′ ladder.

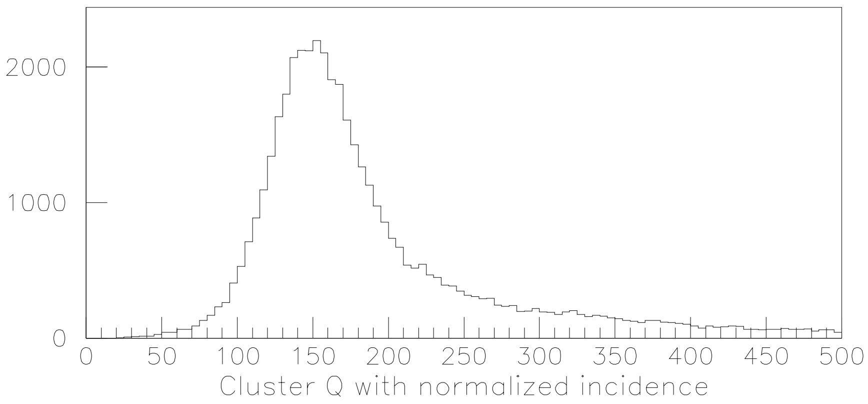

Figure 3-3. The charge deposited in ADC counts by a minimum ionizing particle in a SVX$'$ layer.

integrated twice (once “on beam” and once “off beam”); the difference of these integrations gives the signal. This is done to get rid of the baseline shift due to the varying strip - to - strip leakage current which would also be integrated during the sampling time. However, since SVX$'$ is AC coupled, the leakage current will not be seen by the readout electronics. Hence, SVX$'$ operates in a double sample and hold mode, where only one integration is done (“on beam”). This results in the reduction of SVX$'$ noise by $1/\sqrt{2}$ compared to that of SVX. The typical noise for SVX$'$ is 1300 electrons (10.8 ADC counts) compared to 2200 electrons for SVX. Figure 3-3 shows the plot of charge deposited in a layer of SVX$'$ by a minimum ionizing particle passing through it. The curve peaks around 160 ADC counts; using the value of noise as 10 ADC counts, we get the signal to noise (S/N) for SVX$'$ as 15, compared to 9.5 for SVX. The characteristics of each channel of SVX$'$ were monitored by taking calibration runs between the Tevatron stores when there was no beam activity. Calibration studies included measuring the pedestal, gain and the threshold of each channel of the device. Of the total 46080 channels of SVX$'$, about 1.7% had a shorted coupling capacitor. These channels were not bonded to the readout chip, instead they were grounded through a capacitor on the dummy (non readout) end.

1. Radiation Damage

SVX$'$ received about 90 kRad of radiation. The readout chips were designed to withstand 1MRad of radiation. Hence, for the amount of radiation that SVX$'$ received, no significant degradation in the operation of the readout chips was expected. Radiation causes an increase in the leakage current of the detector. This increase does not saturate the front end of SVX$'$ because of the AC coupling but it shows up as shot noise. For SVX$'$ the leakage current was seen to increase linearly with radiation dose. The rate of increase was about 1.05nA/kRad/strip on layer 0. This corresponded to a damage constant of $\alpha = 0.8 \times 10^{-8}$nA/cm, which is lower than that measured for the irradiated test detectors. The lower value for SVX$'$ may have been due the long time period during which the dose was accumulated and the subsequent annealing of the detectors. An increase in the leakage current of the detector does not not directly degrade the performance of the readout chip if the readout electronics is AC-coupled to the detector. However, the shot noise due to the increased leakage current does show up and decreases the signal to noise ratio. In the case of the SVX$'$, the observed increase in the noise through the period of Run 1b was not consistent with the observed increase in the leakage current. Figure 3-4 shows the observed "excess noise" of a typical SVX$'$ ladder and test ladders as a function of leakage current. The excess noise is defined as the total noise with the preradiation noise value subtracted in quadrature. The triangle symbols in the figure show the observed excess noise for a typical ladder. The solid circles show the excess noise for a SVX$'$ test ladder irradiated non-uniformly at Berkeley (LBL). The cross shows the excess noise for another SVX$'$ test ladder irradiated at TRIUMF. The star symbol shows the excess noise for a SVXII test ladder. SVXII is the new silicon vertex detector, which will be replacing SVX$'$ during Run II of the Tevatron. The dotted curve shows the expected contribution from shot noise. The open circles show the noise for an unirradiated SVX$'$ test ladder. The leakage current for this ladder was increased by artificially shining light on it. The increase in the noise for the SVX$'$ or SVX$'$ test ladders is about 4 times the expected shot noise. The increase in the noise of the SVXII test ladder is consistent with shot noise expectations. The SVXII ladders are biased through polysilicon compared to the FOXFET biasing of the SVX′ detector. This fact along with the observed noise from the two detectors point to the fact that the anomalous increase in the noise is due to a damage to the FOXFET structure. The anomalous increase in the noise cannot be attributed to a degradation in the readout chips because no anomalous increase in the noise or gain was seen for the channels in SVX′ which were not connected to a strip.

During the middle of Run 1b, efforts were made to decrease the noise of the detector to avoid degradation in the detector performance. This was done by studying the effect of bias voltage, integration time and temperature on the noise. The details of the study are documented in references [41, 42]. To reduce the noise the bias voltage was lowered by 3 volts, the integration time was reduced from 1280 ns to 960 ns and the temperature was reduced by 3^{o}C. These changes resulted in a decrease in the noise by 15% without affecting the signal. This change is shown in Fig. 3-5. The changes in the operating conditions were implemented at the accumulated dose of about 45 kRads. These changes resulted in the noise rising at a smaller rate than before the changes. At the beginning of the run the signal to noise was 15 and by the end of the run it came down to about 8 for layer 0.

D. Offline Performance

The first step in the offline reconstruction of tracks in SVX′ is the conversion of the charge on individual strips to clusters followed by matching of these clusters to tracks found by the Central Tracking Chamber(CTC). The conversion from the charge levels on an individual strip starts with the offline subtraction of the pedestals. The pedestal subtraction is carried out on a strip by strip basis and the pedestal values are taken from a pedestal calibration run. After the pedestal subtraction, the strips are clustered using a clustering algorithm that requires that there be a group of contiguous strips which have a charge greater than ‘M’ times the noise, where ‘M’ is 4, 2.5, and 2 for 1 strip, 2 strip and ≥ 3 strip clusters, respectively. The values of ‘M’ were optimized for good hit efficiency and noise rejection using cosmic ray and collision data. Cluster

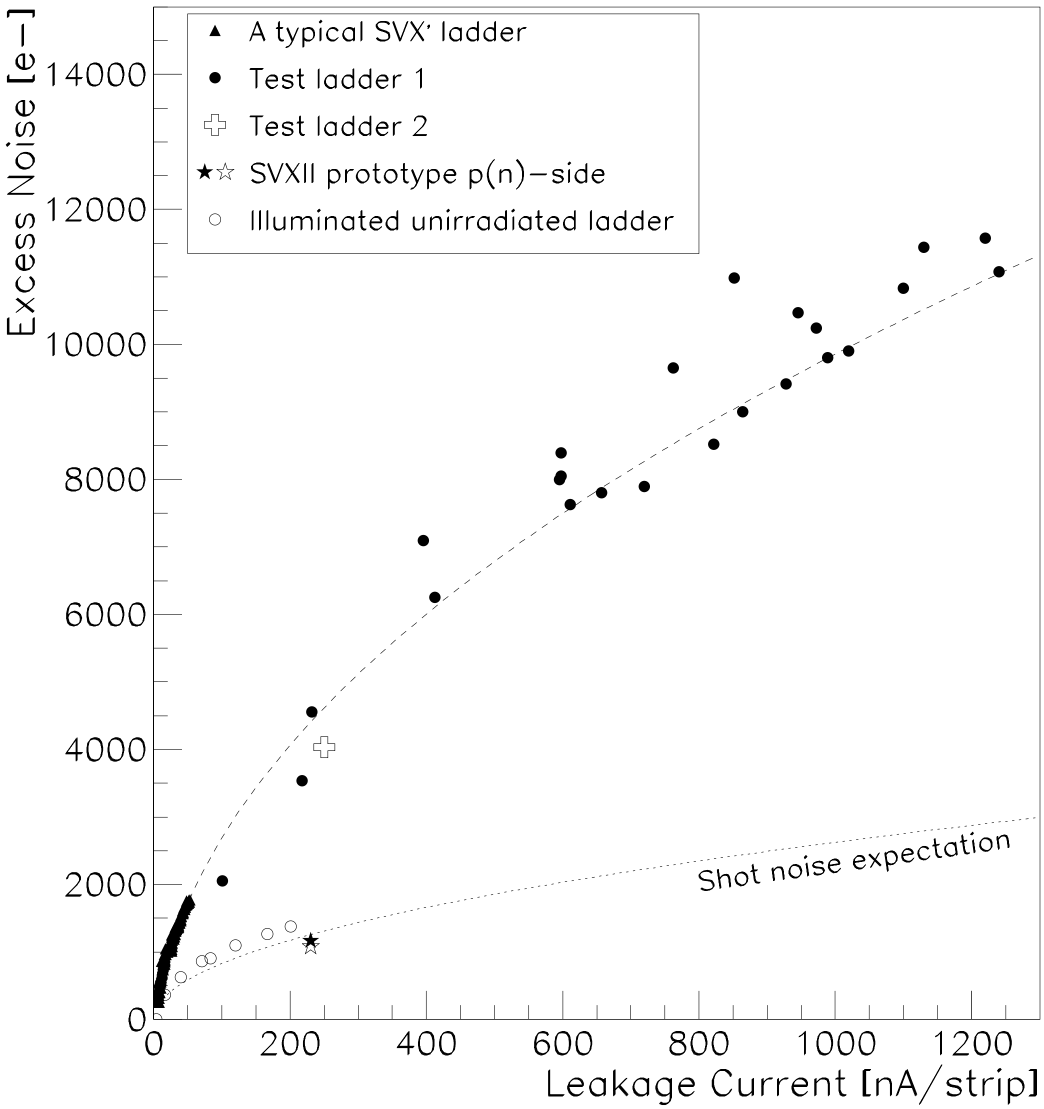

Figure 3-4. The excess noise seen as a function of the leakage current for SVX′ ladders, SVX′ test ladders and SVXII test ladders.The triangle symbols in the figure show the observed excess noise for a typical ladder. The solid circles show the excess noise for a SVX′ test ladder irradiated non-uniformly at LBL. The cross shows the excess noise for another SVX′ test ladder irradiated at TRIUMF. The star symbol shows the excess noise for a SVXII test ladder. The dotted curve shows the expected contribution from shot noise. The open circles show the noise for an unirradiated SVX′ test ladder

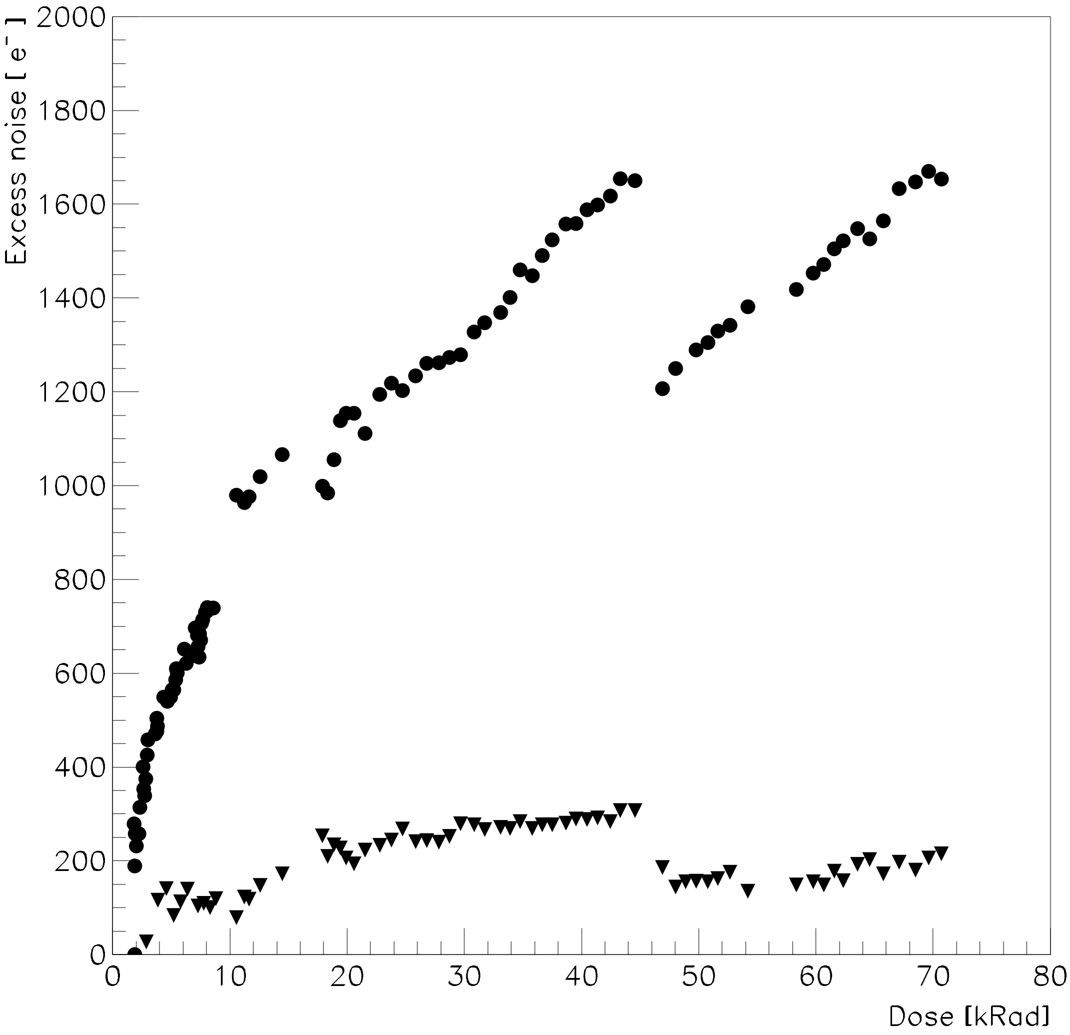

Figure 3-5. The excess noise shown as a function of the accumulated radiation dose for a particular ladder in the layers 0 and 3 of SVX′. It should be noted that the noise decreased by 15% at about 45kRad when the detector operating conditions were optimized to reduce the noise. The solid circles are for layer 3 and the solid triangles are for layer 0.

positions were calculated as the charge weighted centroid using individual strip charges and strip positions.

1. Hit Efficiency

The hit efficiency for SVX$'$ is affected by S/N, pedestals, clustering, pattern recognition, dead strips and geometrical acceptance. Since the detector has some ϕ gaps and dead strips, the hit efficiency can never be 100%. This efficiency is studied by counting tracks in the CTC which extrapolate into the SVX$'$ four layer tracking volume and have missing hits on the various layers. Our studies show a hit efficiency of about 97% for each layer. The bulk of the inefficiencies are due to micro-bonding gaps (1.7%), and the dead strips (1.7%). Figure 3-6 shows the plot of missed hits as a function of the detector z. It should be noted that peaks in the plots can be explained by the geometric acceptance of the detector.

2. Alignment and Detector Resolution

The final alignment of SVX$'$ was done using reconstructed tracks. The position resolution of a layer was determined by taking a track that also has a hit on each of the other three layers. The three hits from the other layers were fitted to a track. The distance between the intersection of the track with the layer being studied and the cluster centroid of the hit on that layer was plotted and fitted to a Gaussian. The width of the Gaussian is related to the position resolution by the relation $\sigma^2_{residuals} = \sigma^2_{position} + \sigma^2_{fit}$, where σ_{fit} is the error from the fitted track parameters. The position resolutions for one and two strip clusters in SVX$'$ were 13 and 11 μm, respectively. Figure 3-7 shows the biased residual distribution for SVX$'$. Biased residuals are found by taking a track that has 4 hits and fitting all the four hits to a track. The residuals of each layer in this case are known as biased residuals. The σ for the biased residual distribution is 8.73 μm.

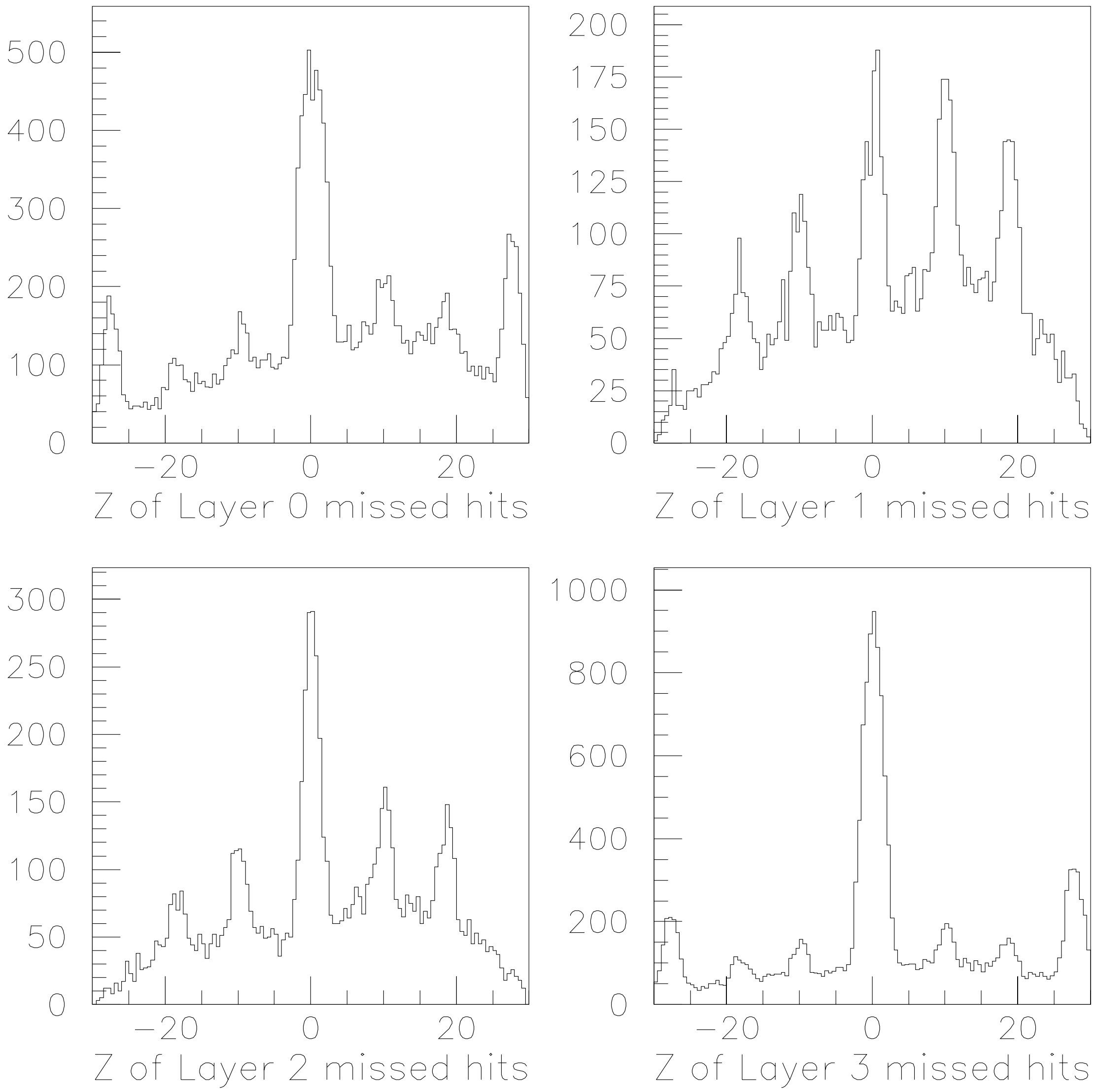

Figure 3-6. The plot of the missed hits as a function of the detector z for the four layers of the SVX$'$ barrels. The peak at z=0 corresponds to the gap between the two barrels and the other peaks correspond to the gaps due to micro-bonds.

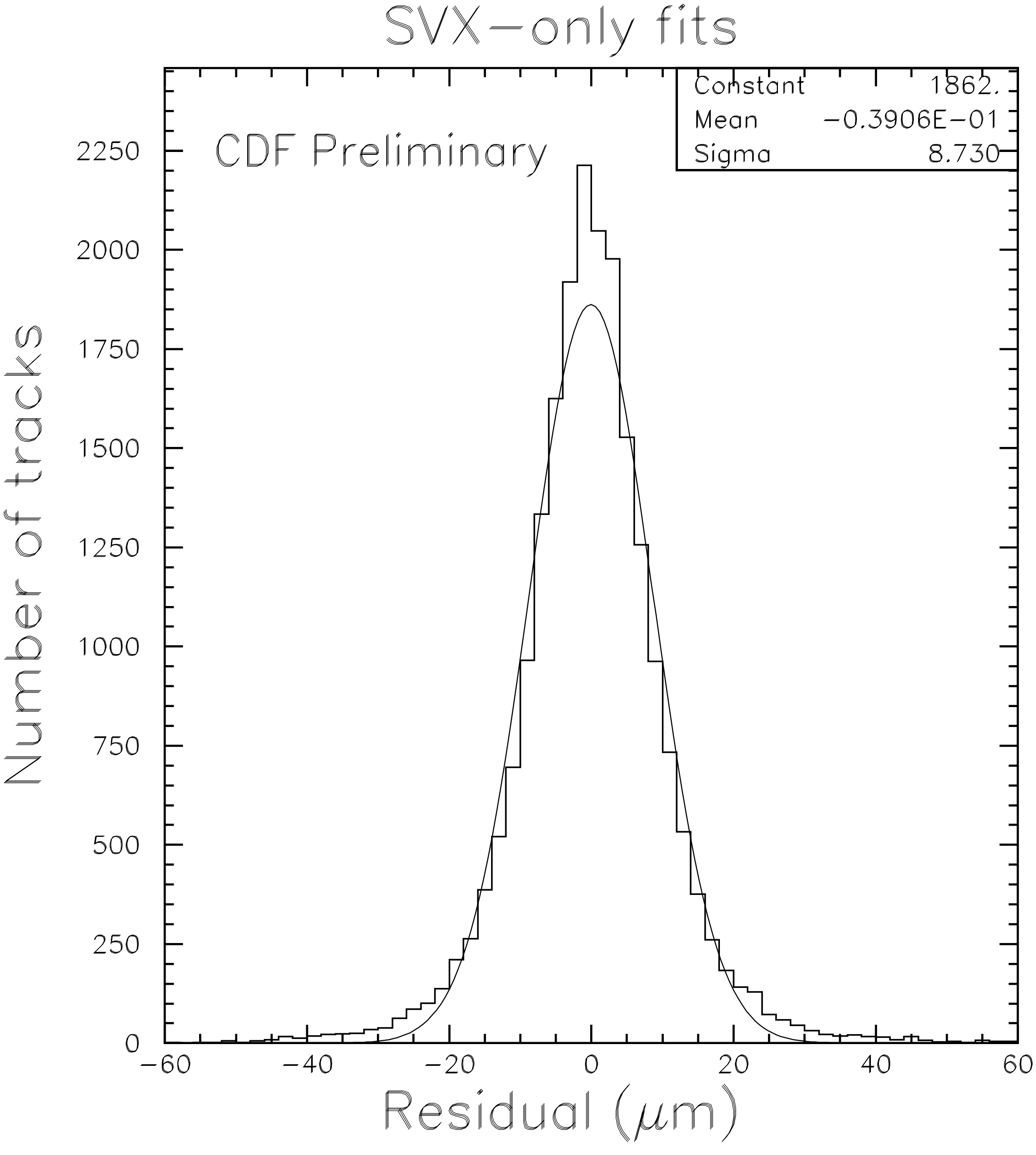

Figure 3-7. The biased residual distribution for SVX′

E. Conclusions

SVX$'$ took about 120 pb^{-1} of data and functioned within its specifications. Though an anomalous increase in the noise with the accumulated radiation dose was observed, it did not affect the detector performance adversely. The detector played a major role in the discovery of the top quark and in other searches and measurements including the search for the B_c meson.

CHAPTER 4.

Event Selection

There are over 50,000 $\overline{p}p$ interactions per second at the B0 interaction region of the Tevatron. At this rate it would be impossible to read out the detector. Hence events that are relevant to an analysis are selected by a trigger system at CDF. This chapter describes the triggers used to select events for this analysis.

A. Trigger

CDF has a three level trigger system. Levels 1 and 2 are hardware triggers constructed from printed circuit board and fastbus electronics and software control. The level 3 is a software trigger. It consists of FORTRAN programs running on a silicon graphics cluster. Each successive trigger level has more time and information to decide if the event should pass to the higher level. Events passing the level 3 trigger are written to a tape and are used for further data analysis.

1. Level 1 Trigger

The Beam Beam Counters (BBC) were described in the last chapter. If the two BBC's record a signal within a window of 15 ns around the collision time then the analog impulses from the calorimeters are summed on hardware boards to get the approximate energy patterns in the detector. The trigger also looks for muon stubs, more than two hits in the muon chambers, and uses the slope of the track in the muon chamber to get the approximate momentum of the track. This is a very rough estimate of the track momentum as compared to the momentum that can be obtained from the CTC information. However the level 1 decision should be made within 3.5 μs (the bunch crossing time), hence it is not possible to process the CTC information at this time. The uncertainty in the measurement of the track angle is 5 mrad. The uncertainty in the measurement of the momentum has not been determined. The major uncertainty in the momentum measurements is due to the multiple scattering, especially at low momentum. The level 1 efficiency as a function of the track P_t for run 1a is shown in Fig 4-1. This figure was obtained from Ref. [43]. There are about 50,000 events per second that enter the detector. Two percent of these events pass the level 1 trigger.

2. Level 2 Trigger

The level 2 trigger examines the fastout signal from the calorimeters in greater detail. It sums the impulses to find the jet energy clusters. The Central Fast Tracking (CFT) is used to process the CTC information. It finds the $r-\phi$ components of the tracks and sorts them according to their P_t with a precision of $\frac{\Delta P_t}{P_t^2} \equiv 0.035\ P_t$. This is a better measurement than that at level 1, yet it is determined from only one prompt hit out of the 12 possible hits in a layer. In level 2 the tracks are also extrapolated to the muon chambers to determine the momentum of the muons in the event. Level 2 requires that there be at least two level 1 CMU muons or one CMU and one CMX muon, or two CMX muons. One of the muons from the pair should have a matching CFT track. The CFT track should also have a P_t greater than 2.5 GeV/c. About 20 events per second pass the level 2 trigger. Figure 4-2 shows the plot of the level 2 efficiency for run 1a as a function of the track P_t [43].

3. Level 3 Trigger

The level 3 trigger is a software trigger. It uses the complete reconstruction information from the CTC to do an accurate determination of the momentum of the muons or other tracks. For the J/ψ data set the trigger requires that the muon stubs match to the CTC tracks within 4σ. In addition it is also required that the invariant mass of the two muons be between 2.8 to 3.2 GeV/c^2. About 6 events per second pass the level 3 trigger, these events are written to tape.

The trigger also requires the muons to be separated by a calorimeter tower. This requirement reduces the effects of punch-through from high energy jets which traverse through the calorimeters and leave stubs in the muon chambers.

Figure 4-3 shows the di-muon invariant mass distribution for the events passing the level 3 trigger for Run 1a and 1b . The two muons are required to have opposite charge. This figure shows that there were 544,000 di-muon pairs that passed the J/ψ trigger in run 1a and 1b.

B. Analysis cuts

The data used in this analysis were obtained from the trigger described above. This data set is known as the inclusive J/ψ data set. The signature of $B_c \rightarrow J/\psi + \mu + X$ is a displaced vertex with three muons, where two muons come from the J/ψ and the third comes from the B_c. A set of cuts was applied to the data to select such tri-muon events. The summary of such cuts is listed in the Table 4-1 and is described in detail in the following sub-sections.

1. Muon Selection

Muons from all the central muon chambers (CMU, CMP and CMX) were used in this analysis. These muons were required to have SVX tracks. In the track reconstruction the muon's CTC track is projected to the muon chambers and is matched with the stubs in the chamber. P_t dependent corrections for the effects like multiple scattering and energy losses are taken into consideration. The reconstruction program calculates the matching χ^2 for the tracks. The different cuts on the χ^2 for the various muon types are listed in Table 4-1. The minimum P_t of the selected muons is required to be greater than 1.4 GeV/c. Muons with P_t less than this will not be able to traverse to the central muon chambers due to the dE/dx losses in the material before the chambers.

2. J/ψ Selection

The two muons selected to make a J/ψ should be CMU, CMU/CMP, CMX or CMU/CMX muons. CMU/CMP muons are required to have hits in both the CMU and the CMP muon chambers. The CMU/CMX muons are required to have hits in the the CMU and the CMX muon chambers. The two muons should have opposite charge. The muon pair is required to pass the J/ψ trigger. The tracks belonging to the two muons are fitted to a vertex (vertex constraint) using a fitting program called CTVMFT [44]. The invariant mass of the two tracks after the vertex constraint is required to be within 50 MeV/c^2 of the J/ψ world average mass from the Particle Data Book [19]. The P_t of the J/ψ is required to be greater than 4.0 GeV/c.

3. Cuts on the μ from the B_c

The muon from the B_c (also called the third muon) is required to be a CMU/CMP muon and should have a P_t greater than 3.0 GeV/c. The third muon is restricted to only the CMU/CMP muons in order to reduce the background from hadron punch-through. This is so because the a CMU/CMP muon has to travel the most amount of steel in order to reach the muon chambers. This issue will be described in greater detail in the following chapter.

4. Cuts on the Three Track Vertex

The three tracks from the three muons are fitted to a vertex using CTVMFT. In the fit the invariant mass of the tracks belonging to the J/ψ muons is constrained to the world average J/ψ mass. The three tracks are constrained to a vertex with a Probability(χ^2) greater than 1%. The J/ψ and the third muon are required to be in the same hemisphere. This cut is applied to reduce the background from the $b\bar{b}$ events. The $c\tau^*$ of the three track vertex was required to be greater than 60, 85 and 100 microns. Where $c\tau^*$ is given by

$$c\tau^* = \frac{\mathrm{Mass}(J/\psi + \mu)}{|P_t(J/\psi + \mu)|} L_{xy}(J/\psi + \mu) \tag{4-1}$$

where $L_{xy}(J/\psi + \mu)$ is the distance between the primary and the $J/\psi + \mu$ vertex in the $x - y$ plane.

5. $J/\psi - K$ Selection

The results of this analysis are presented as the ratio of the cross-section times branching ratio for the $B_c \rightarrow J/\psi + \mu + X$ to the cross-section times branching ratio for the $B \rightarrow J/\psi + K$ for different assumed B_c lifetimes. The $B \rightarrow J/\psi K$ events are selected in the same way as the B_c events. However the third track is required only to be a CTC track and is not required to have any stubs in the muon chambers. The $c\tau$ cut on the three track vertex for the $J/\psi - K$ events is required to be 100 μm.

6. Covariance scaling

There was a time dependent degradation of the CTC during the period of the data taking. This degradation was incorporated in the analysis by scaling the error covariance matrix for the CTC tracks. For Run 1a the scale factor was set to 2.0 and for Run 1b the scale factor was set to 2.4 .

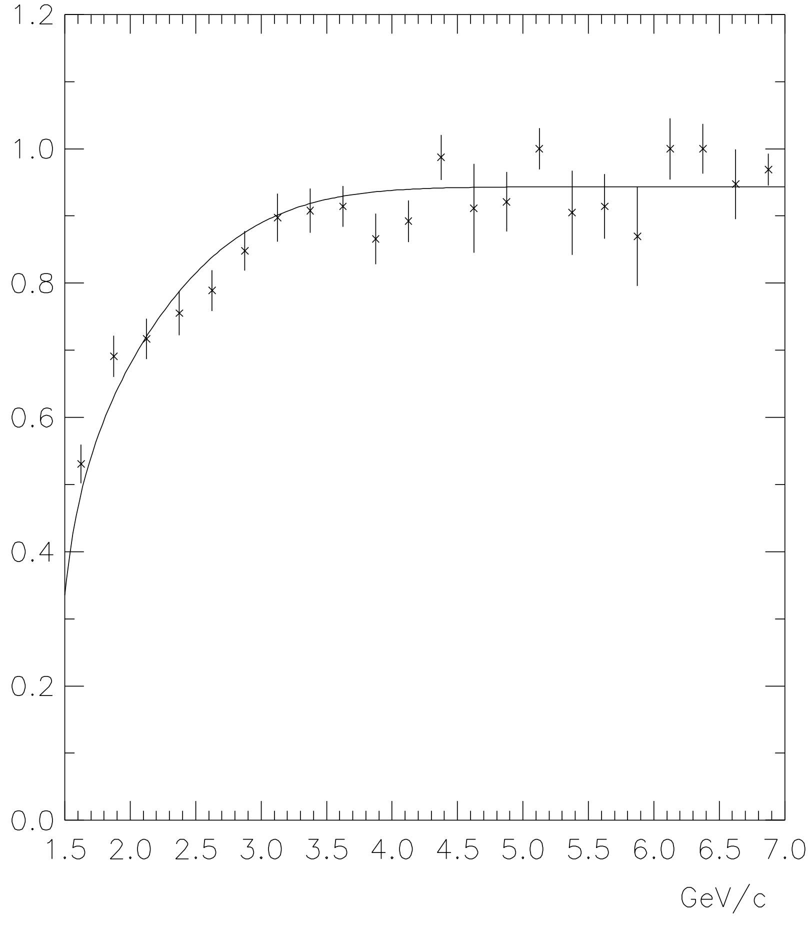

Figure 4-1. The level 1 trigger efficiency for a muon as a function of their P_t.

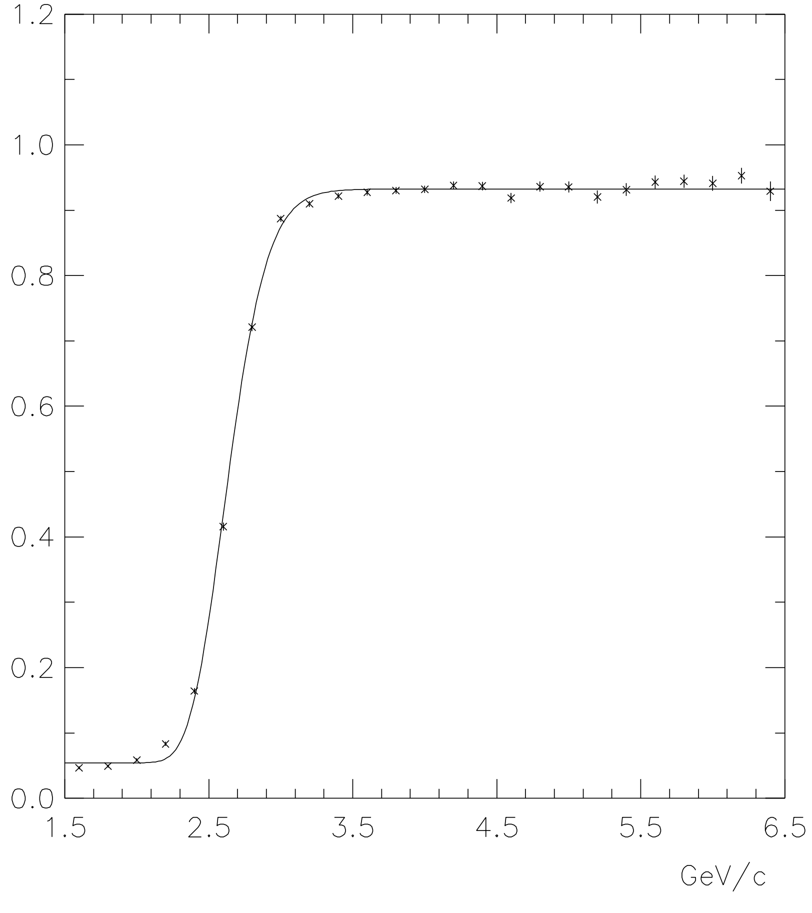

Figure 4-2. The level 2 trigger efficiency for the muons as a function of their P_t

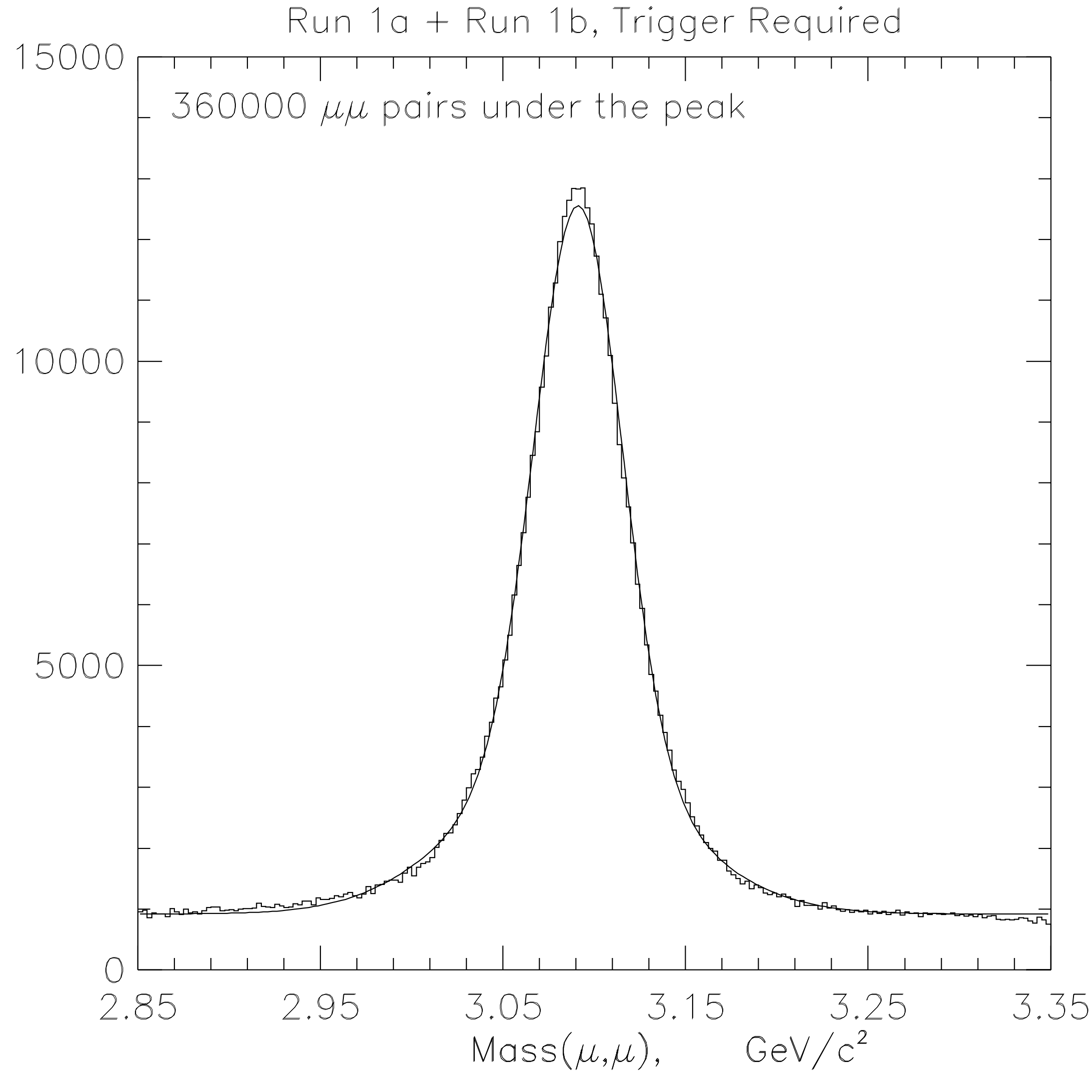

Figure 4-3. The di-muon mass distributions from Run 1a and 1b. The two muons in the pair should have opposite charge. The pair is required to pass the J/ψ trigger. The y axis shows the number of events per bin.

Table 4-1. Summary of the cuts used in the analysis.

	Cuts
Muon Selection	$\chi^2_x < 9$ and $\chi^2_z < 12$ for CMU, CMU/CMP and CMU/CMX muons $\chi^2_x < 9$ For CMX muons Muon $P_t > 1.4$ GeV/c
J/ψ Selection	Muon types allowed CMU, CMU/CMP, CMX, CMU/CMX Di-muon pair should pass the J/ψ trigger Both the muons should be SVX muons. J/ψ mass should be within 50 MeV of the PDG J/ψ mass. J/ψ $P_t > 4.0$ GeV/c CTVMFT is used to fit the muons to a vertex.
Third muon.	Third muon should be CMU/CMP muon. Third muon $P_t < 3.0$ GeV/c It should be a SVX muon.
Three track vertex	CTVMFT is used to fit the two tracks to a vertex. J/ψ muons are mass constrained to the PDG J/ψ mass. The three tracks are vertex constrained with Prob(χ^2) > 1% J/ψ and the third muon are required to be in the same hemisphere and $c\tau^* > 60, 85, 100$ μm.
Cuts on $J/\psi K$	K $P_t > 3.0$ GeV/c K track should point to the CMU/CMP fiducial region K track should be a SVX track Prob(χ^2) of the vertex fit be > 1% J/ψ and K should be in the same hemisphere $c\tau > 100$ μm.
Covariance scaling	In Run-1a the scale factor is set to 2.0 In Run-1b the scale factor is set to 2.4

CHAPTER 5.

Physics Analysis

A. Introduction

One cannot look for a definite resonance peak in the three muon invariant mass spectrum to establish the existence of the B_c. There is a missing energy, in the final decay products of the B_c due to at least one missing neutrino. Because of the missing energy the three muon invariant mass spectrum is very broad. The broad mass distribution makes the search dependent on the accuracy of the background estimates. This chapter describes the Monte Carlo studies used to determine the search region in the mass spectrum and the methods used to determine the various backgrounds to this search.

B. Monte Carlo Studies

B_c events were generated using a Monte Carlo program called the BGENERATOR [45]. There are two processes in BGENERATOR; NDE and MNR. The NDE process involves the generation of a single b quark according to the parameterization of the next-to-leading-order calculation by Nason, Dawson, and Ellis [46] and then the subsequent fragmentation of the b quark to a single B meson. The MNR process produces $b\bar{b}$ pairs using the input spectra from the MNR Monte Carlo [47] and the $b\bar{b}$ quarks are fragmented to $B\bar{B}$ mesons pairs. We generated single B_c's. The B_c's generated were forced to decay into $J/\psi+\mu+\nu$ using the CLEOMC Monte Carlo program [48]. CLEOMC uses the experimental data from the the CLEO experiment to establish the decay of the generated particles. The program has been adapted to the CDF environment. We used the ISGW [49] model for the semileptonic decay with unpolarized daughters.

The CDF detector was simulated using QFL [50]. The QFL simulation package provides a fast and a reliable detector simulation for high statistics physics and acceptance calculations. It parameterizes the detector response rather than derive it from first principles. Data from QFL were passed through the trigger simulation using the DIMUTG module [43, 51]. DIMUTG parameterizes the turn on curves for the various levels of the J/ψ trigger and uses them to decide if the muons have passed the trigger. In BGENERATOR the minimum b quark P_t was required to be greater than 5 GeV/c. The B_c mass was set to 6.258 GeV/c^2 and its lifetime was set to 0.6 ps.

The difficulty in searching for $B_c \rightarrow J/\psi + \mu + X$ decays is that there is at least one neutrino which is undetectable. Therefore, the invariant mass distribution of the three muons is very broad. Figure 5-1 shows such a mass plot made from the generator level (GENP) information (i.e., before the detector simulation). Studies were done to see if we could extract the B_c signal by looking at the sharp cut-off peak in the transverse mass plot of the B_c [52]. Such a peak was seen in the transverse mass plot from the GENP information. However after the detector simulation the peak vanished due to inadequate resolutions of the primary and the secondary vertices. We decided to use the tri-muon mass distribution to search for the B_c meson. Figure 5-2 shows the three muon invariant mass distribution after the detector and trigger simulation. This figure also shows that the region of the search would be limited by the J/ψ mass at the low end and the B_c mass at the high end. The P_t distributions of the $J/\psi + \mu$ system and then only the third muon from the B_c are shown in Fig. 5-3. The P_t of the third muon from the B_c is cut at 3 GeV/c . Figure 5-4 shows the L_{xy} and the $c\tau^*$ distribution for the $J/\psi + \mu$, where L_{xy} is the distance between the primary and the secondary vertices in the xy plane. The impact parameter and the impact parameter significance for the third muon from the B_c is shown in Fig. 5-5.

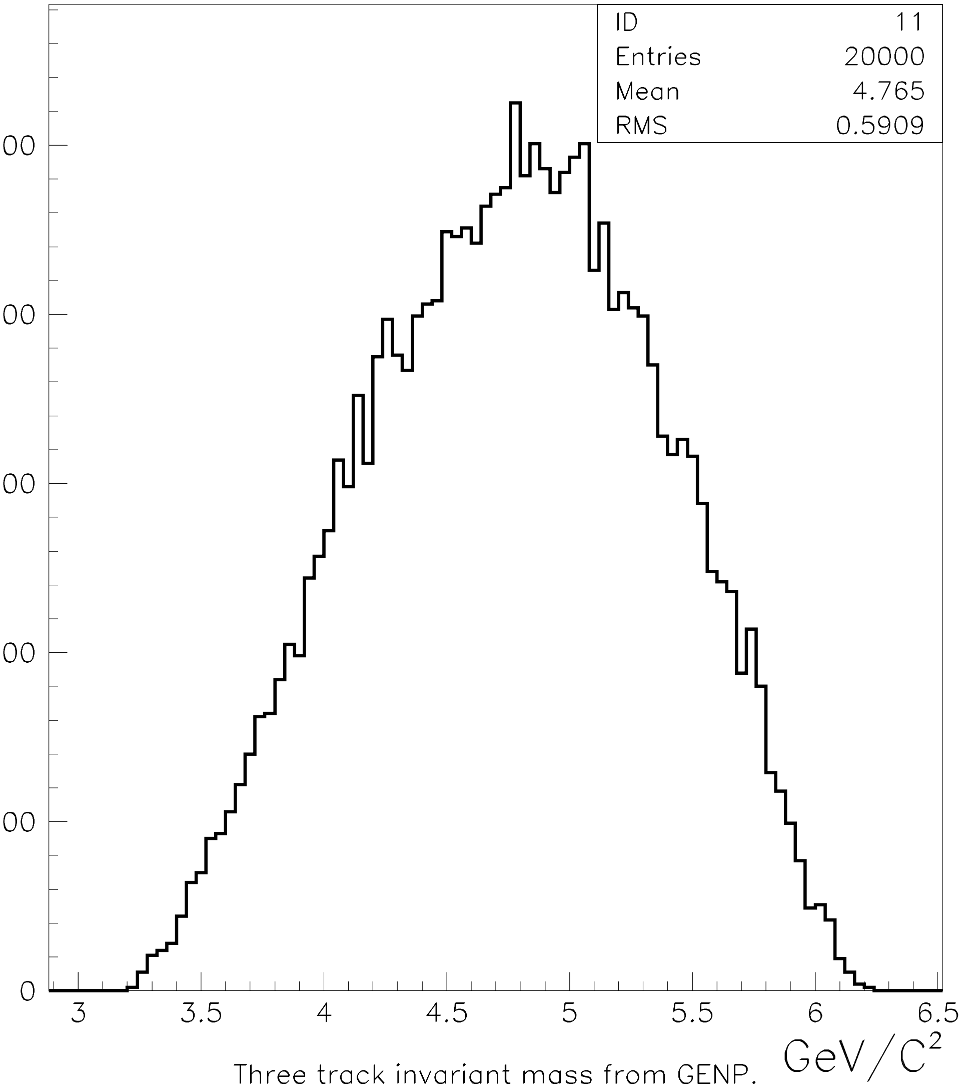

Figure 5-1. The $J/\psi + \mu$ invariant mass distribution before the detector and the trigger simulation. The y axis shows the number of events per bin.

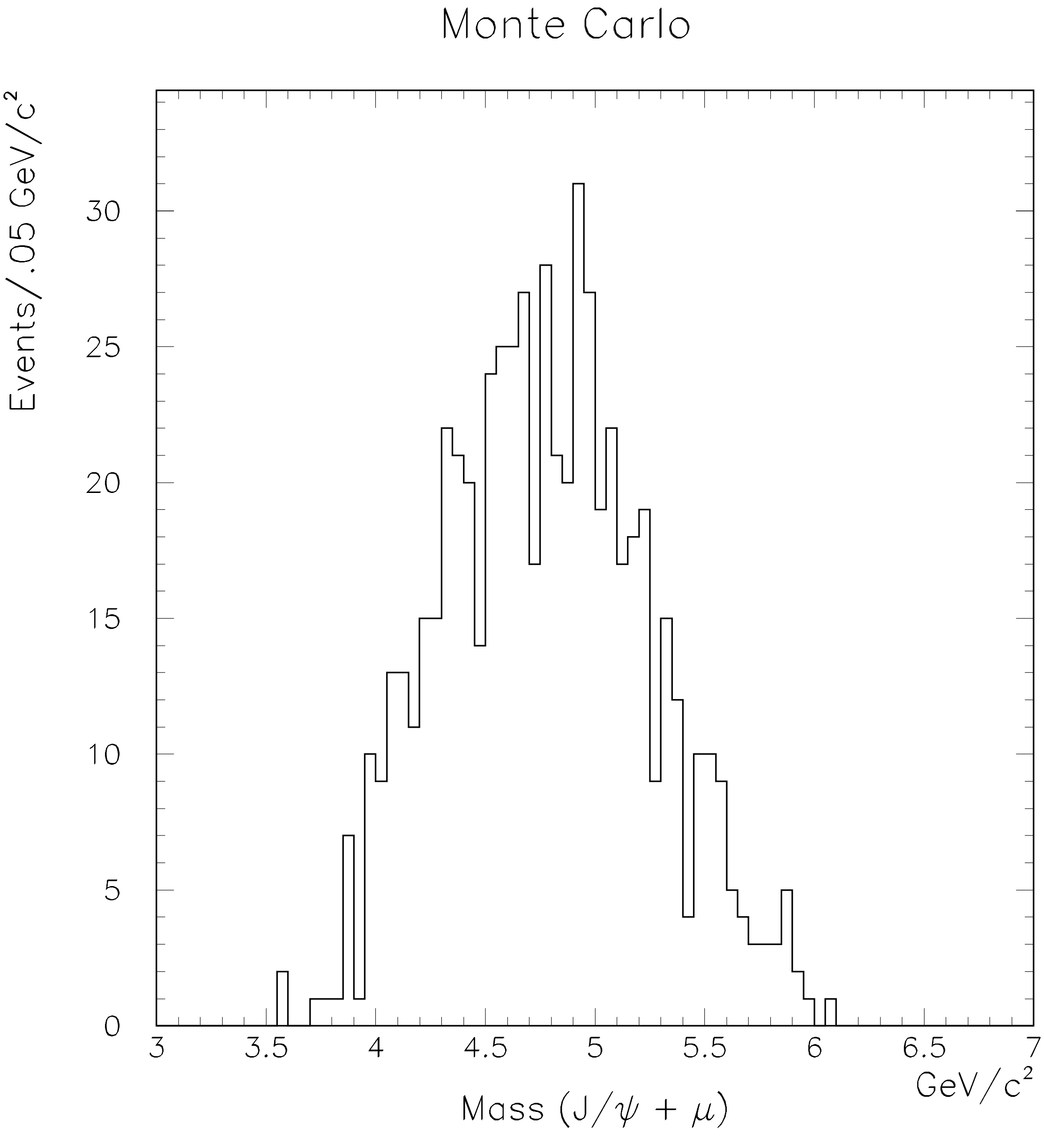

Figure 5-2. The $J/\psi + \mu$ invariant mass distribution after the detector and the trigger simulations.

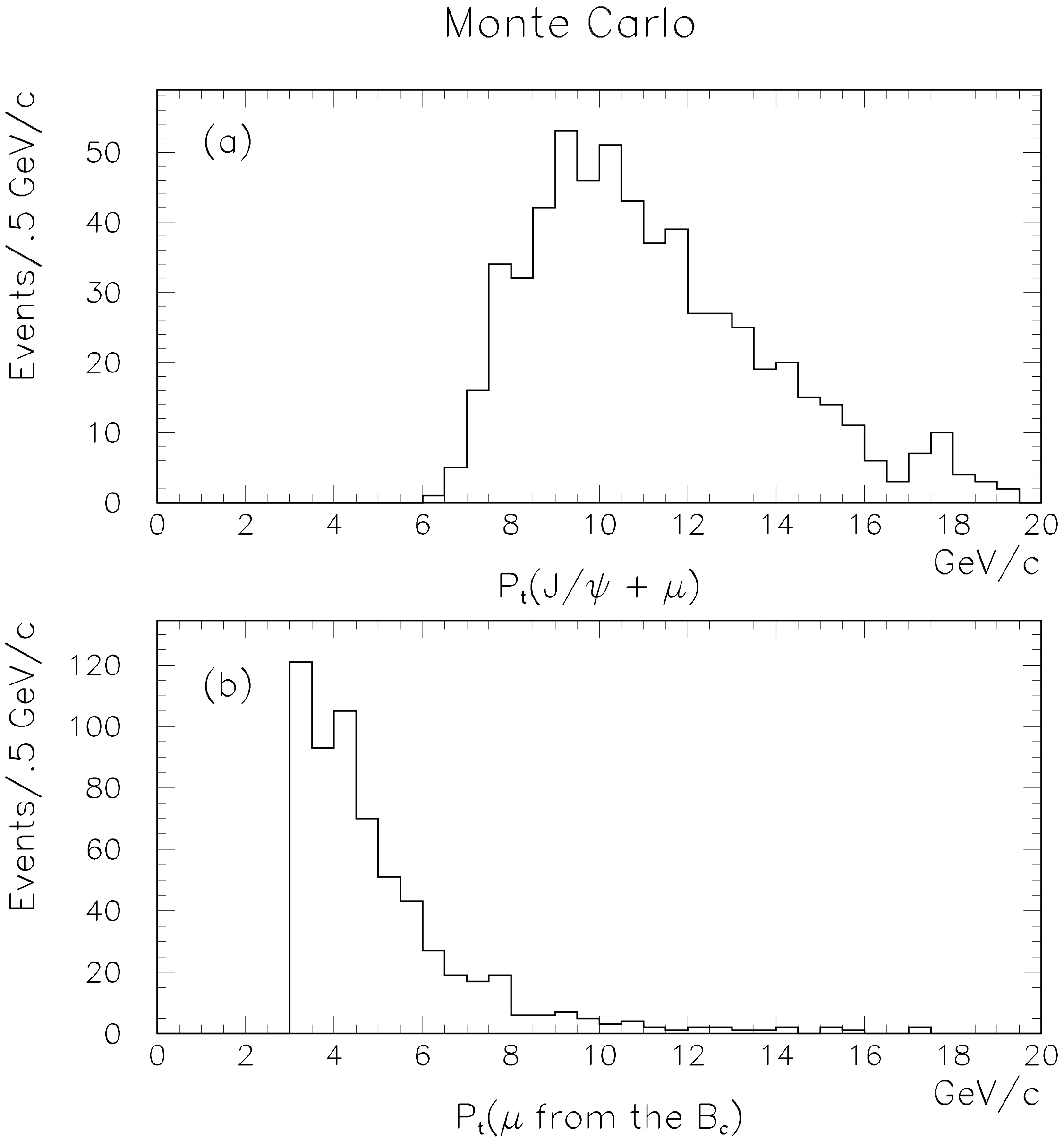

Figure 5-3. (a) P_t spectrum of $J/\psi + \mu$ from Monte Carlo. (b) P_t spectrum of the third muon from Monte Carlo.

C. Events in the Signal Region From Data

The aim of the analysis was to look for events with three muons from a secondary vertex. For the purpose of this analysis the invariant mass range of interest for the three tracks was defined to be between 4 and 6 GeV/c^2. This range was chosen after looking at the three track invariant mass distribution from the Monte Carlo. The primary vertex for the events was obtained from the run average beam position and the errors on it were set to 40 μm. The vertex fitting was done using CTVMFT. In CTVMFT the two J/ψ muons were mass constrained to the world average J/ψ mass. However, since these events are not fully reconstructed the CTVMFT was not required to constrain the vector sum of the momenta of the daughter muons to the primary vertex. The cuts used in this analysis have already been described in Chapter 4 and are summarized in Table 4-1.

The combined Run 1a and Run 1b J/ψ mass distribution is shown in Fig. 5-6. There are 196000 ± 1400 events under the peak. Figure 5-7 shows the invariant mass distribution of J/ψ and the third muon in the signal region for Run 1a and Run 1b for a $c\tau^*$ cut of 60 μm. The P_t spectra of the $J/\psi + \mu$ and the P_t of the third muon from the B_c are plotted in Fig. 5-8. Figure 5-9 shows the cτ^* and the L_{xy} distribution of $J/\psi + \mu$. Figure 5-10 shows the impact parameter and impact parameter significance distribution for the third muon from the B_c. The number of events in the signal region with different $c\tau$ cuts for Run 1a and Run 1b are summarized in Table 5-1.

Table 5-1. Summary of the events in the signal region for Run 1a and Run 1b

$c\tau^*$ cut μm	Run 1a	Run 1b	Run 1a + Run 1b
60μm	3	14	17
85μm	3	11	14
100μm	2	11	13

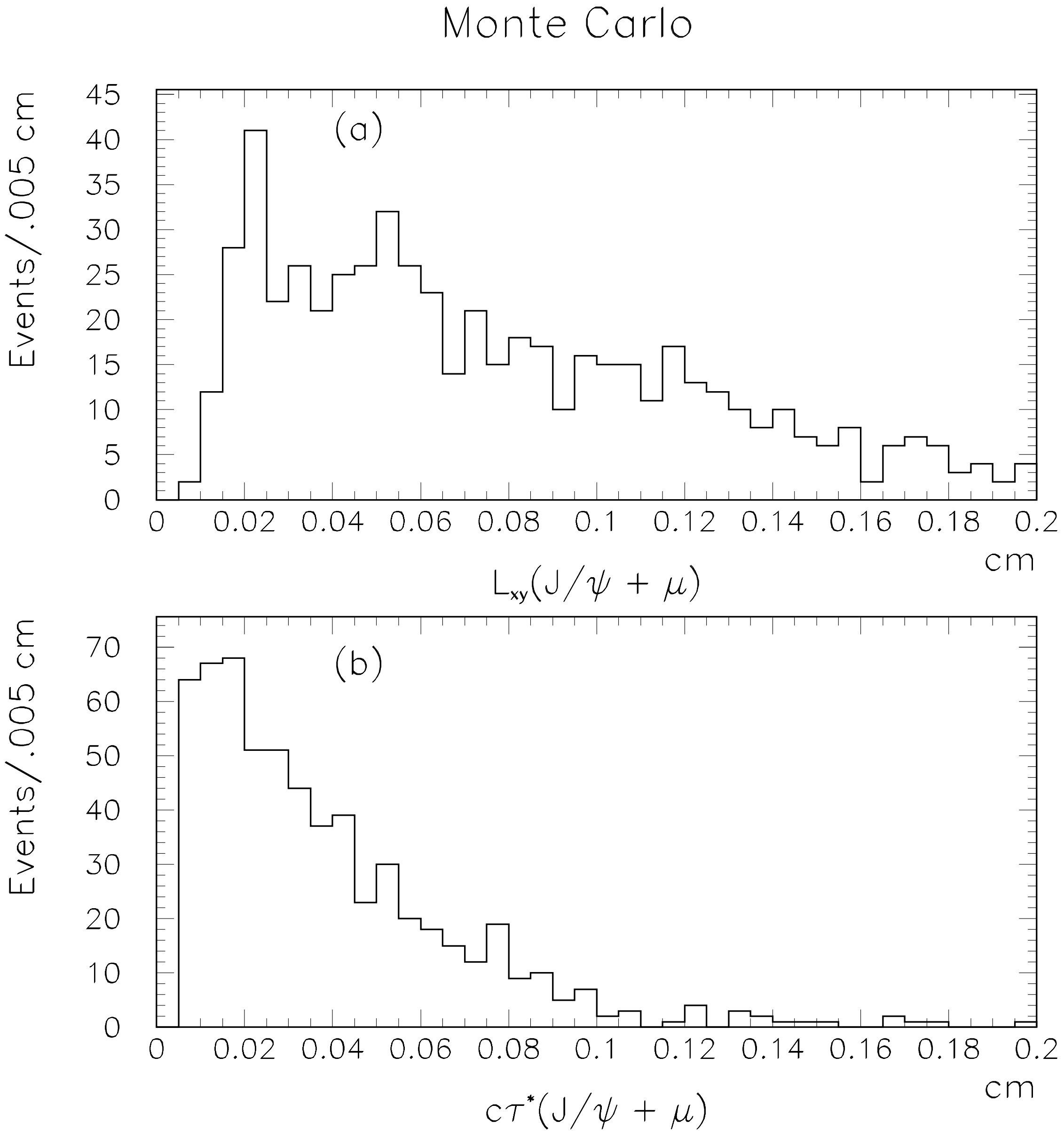

Figure 5-4. (a) The L_{xy} distribution for $J/\psi + \mu$ from Monte Carlo. (b) The pseudo $c\tau$ distribution for $J/\psi + \mu$ from Monte Carlo.

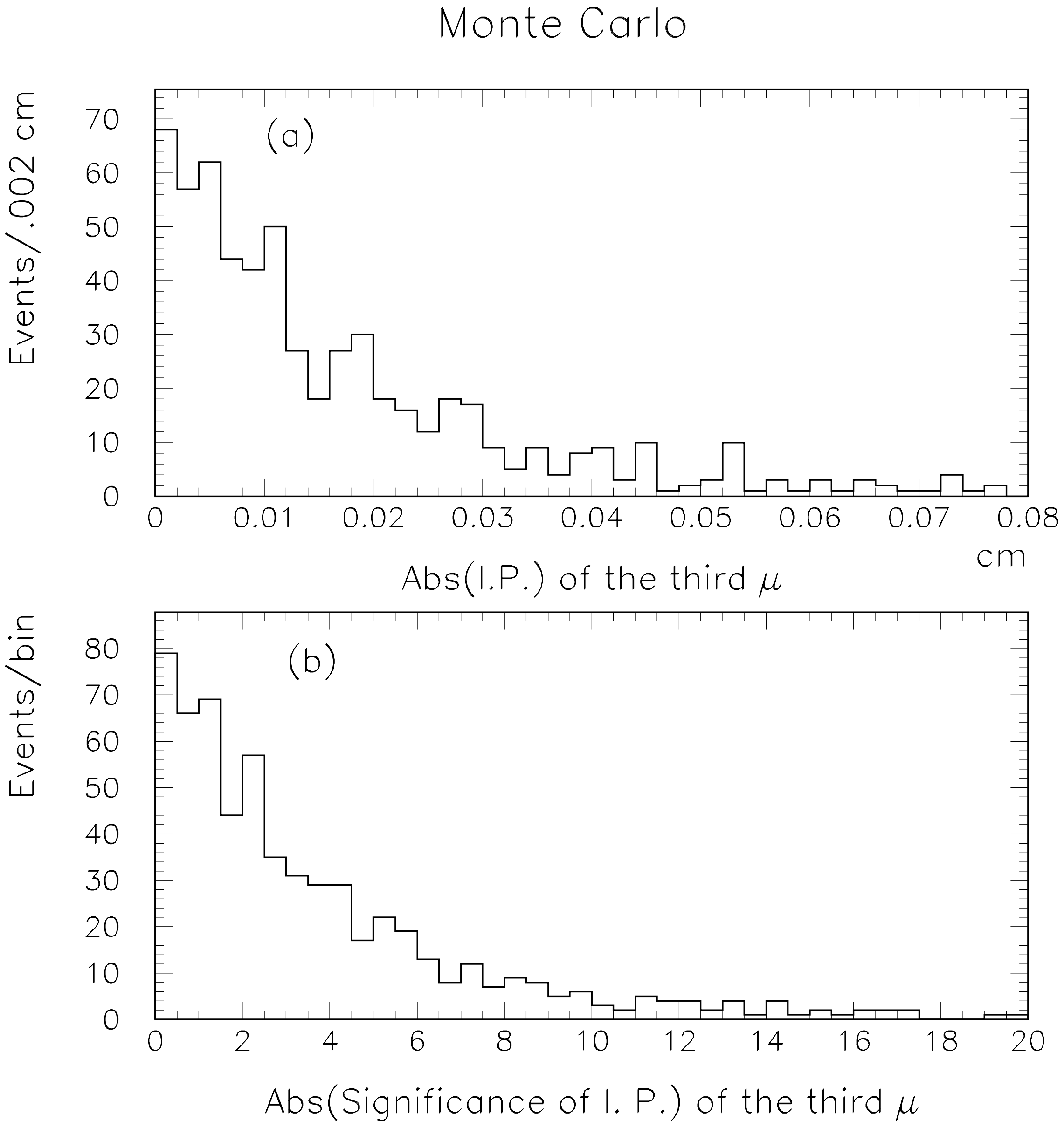

Figure 5-5. (a) The impact parameter distribution of the third muon from Monte Carlo. (b) The impact parameter significance distribution of the third muon from Monte Carlo.

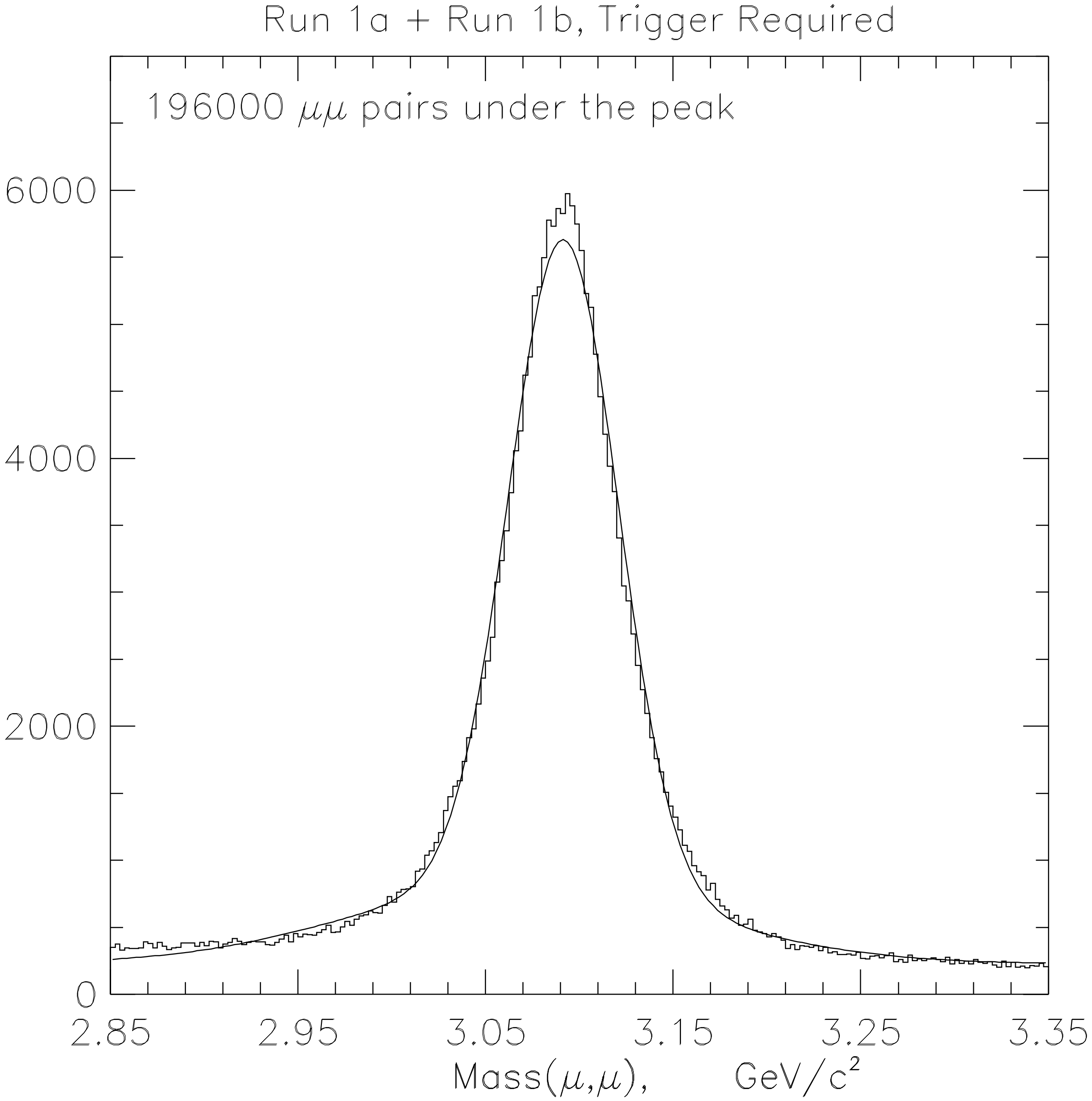

Figure 5-6. The J/ψ mass plot for Run 1a + Run 1b; the J/ψ's are required to pass all the cuts described for the J/ψ's in Table 4-1. The histogram is fitted to two Gaussians (the solid curve) There are 196,000 ± 1400 events under the peak.

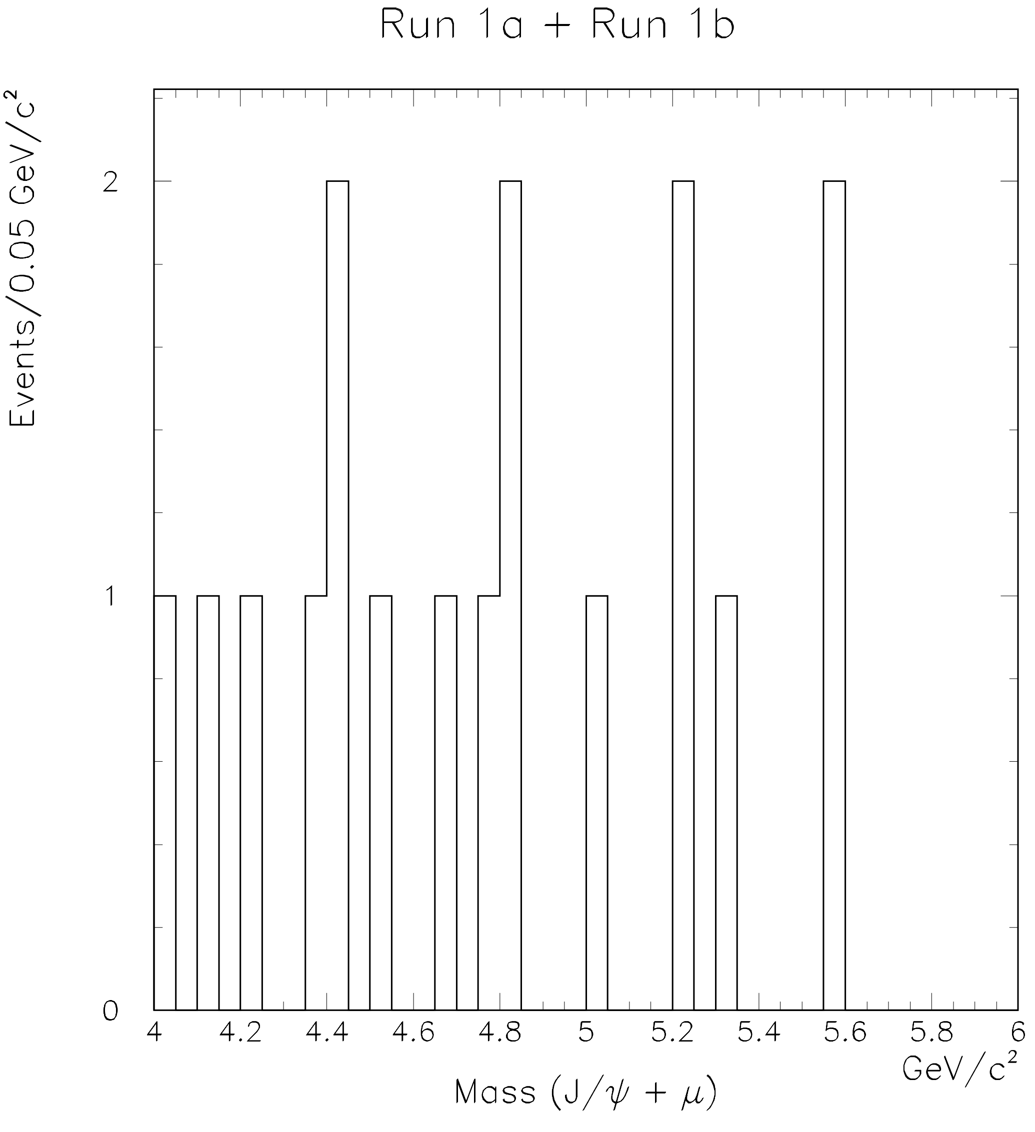

Figure 5-7. The $J/\psi + \mu$ invariant mass plot for Run 1a and 1b data. There are 17 events in the signal region. The $c\tau^*$ cut used to make this plot is 60μm.

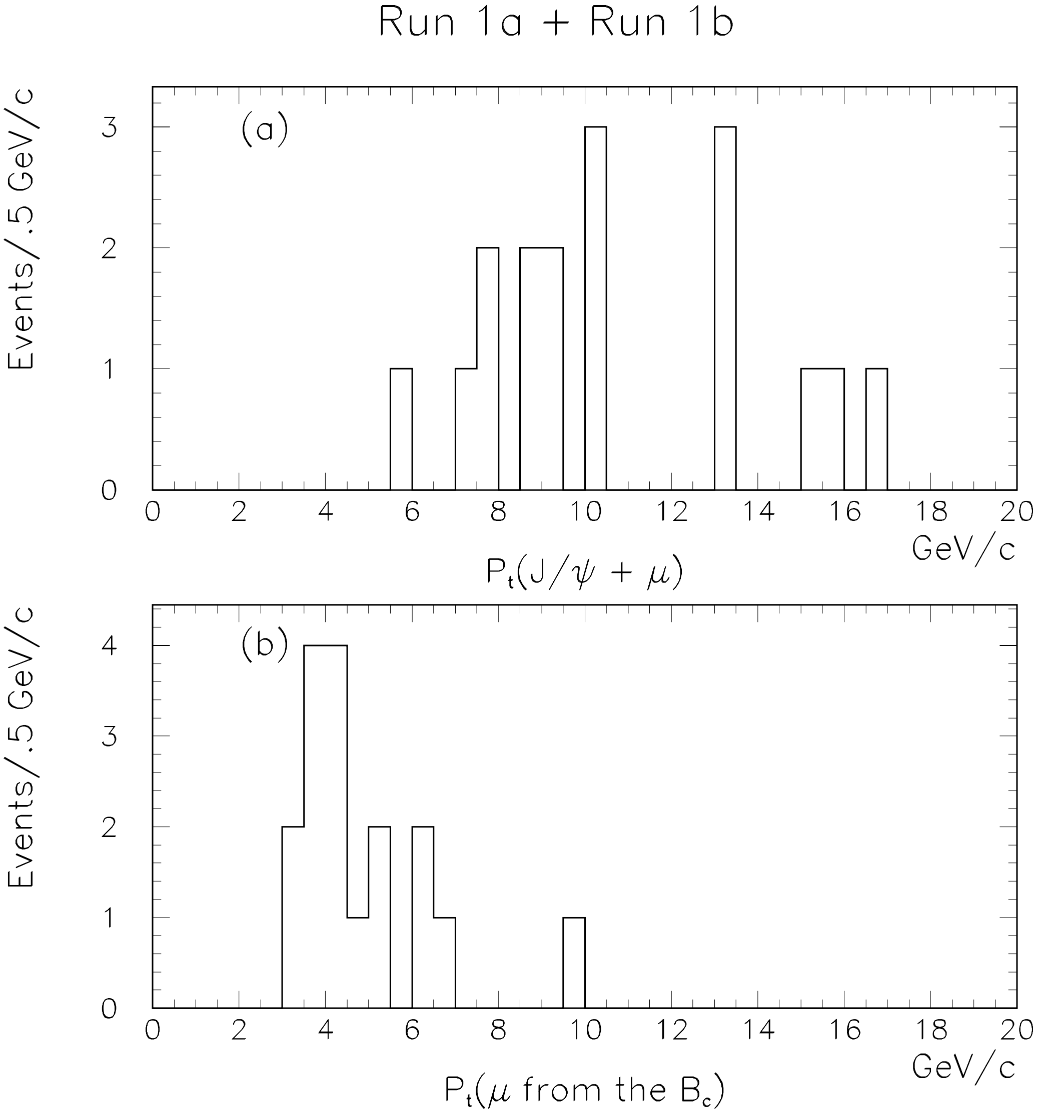

Figure 5-8. (a) The P_t spectrum of $J/\psi + \mu$ for Run 1a and 1b data. (b) The P_t spectrum of the third muon for Run 1a and 1b data.

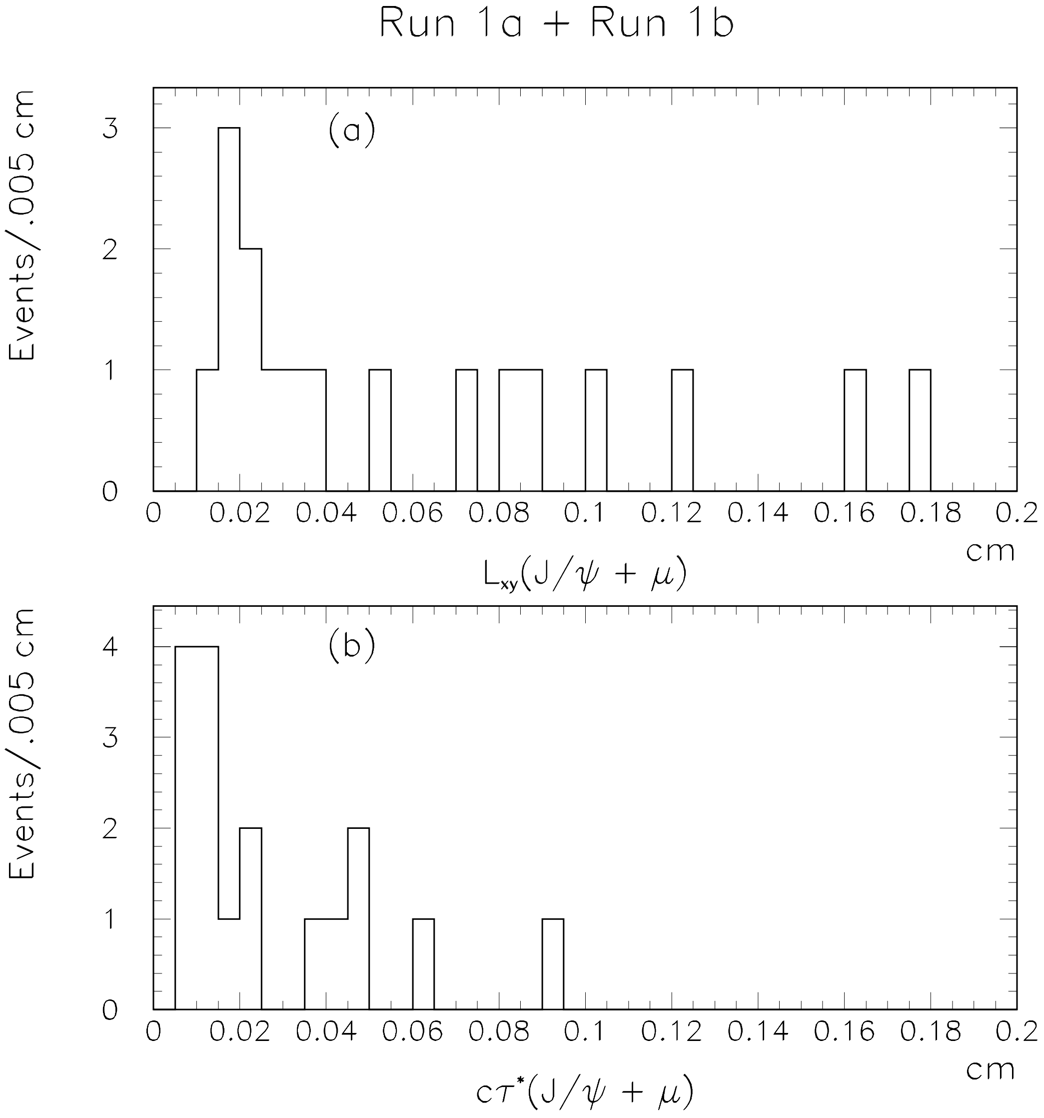

Figure 5-9. (a) The pseudo $c\tau$ distribution for $J/\psi + \mu$ vertex for Run 1a and 1b data. (b) The L_{xy} distribution for $J/\psi + \mu$ vertex for Run 1a and 1b data

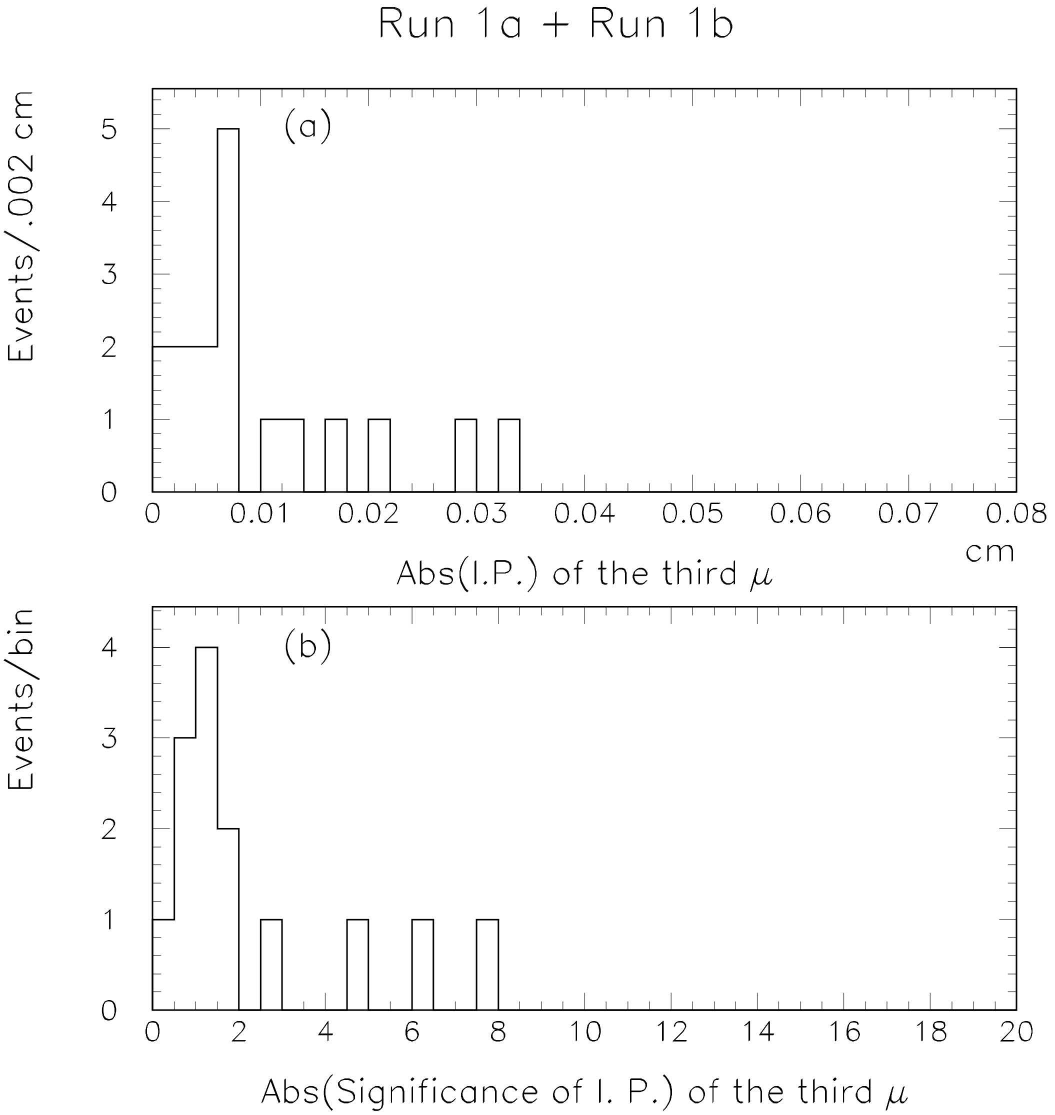

Figure 5-10. (a) The impact parameter distribution of the third muon for Run 1a and 1b data. (b) The impact parameter significance distribution of the third muon for Run 1a and 1b data

D. Background

The events observed in the signal region in the data have a contamination from background events. In this section we describe the methods used to determine the various background contributions to the data events in the signal region. The irreducible background in this channel is likely to come from fake muons (punch-trough and decay in flight), mis-measured tracks, and the normal $b\bar{b}$ events. Fake J/ψ's also contribute to the background. They can contribute in two ways, (1) fake J/ψ and fake muon and (2) fake J/ψ and a good muon. Case (1) is automatically included in our background estimates for the fake muons. Case (2) is too small (<.2 events) and is ignored in the overall estimate of the background.

1. $B\bar{B}$ Background

a. Introduction.

$B\bar{B}$ pairs produced during the $p\bar{p}$ collisions can mimic the B_c signature. This happens when one of the B's produced decays into J/ψ + X and the other B decays into μ + X. Furthermore if the J/ψ decays into a $\mu\mu$ pair then there would be three muons in the event. In a few cases these muons may make a vertex that passes our vertex cuts. If such an event also passes the other cuts of our analysis, it would be an irreducible background to the B_c signal.

b. Estimate of the $B\bar{B}$ background.

This background was estimated by using Monte Carlo. $B\bar{B}$ pairs were generated using BGENERATOR and CLEOMC was used to decay the particles. One of the B's was forced to decay into J/ψ + X and the other was allowed to decay naturally. The detector was simulated using QFL and the simulated data were required to pass the dimuon trigger. The analysis code was run on the simulated data. Any contribution from decay in flight and punch through to the events picked up by the analysis code were removed. The resulting number of events was then the $B\bar{B}$ background for the generated Monte Carlo. This number was normalized to data by using the number of J/ψ's from B's in data. The normalization factor is defined as

$$R = \frac{N_{J/\psi}^{data}}{N_{J/\psi}^{MC}} \times F_B, \tag{5-1}$$

where F_B is the fraction of the J/ψ's in data that come from B's, $N_{J/\psi}^{data}$ is the number of J/ψ's passing our cuts in data and $N_{J/\psi}^{MC}$ is the number of J/ψ's in the Monte Carlo sample. $F_B = 19.6 \pm 1.5\%$ [34].

Since the SVX and the triggers are different for the two runs, the $B\bar{B}$ Monte Carlo data were generated for both Run 1a and Run 1b. We obtain R as 0.117 for Run 1a and 0.357 for Run 1b. The number of the background events was obtained by using the following formula:

$$\text{Number of Background events} = N_{J/\psi+\mu}^{MC} \times R$$

Where $N_{J/\psi+\mu}^{MC}$ is the number of tri-muon events picked up by the analysis code when it was run on the $B\bar{B}$ Monte Carlo. Table 5-2 summarizes the $B\bar{B}$ background for various $c\tau^*$ cuts for both the runs.

Table 5-2. Summary of the $B\bar{B}$ background for Run 1a and Run 1b. The errors reported are obtained by adding the statistical and the systematic errors in quadrature.

$c\tau^*$cut	Run 1a	Run 1b	Run 1a + Run 1b
60μm	0.23±0.16	1.07±0.62	1.30±0.64
85μm	0.23±0.16	1.07±0.62	1.30±0.64
100μm	0.23±0.16	0.71±0.51	0.94±0.53

c. Systematic Error.

The major systematic errors in this estimate come from F_B and the trigger simulation. The systematic error due to F_B is 7.7% was obtained from Ref. [35]. The error due to the trigger simulation was taken to be the difference in the calculated $B\bar{B}$ background with and without the trigger. It was estimated to be 4%. The total systematic error for this estimate was therefore 8.6%.

2. Punch through Background

a. Introduction.

An event that can mimic $B_c \rightarrow J/\psi + \mu + X$ is a J/ψ produced along with another particle that travels through the calorimeter and the steel upstream of the muon chambers without showering. This background is called the punch through background. This probability to punch through is about 2×10^{-3}; however, there are a large number of tracks meeting the cut requirements and this tends to offset the fact that most of the particles will be absorbed before reaching the CMP.

b. Estimate of the Punch Through Background.

In order to estimate the punch through background, the analysis code was first run on the data without requiring that the third track be a muon. All of the analysis cuts that make sense to apply to a non-muon third track are then applied to the resulting sample of J/ψ+track events, including the requirement that the track be pointing to the CMU+CMP fiducial region.

Shown in Fig. 5-11 is the J/ψ+track distribution where the additional track is assumed to be a muon for the purposes of determining its mass. The data in this histogram are from Run 1b only and the J/ψ was required to pass the dimuon trigger. One can see a definite peak due to $B \rightarrow J/\psi + K$ events where the kaon has been assigned a muon mass.

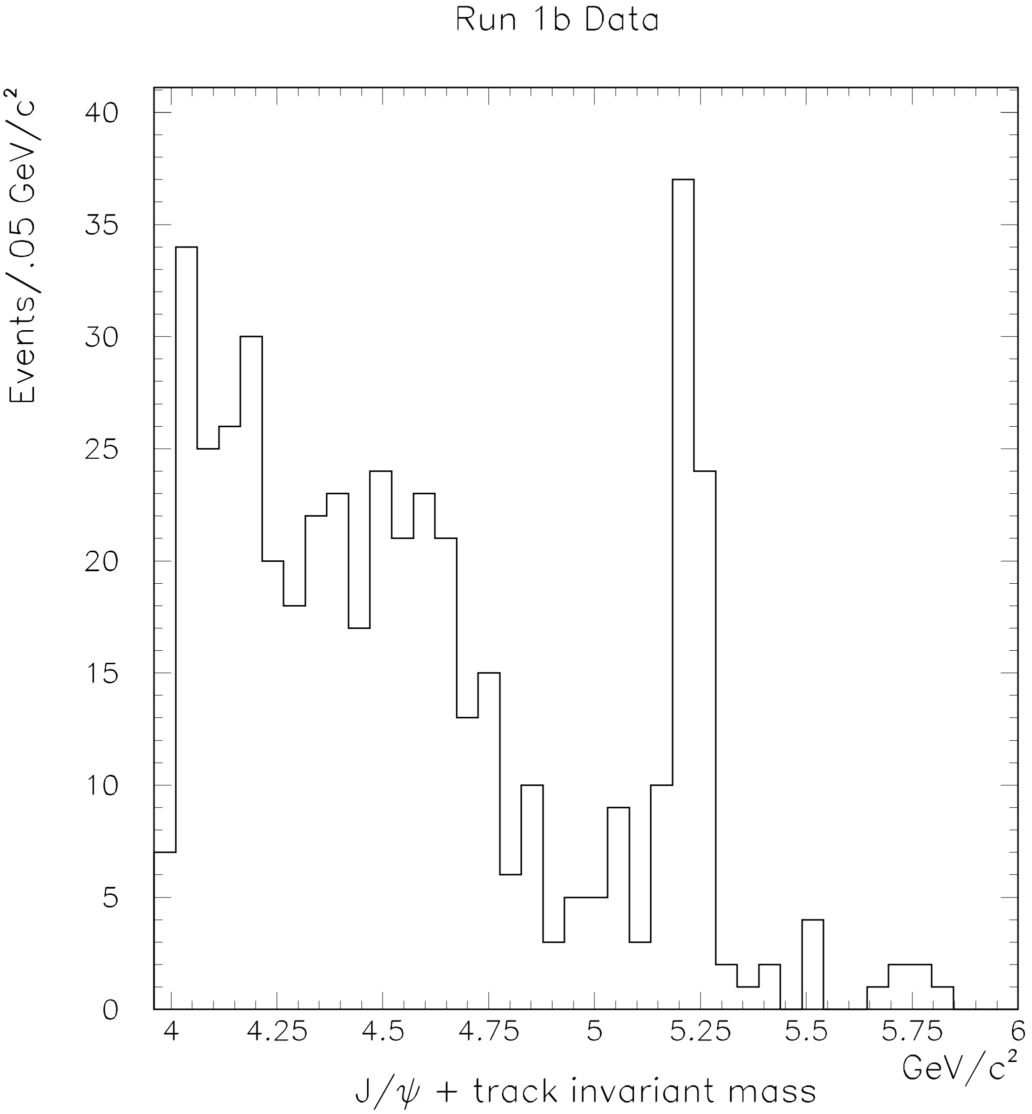

Figure 5-11. The total number of J/ψ+track candidates prior to requiring hits in the muon chambers. These events are the potential contributors to the punch through and the decay in flight background. One can clearly identify the peak caused by $B \to J/\psi + K$ events where the kaon has been called a muon. The overall shape of this curve would also be the shape of the three track invariant mass distribution for the background.

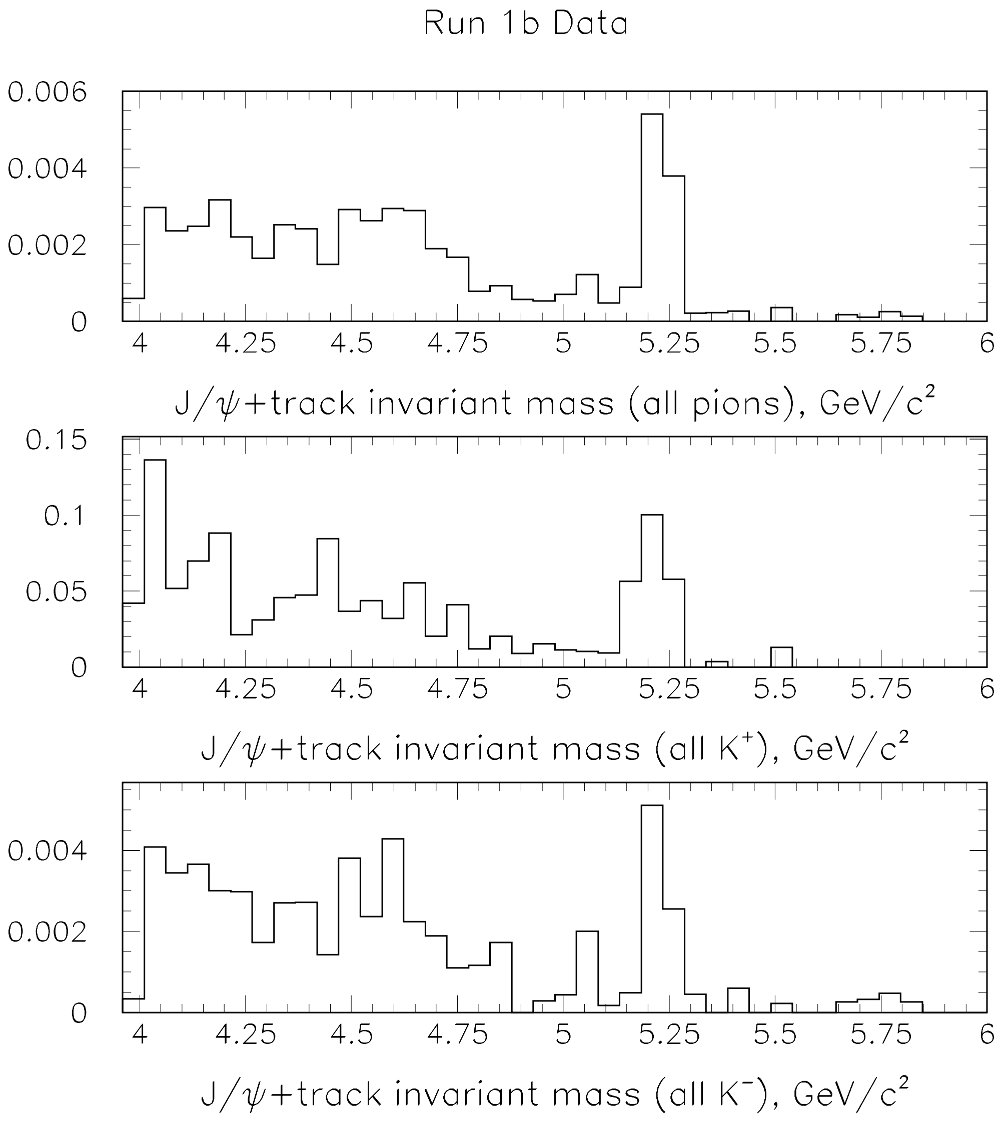

Figure 5-12. The total number of J/ψ+track candidates expected from fake muon background due to punch through. The top histogram assumes that all the tracks are pions whereas the middle and lower plot assumes that all of the third tracks are kaons (positive and negative respectively). The events are weighted by the punch through probability for each track. Adding up the weighted entries in each plot, we get 0.23 events if we assume that all the tracks were pions and 1.77 events if we assume that all the tracks were kaons.

An accounting of the amount and kinds of materials in the detector through the CMU has been done and implemented in a subroutine called CMWINT.[53] This program uses the cross sections from the Particle Data Group (PDG) to obtain the shape of the nuclear interaction lengths in CDF as a function of the particle energy. In this case, we expect to only receive significant punch through backgrounds from kaons and pions. The subroutine output is normalized at high energy to the particle cross sections measured in Caroll, et al.,[54, 55] and returns the number of nuclear interaction lengths traversed by a particle at normal incidence to the calorimeter. This code was modified to account for the upgrades that have taken place since the 88-89 run. The modification includes the additional steel in the CMP and was done by scaling the interaction lengths at 100 GeV/c by the values indicated in PDG for an additional 60 cm of steel. The energy lost by a minimum ionizing particle in the detector material can also have an effect by slowing the particle down and changing the probability with which it interacts. This effect was also included in the punch through probability calculation.

Using Fig. 5-11 as a starting point, the events were weighted by the probability that each would punch through the detector to produce a fake CMP muon. This was done according to the formula:

$$P(\lambda) = exp(-\frac{\lambda}{\sin\theta}) \tag{5-2}$$

where $\lambda(E)$ represents the number of interaction lengths for a particle of energy E at normal incidence and θ is the angle of the track with respect to the calorimeter along the beam-line. The angle of the track with respect to the muon upgrade walls in the $r-\phi$ projection is not taken into account. All tracks are assumed to punch through the CMP at normal incidence in the $r-\phi$ projection.

It is assumed that all particles mimicking muons will reconstruct regardless of the offline CMP reconstruction efficiency. The resulting weighted distributions are shown in Figure 5-12. In the upper histogram, it is assumed all the tracks in Figure 5-11 are pions. The lower two histograms show what happens when all the observed tracks are assumed to be kaons. The interaction probability per unit material is smaller for the positive kaon and this causes the positive kaons to be approximately ten times more likely to punch through the CMU and CMP over negative kaons or pions.

Adding up the weighted events in the B_C signal region yields 1.77 ± 0.08 events if one assumes all of the tracks are kaons and 0.23 ± 0.01 events for the pion assumption. The uncertainties quoted here are statistical. It is clear that assuming all of the tracks come from kaons is incorrect; however, it is not clear what fraction should be applied. Nearly all of the tracks in the misidentified $J/\psi{+}K$ peak are kaons. The background below an invariant mass of 5.1 GeV/c^2 consists of J/ψ+track from other B meson decays. Consequently, production of strange quarks is preferred causing an abundance of kaons over normal $J/\psi+X$ background. This analysis assumes that all of the punch through candidates are kaons. Furthermore, to determine whether the calculation is correct and understand the systematic uncertainties, we shall focus on the region of the $J/\psi + K$ excess where the particle type is well understood. This region is from 5.15 to 5.30 GeV/c^2, which is below the true B meson mass because the third track has been assigned a muon mass here.

c. Systematic Errors.

There are two dominant sources of uncertainty in this calculation. The first involves the lack of knowledge of the interaction cross sections of the punch through candidates with the materials in the detector. The second is uncertainty in the kind and amount of matter encountered by a particle as it traverses the calorimeter. A cross-check can be done to determine the overall systematic error in the calculation of the punch through probability by examining the predictions for the invariant mass region around the $J/\psi + K$ mass peak and comparing these to the data.

The code that allows one to predict the number of punch through fakes in the signal sample will also predict how many tracks would punch through to the CMU alone. Without requiring the added steel in the CMP one would expect most of the positively charged events in the B^+ region to be punch through events. Duplicating the procedure outlined above for the tracks in the $B \rightarrow J/\psi{+}K$ region in Figure 5-11 we require only the acceptance and material through the CMU. The following predictions for the mass region from 5.15 to 5.30 GeV/c^2 are obtained:

- 3.32 ± 0.46 positive events.
- 0.65 ± 0.08 negative events.

Figure 5-13 shows the numbers and event distributions for kaons from the calculation of the punch through probability. This was applied to the initial number of tracks pointing toward the CMU. The data from Run 1b, requiring at least a CMU muon for the third track, are shown in Figure 5-14. The data yield 3.0 $J/\psi + K^+$ events and 1.0 $J/\psi + K^-$ events in the $B^\pm$ mass region.

One problem with this comparison is that the CMU data in the $J/\psi + K$ region, though enriched in punch through, will also contain possible backgrounds. For example, the kaon can decay into a muon and if the tracking chamber picks up the kaon track instead of the muon, then the decay would still reconstruct in the $J/\psi + K$ region. This is also near the most likely location for actual B_C signal events to appear in the distribution. To get some idea of how much of the data in the $J/\psi + K$ mass region is background, we can look in the same mass region but require a CMP muon as well. We obtain 2 positive events and that same negative event having CMU/CMP stubs which pass the cuts. It is approximately 10 times less likely that a K^- would punch through the CMP than a K^+. Consequently, there is an indication that approximately one event of background exists in the CMU data in the B^+ mass region based on the fact that one event is present in the B^- region.

The systematic error is set as the difference between the predicted number of events between 5.15 and 5.3 GeV/c^2 for the positive tracks versus the actual punch through from CMU data of 2 events, or ±39%. The final numbers for the punch through background in the mass region from 4.0 to 6.0 GeV/c^2 is obtained by assuming that all of the events are kaons. The whole exercise is then repeated for Run 1a. The results of this estimate are summarized in Table 5-3

We believe that this is a conservative estimate. We have shown using a known sample of kaons that the calculation properly predicts their numbers

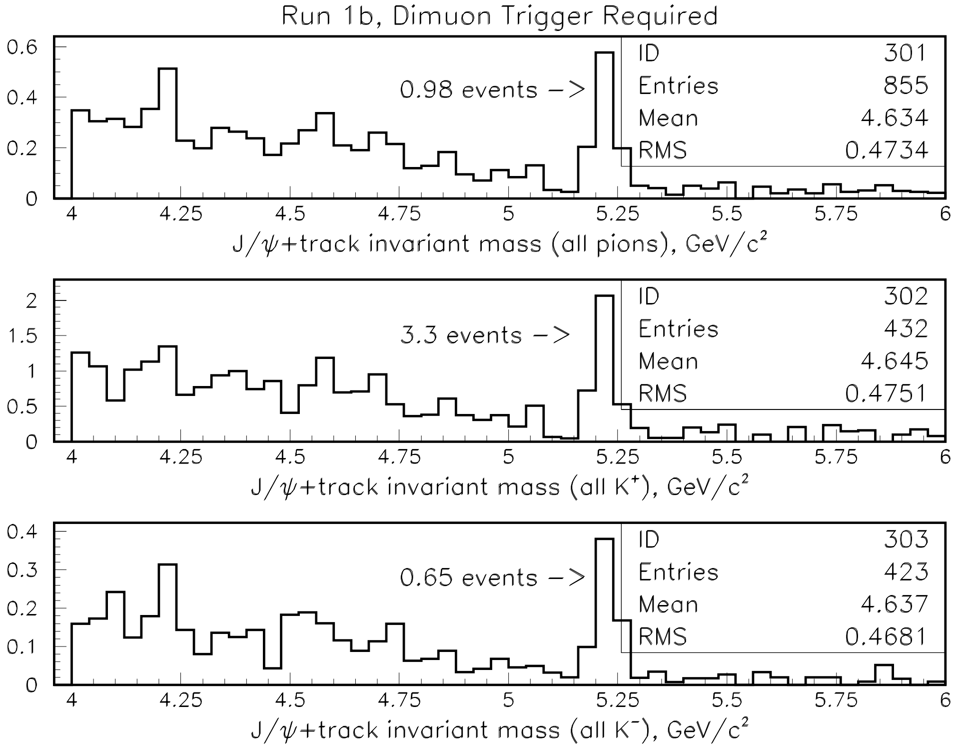

Figure 5-13. These figures show the punch through calculation but only the material through the CMU was required of the third track. The upper plot shows the assumption of only pions. The next two plots show the calculation for positive and negative kaons, respectively. Indicated on the plots are the estimated punch throughs in the $J/\psi + K$ peak region.

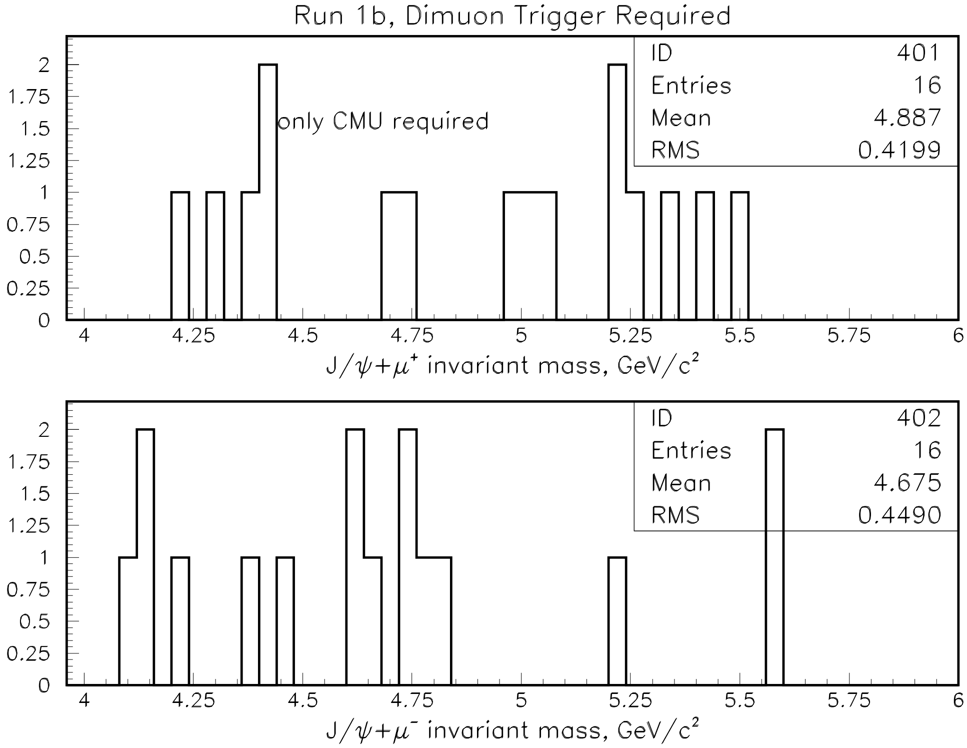

Figure 5-14. This figure shows the data where all of the analysis cuts have been applied but only a CMU muon was required of the third track. The upper plot shown the cases with positive third CMU's and the lower plot is the negative CMU tracks. The $J/\psi + K$ mass region is from 5.15 to 5.30 GeV/c^2.

Table 5-3. Summary of the punch through background for Run 1a and Run 1b. The errors shown in the table are the sum of the statistical and systematic errors in quadrature.

$c\tau^*$ cut	Run 1a	Run 1b	Run 1a + Run 1b
60μm	0.43±0.17	1.77±0.69	2.20±0.71
85μm	0.38±0.17	1.56±0.62	1.94±0.64
100μm	0.34±0.14	1.50±0.56	1.84±0.58

within statistics given the total number of input tracks. Furthermore we have assumed that all of the tracks are kaons for the purposes of calculating the punch through background. Since the positive kaon has a much better chance of faking a muon, this is the worst case scenario.

We can support the conclusion that our estimate of all kaons is conservative by again turning to the CMU-only sample and looking at the charge asymmetry in the data in the mass region of interest. The point is that if the background in the entire mass region is dominated by kaon punch through, there would be a large asymmetry in the CMU only data. As pointed out earlier, there are 3 positive events and one negative event in the $J/\psi + K$ mass region, indicating some excess expected of positive over negative events. However, the CMU data have 16 positive events and 16 negative events from 4.0 to 6.0 GeV/c^2 as shown in Figure 5-14. The pion punch through probability is the same as the K^- punch through probability, so it is unlikely that the lack of charge asymmetry is due to an excess of symmetric pion punch through. This evidence in the data supports our conclusion that the estimate of the punch through background is a conservative one.

3. Decay in Flight Background from Prompt Pions and Kaons

a. Introduction.

Pion or kaon decay in flight (DIF) can contribute to the background associated with the $B_c \to J/\psi + \mu + X$ search. This happens when a daughter muon from a prompt pion or a prompt kaon in an event makes a good vertex with a J/ψ in the event and passes all the analysis cuts.

In the search for B_c, one of the cuts required that the P_t of the muon from the B_c be greater than 3 GeV/c. With this cut on the P_t, the probability for a pion or a kaon to decay before reaching the muon chambers is small. However there are a large number of pions and kaons present in an event, hence decays in flight will contribute to the total background. In this sub-section we describe the method to determine the DIF background due to the pions or kaons from the primary vertex that decay in flight and make a good vertex with a J/ψ in the event.

b. Estimate of the Background.

This estimate was made using data. CTC tracks with $P_t > 2$ GeV/c^2 in a data event with a J/ψ were selected. These tracks were assumed to be pions or kaons. They were forced to decay before the end of the CMU volume. This was done by simulating the tracks through the detector using CDFSIM [56] forcing them to decay before reaching the CMU chambers. CDFSIM is a comprehensive detector simulation package at CDF. Unlike QFL, it derives the detector effect from first principles. Hadronic interaction was enabled in CDFSIM so that the probability of the particle to interact with the material in the detector before it decayed was taken into consideration. The decayed tracks were reconstructed using the offline reconstruction program and were dropped back into the event from which they were selected. These tracks were then fitted to a vertex with the two muons from the J/ψ in the event. The resulting three track combinations were subjected to all the other analysis cuts. Combinations that passed the cuts were weighted by the probability for the third track to decay before the end of the CMU volume. The weight was calculated using the following formula

$$\begin{aligned}\text{Weight}(\pi) &= 1 - e^{-(L_{cmu}\times M_{\pi}\times c)/(p_t\times c\tau_{\pi})} &\quad (5\text{-}3)\\ \text{Weight}(K) &= 1 - e^{-(L_{cmu}\times M_{K}\times c)/(p_t\times c\tau_{K})} &\quad (5\text{-}4)\end{aligned}$$

where, L_{cmu} is the distance between the primary vertex and the CMU chambers in cm, M_{π} and M_K are the pion and the kaon mass in GeV/c^2, $c\tau_{\pi}$ and $c\tau_K$ are the decay length for the pion and the kaons in cm and c is the speed of light in cm-s^{-1}. The background was calculated by summing up the weights of all the three track combinations whose invariant mass fell between 4 and 6 GeV/c^2.

The CTC tracks selected were required to have a $P_t > 2$ GeV/c and not 3 GeV/c as in the normal analysis cut for this search. This is done because when a track decays, it develops a kink. The kink is larger for the kaons than for the pions. Because of the kink the reconstruction program reconstructs these tracks, with a momentum that is some times higher than the actual momentum of the track. Thus it is possible for a track with $P_t < 3$ GeV/c to pass the 3 GeV/c P_t cut, if it is reconstructed after it decays within the CTC. This effect is shown in Fig. 5-15. The solid lines in these plots are the P_t of the track before the decay and the dashed ones are the P_t of the track after the decay and the reconstruction. In the top plot all the tracks were assumed to be kaons and in the bottom they were assumed to be pions. It should be noted that more tracks reconstruct as stiffer tracks after the decay if they are assumed to be kaons as compared to the assumption that they are pions. This is because the muons from a kaon decay have a greater kink than the muons from a pion decay. This "feedup" in the momentum motivated the requirement that the P_t cut on the selected tracks be much below 3 GeV/c. However in this estimate this cut is set at 2 GeV/c and not lower. This is done because the third muon is required to be a CMU/CMP muon. A track with a $P_t < 2$ GeV/c would decay into muons with $P_t < 2$ GeV/c. Due to the dE/dx losses a muon with $P_t < 2$ GeV/c will not be able to traverse as far as the CMP. Hence, even though a 1 GeV/c track may decay and reconstruct as a track with $P_t > 3$ GeV/c, the actual momentum of the daughter muon would be less than 1 GeV/c. A muon with this P_t would be unable to reach the CMP and therefore such an event will be rejected.

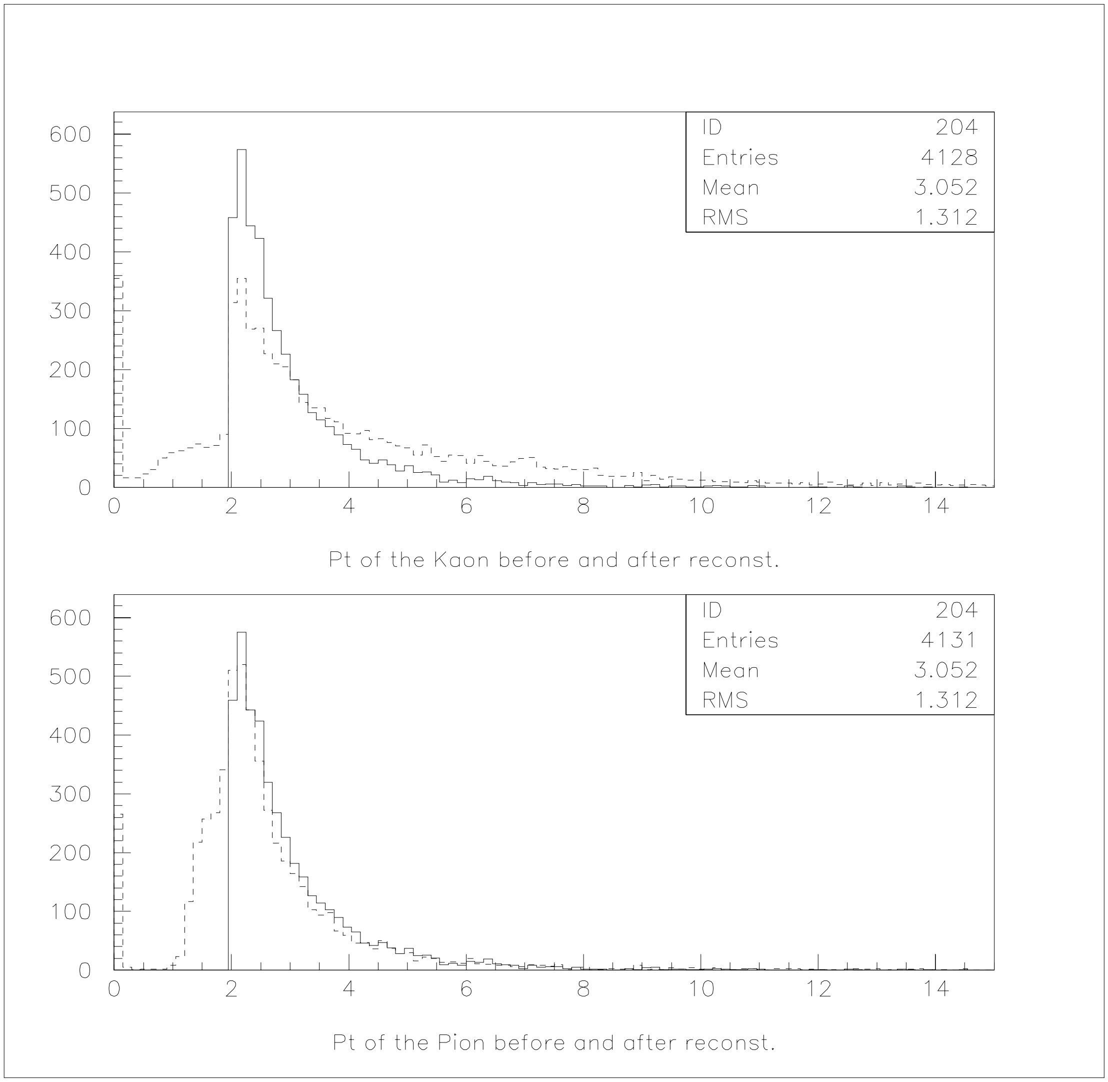

Figure 5-15. The top plot shows the momentum spectrum of the kaon before decay (solid line) and after decay and reconstruction (dashed line); the bottom plot shows the same for the pions.

Figure 5-16 shows the result of the estimate for this background for about one third of the run 1b data set. The top plot in this figure shows the three track invariant mass distribution when all the tracks are assumed to be pions. The lower plot shows the same thing when the tracks are assumed to be kaons. It should be noted that the number of kaon events are less than the number of the pions events. This is because the reconstruction efficiency for a decayed pion is greater than the reconstruction efficiency for a decayed kaon. In both these cases one of the most discriminating factors against this background is the requirement that the third track be a SVX track. After weighting the entries in the two plots in Fig. 5-16 and summing them up for the signal region we get .21 events for the pions and .17 events for the kaons. Since the kaons and the pions in this case are prompts, we used the kaon to pion ratio as 4:1 [57] where Ref. [57] gives the prompt kaon to pion ratio in $p\bar{p}$ collisions at $\sqrt{s}=$ 1.8 TeV. Assuming the pion to kaon ratio as 4:1, and using the fact that we looked at about one third of the run 1b data, we can calculate the number of background events for Run 1b. This result is scaled to Run 1a, by scaling the Run 1b results by the number of J/ψ's in Run 1a. The results of this calculation are summarized in Table 5-4.

c. Systematic Error. One of the major contribution to the systematic error in the calculation of the background from the decays in flight comes from the efficiency of reconstructing a track that decayed after entering and before exiting the CTC. This is due to the fact that most of the tracks that decay after exiting the CTC will be reconstructed by the CTC and will pass as good tracks. However when a track decays within the CTC, depending on how far into the CTC it actually decay, the track might or might not get reconstructed as a good track. Figure 5-18 shows that about 17% of the reconstructed tracks decayed within the inner 80% of the CTC. We therefore make a conservative estimate on the systematics due to the reconstruction as 17%. The systematic error due to the uncertainty in the K to π ratio was 25%. Therefore the total systematic error for this case was 30 %.

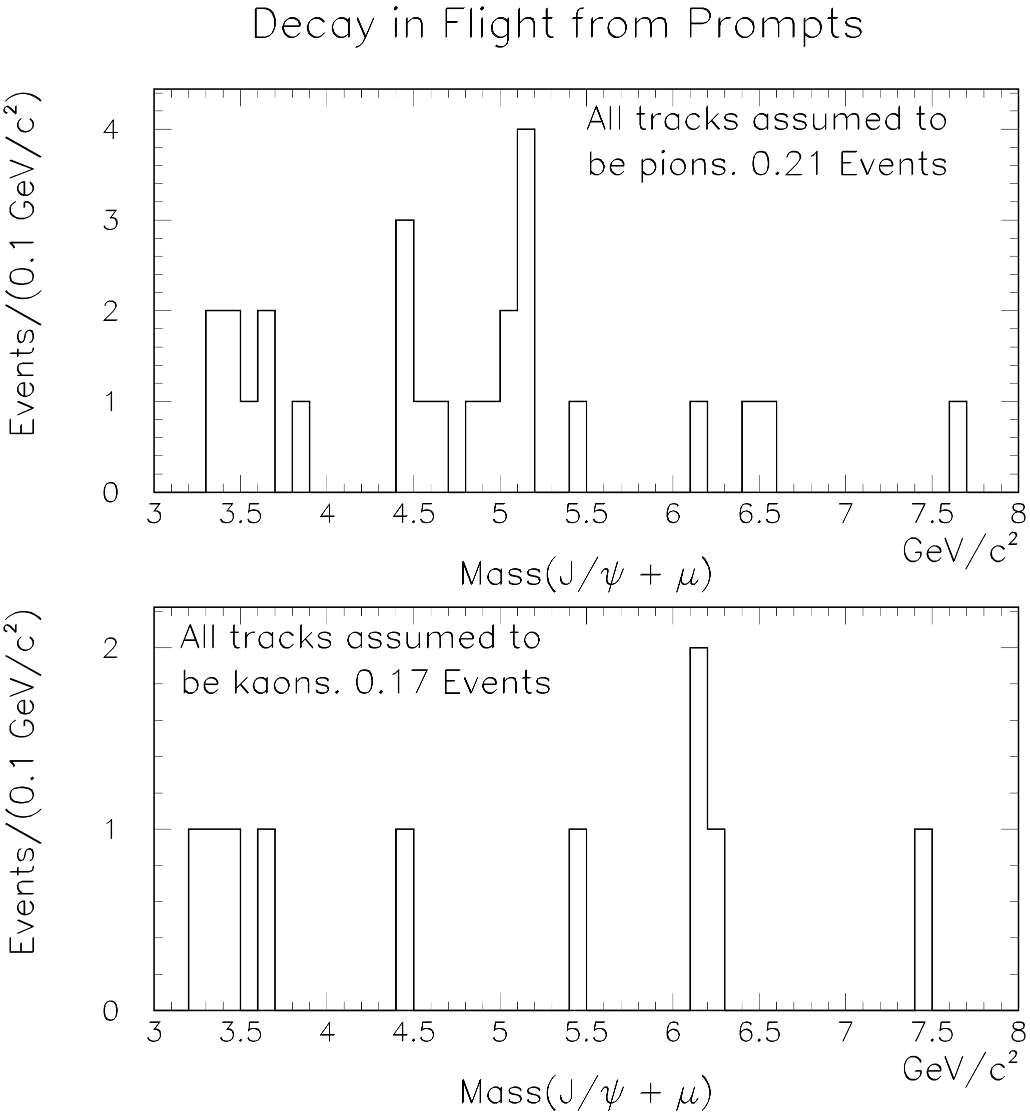

Figure 5-16. The top plot shows the three track invariant mass distribution when the third track is assumed to be a pion. The bottom plot shows the same thing when the third track is assumed to be a kaon. These plots are for about one third of the Run 1b. After weighting the probability of the third track to decay and summing it up for all the entries in the signal region, there will be .21 events when the tracks were assumed to be pions and 0.17 events when the tracks were assumed to be kaons.

Table 5-4. Summary of the decay in flight background from prompts for Run 1a and Run 1b. The errors shown in the table are the sum of the statistical and systematic errors in quadrature.

$c\tau^*$ cut	Run 1a	Run 1b	Run 1a + Run 1b
60μm	0.14 ± 0.10	0.64 ± 0.49	0.78 ± 0.50
85μm	0.13 ± 0.10	0.61 ± 0.46	0.74 ± 0.47
100μm	0.10 ± 0.08	0.58 ± 0.37	0.68 ± 0.38

4. Background from Decay in Flight of Pions or Kaons from Displaced B's

a. Introduction.

B's which decay into $J/\psi+X$ may also contribute to the DIF background. The pions and the kaons from the inclusive B decay might decay in flight into a muon. This muon could make a good vertex with the J/ψ from the B. If such a combination passes all the other analysis cuts then it would show up as a background to the B_c search. The most likely scenario for this is when the particle decays towards the end of the CTC or decays in the calorimeters before it could shower. In these cases it is likely that the CTC will reconstruct the original particle, yet the muon from the decay will yield a stub in the muon chambers. This stub could be assigned to the reconstructed track.

b. Estimate of the Background.

This background was estimated using Monte Carlo. BGENERATOR was used to generate the B's. The generated B's were decayed using CLEOMC Monte Carlo. All the B's were forced to decay into $J/\psi+X$. CDFSIM was used to simulate the detector. The detector simulation was done twice. In the first case the pions and the kaons in the event were forced to decay before the end of the CMU volume with the hadronic interaction enabled in the simulation. In the other case the pions and the kaons were not forced to decay, but were allowed to decay naturally.

The analysis code was run on the two data sets generated above. In the case where the particles were not forced to decay all the analysis cuts were applied, however the requirement that the third track have a CMU/CMP stub was replaced by the requirement that it point to the CMU/CMP fiducial region. The top plot in Fig. 5-17 shows the three track invariant mass distribution, where the third track is assigned the muon mass. In this case the decays were not forced. There are 310 entries in this plot in the signal region, with 58 events under the $J/\psi K$ peak where the K track has been assigned the muon mass. A similar plot for the run 1b data yields about 520 events in the signal region and 74 events under the $J/\psi K$ peak (see Fig. 5-11). We use the number of events under the $J/\psi K$ peak to scale the Monte Carlo results to the Run 1b data. From these numbers we get the scale factor as 1.27. The bottom plot in Fig. 5-17 shows the three track invariant mass distribution for the case where the kaons and the pions were forced to decay. In this plot all the analysis cuts were applied, including the requirement that the third tracks have CMU/CMP stubs. 103 events were picked up in the signal region. To get the number of background events from this plot, the entries in the plot were weighted by the probability of their third track to decay before the end of the CMU volume. If all the tracks in the plot were assumed to be pions then the the number of the background events was 1.17 events. If the tracks were assumed to be kaons the number of the background events was 8.15 events. To estimate the background from Fig. 5-17 we will have to determine the K to π ratio for the third tracks in the bottom plot in Fig. 5-17. It should be noted that in this case we cannot use the kaon to pion ratio we used in the prompt case. The ratio for this case is determined as follows:

We took a sample of the $B \to J/\psi + X$ Monte Carlo data which had passed the trigger simulation. In this data set we counted the number of K's and π's with $P_t > 3.0$ GeV/c using the information from the GENP bank. The K to π ratio obtained by such a counting gave us the ratio which would exist before any

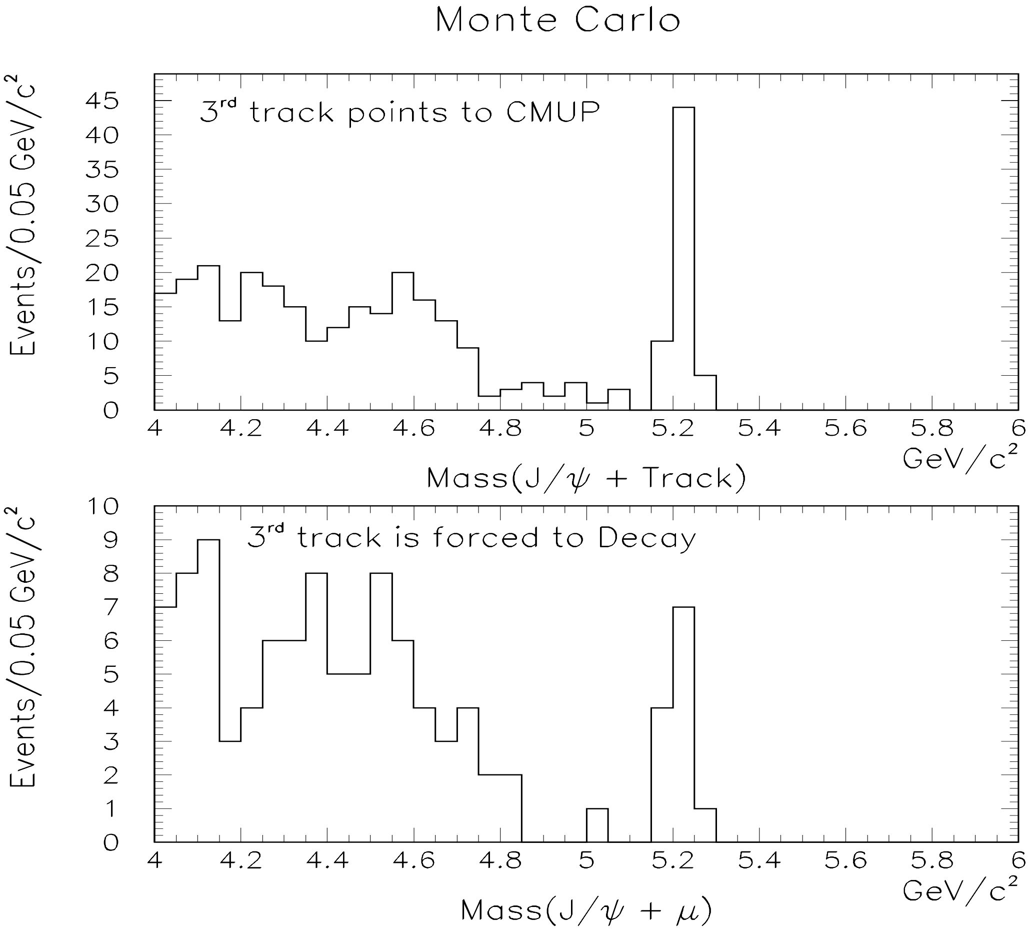

Figure 5-17. The top plot shows the three track invariant mass distribution for the $B \to J/\psi + X$ Monte Carlo data set, where the kaons and the pions were not forced to decay. All the analysis cuts were applied; however, the third track was not required to have a CMU/CMP stub but was just required to point to the CMU/CMP fiducial region. The lower plot is made from the same data set when the pions and the kaons were forced to decay before the end of the CMU volume. If the entries in this plot are weighted by the probability of their third track to decay, then they add up to 1.17 events if the tracks are assumed to be pions and 8.15 events if the tracks are assumed to be kaons.

reconstruction was done. We call this ratio the ratio at birth. For our sample N_{kaon}/N_{pion} at birth was 1.38 .

Next we studied how the ratio at birth will be affected when the reconstruction is done. We generated one dataset with $B \to J/\psi K$ and another dataset with $B \to J/\psi\pi$. The number of events generated in the two datasets was the same. The kaons and the pions in each data set were forced to decay within any region up to the CMU and the events were simulated through the detector using CDFSIM. Our analysis code was run on the simulated data. After applying all the analysis cuts we got 238 events for the $J/\psi K$ case and 891 events for the $J/\psi\pi$ case, see Fig. 5-18. This means that if we start with a sample in which K to π ratio is 1:1 at birth, then after reconstruction N_{kaon}/N_{pion} becomes 0.27 . In our case N_{kaon}/N_{pion} at birth was 1.38, hence after the reconstruction N_{kaon}/N_{pion} will be 0.37 . This implies that the bottom plot in Fig. 5-17 has 27% kaons and 73% pions.

To get the estimate of this background for run 1b, the results were scaled by a factor of 1.27. From Monte Carlo we have already seen that the sample of the third tracks have 27% kaons and 73% pions. Using this ratio and the scale factor we obtain the number of background events for Run 1b. The result was scaled to Run 1a by the number of events in the similar $J/\psi K$ peak in Run 1a. The results of this estimate are summarized in Table 5-5.

Table 5-5. Summary of the decay in flight background from B's for Run 1a and Run 1b. The errors shown in the table are the sum of the statistical and systematic errors in quadrature.

$c\tau^*$ cut	Run 1a	Run 1b	Run 1a + Run 1b
60μm	0.79±0.23	3.87±1.12	4.66±1.14
85μm	0.79±0.23	3.74±1.08	4.53±1.10
100μm	0.79±0.23	3.53±1.02	4.32±1.05

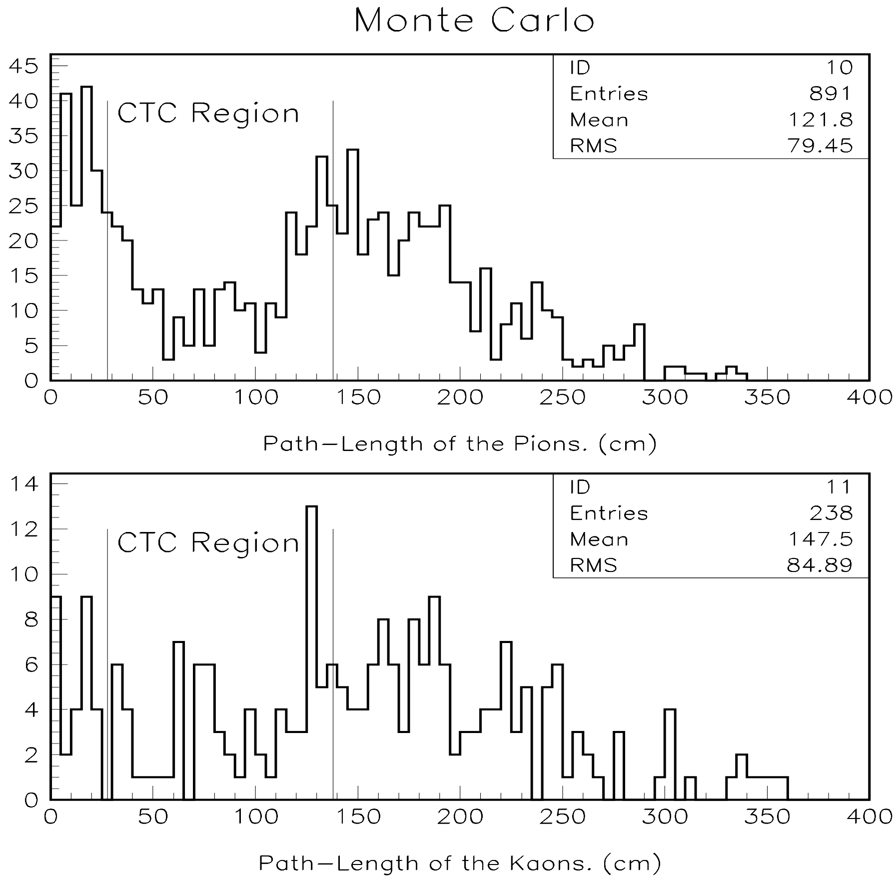

Figure 5-18. The top plot shows the path-length of the pions for a MC sample of $B \to J/\psi + \pi$ events, where the pions were forced to decay within any region up to the CMU. The sample has all the analysis cuts applied on it. The bottom plot shows the path-length distribution of the kaons for a MC sample of $B \to J/\psi + K$; the kaons were forced to decay within any region up to the CMU. This sample, too, has all the analysis cuts applied to it.

c. Systematic Errors.

The systematic error due to the uncertainty in the reconstruction is the same as for the DIF from the prompt pion and kaon background, which was 17%. The contribution from the trigger simulation is 4%. There is an 8% systematic error on the K to π ratio. The systematic error due to the Monte Carlo statistics is 17%. Thus the total systematic error is 24%.

5. Cross Checks of the Background Estimates

The search for the $B_c \to J/\psi + \mu + X$ depends on the accuracy with which we can estimate the background. It was therefore very important to cross-check the background estimates. The biggest contribution to the background in this search was due to the fake muons. The fake muon background estimates reported above were cross checked by using independent data sets. The checks confirmed the accuracy of the background due to fake muons. The details of the check are described in Appendix 1.

6. Summary of the Total Background

The total background to the search for Run 1a and Run 1b is summed up in Tables 5-6, 5-7 and 5-8:

E. Efficiencies

To determine the efficiencies, B_c's were generated using BGENERATOR and were simulated through the detector using QFL. The trigger was simulated using DIMUTG. The efficiency for the B_c was defined as follows:

$$\varepsilon_{B_c} = \frac{Number\ of\ B_c\ picked\ up\ by\ the\ analysis\ code}{Number\ of\ events\ passing\ the\ dimuon\ trigger}$$

In this analysis we used the relative efficiencies instead of absolute efficiencies. The relative efficiency was calculated with respect to the B_u, where

Table 5-6. Background for Run 1a and Run 1b at $c\tau > 60\mu$m.

Background type	Run 1a	Run 1b	Run 1a + Run 1b
$B\bar{B}$	0.23±0.16	1.07±0.62	1.30±0.64
Punch through	0.43±0.17	1.77±0.69	2.20±0.71
Decay in flight from prompts	0.14±0.10	0.64±0.49	0.78±0.50
Decay in flight from B's	0.79±0.23	3.87±1.12	4.66±1.14
Total Background	1.59±0.34	7.53±1.53	8.94±1.57
Data events	3	14	17

the efficiency of the B_u is defined in the same manner as that for the B_c. The relative efficiency can be written as follows:

$$\varepsilon_{rel} = \frac{\varepsilon_{B_c}}{\varepsilon_{B_u}}$$

For the purpose of this calculation the B_c were generated at various assumed lifetimes of .25, .50, .75, 1.0, 1.2 and 1.55 ps. The B_u was generated at 1.55 ps [20]. The results of the the relative efficiency calculations are shown in Table 5-9.

The systematic error for this calculation is listed in Table 5-10. The individual sources of the systematic errors in Table 5-10 are described as follows:

- There is a 2.5% error due the finite statistics of the Monte Carlo used.
- The calculation of the error due to the b quark production spectrum was calculated by the $J/\psi e$ analysis [58]. Since this result would be the same for both the analyses, we used the number obtained by that group.
- The uncertainty due to the Peterson's fragmentation parameter is only for the B_u's. We used the number obtained by the $J/\psi\pi$ analysis [26].
- The difference in Run 1a and Run 1b accounts for a 3.4% uncertainty. We therefore assign a 3.4% error to the detector simulation.

Table 5-7. Background for Run 1a and Run 1b at $c\tau > 85\mu$m.

Background type	Run 1a	Run 1b	Run 1a + Run 1b
$B\bar{B}$	0.23±0.16	1.07±0.62	1.30±0.64
Punch through	0.38±0.17	1.56±0.62	1.94±0.64
Decay in flight from prompts	0.13±0.10	0.61±0.46	0.74±0.47
Decay in flight from B's	0.79±0.23	3.74±1.08	4.53±1.10
Total Background	1.53±0.34	6.98±1.46	8.51±1.50
Data events	3	11	14

- The error due to the trigger simulation was estimated to be 4%.

Upon adding all these errors in quadrature we get the total systematic error as 8% for our relative efficiency calculations.

Table 5-8. Background for Run 1a and Run 1b at $c\tau > 100\mu$m.

Background type	Run 1a	Run 1b	Run 1a + Run 1b
$B\bar{B}$	0.23±0.16	0.71±0.51	0.94±0.53
Punch through	0.34±0.14	1.50±0.56	1.84±0.58
Decay in flight from prompts	0.10±0.08	0.58±0.37	0.68±0.38
Decay in flight from B's	0.79±0.23	3.53±1.02	4.32±.1.05
Total background	1.46±0.32	6.32±1.32	7.78±1.36
Data events	2	11	13

Table 5-9. Relative efficiency calculations

B_c Lifetime (ps)	cτ^* cut (μm)	$1/\varepsilon_{rel} = \frac{\varepsilon_{B_u}}{\varepsilon_{B_c}}$ (Errors are Stat + Sys.)
0.25	60	3.11±.36
0.50	60	1.96±.19
0.75	85	2.30±.23
1.00	85	1.90±.23
1.20	100	1.82±.18
1.55	100	1.59±.14

Table 5-10. Systematic errors for the efficiency calculations

Source of Error	Contribution
Monte Carlo Statistics	2.5%
Production Spectrum	5.0%
Fragmentation Parameter	2.3%
Detector Simulation	3.4%
Trigger Simulation	4.0%
Total	**8.0%**

CHAPTER 6.

Conclusions

We searched for the B_c meson in the $J/\psi + \mu + X$ decay mode in approximately 110 pb^{-1} of data collected with the CDF detector. The search yielded 17 B_c candidate events with an expected background of 8.9 events. The probability for this background to fluctuate to the observed number of events is 1.04%. This is too large to experimentally confirm the B_c. However there is definitely an excess of the observed events in data over the expected background and this may be attributed to the production of B_c. Another independent search for the $B_c \rightarrow J/\psi + e + X$ was also performed at CDF. In this search 16 candidate events were observed in data with an expected background of 9.60 events. A natural step will be to combine the results from the two searches to establish the existence of the B_c meson. The individual and the combined results of the two searches are shown in Table 6-1. When the two results are combined we observe 33 B_c candidate events in data with an expected background of 18.5 events. This corresponds to a probability of .23% for the background to fluctuate to the observed number of events. If we assume a Gaussian distribution for the signal events then this probability would correspond to a 3.01 sigma effect. The combined results strongly point to the evidence for the B_c production at the Tevatron.

A. Limit on the Relative B_c Production

The results from the search for the $B_c \rightarrow J/\psi+\mu+X$ alone is not sufficiently significant to enable us to claim the observation of the B_c meson. Hence, we calculated the limit on the B_c production. This was calculated as a 95% C.L.

Table 6-1. This table shows the number of events that were observed in the data for the $B_c \to J/\psi\mu X$ and $B_c \to J/\psi e X$ searches. It also shows the probability for the background to fluctuate to the observed events for the individual and the combined analyses.

Search Mode	Events Observed	Background	Probability	Sigma
$B_c \to J/\psi\mu X$	17	8.94	1.04%	2.56
$B_c \to J/\psi e X$	16	9.60	3.62%	2.09
Combined	33	18.54	0.21%	3.07

limit on the production of $B_c \to J/\psi + \mu + X$ relative to the $B_u \to J/\psi + K$ production. The limit is calculated as follows;

$$\frac{\sigma.\mathrm{BR}(B_c^+ \to J/\psi + \mu^+ X)}{\sigma.\mathrm{BR}(B_u^+ \to J/\psi + K)} = \frac{N_{J/\psi+\mu+X}}{N_{J/\psi+K}} \times \varepsilon_{rel} \tag{6-1}$$

ε_{rel} is the relative efficiency for finding $B_c^+ \to J/\psi + \mu^+ X$ compared to $B_u^+ \to J/\psi + K$. It was calculated from Monte Carlo and is listed in Table 5-9. $N_{J/\psi+\mu+X}$ and $N_{J/\psi+K}$ are the number of $B_c \to J/\psi + \mu + X$ and $B \to J/\psi + K$ candidate events seen in the data.

The formula used to calculate the 95% C.L is obtained from Ref. [59, 60]. It includes all the errors in the limit calculations and can be written as;

$$\epsilon = \frac{\sum_{n=0}^{N_{tot}} \int G(b)G(\varepsilon_{rel})G(N_{J/\psi+K})P(n, \frac{r.N_{J/\psi+K}}{\varepsilon_{rel}})db\, d\varepsilon_{rel}\, dN_{J/\psi+K}}{\sum_{n_b=0}^{N_{tot}} \int G(b)P(n_b, b)db} \tag{6-2}$$

where r is the relative B_c production rate, N_{tot} is the number of events in the signal region, b is expected background, G is the Gaussian probability distribution, P is the Poisson probability distribution and $\epsilon = 1$ - C.L.. The results of the 95% C.L. upper limit on the $(\sigma.\mathrm{BR}(B_c^+ \to J/\psi + \mu^+ X))/(\sigma.\mathrm{BR}(B_u^+ \to J/\psi + K))$ as a function of assumed B_c lifetime is shown in Table 6-2 and is plotted in Fig. 6-1. The dashed curve in the plot shows the theoretical prediction for the same ratio.

Table 6-2. This table shows the 95% C.L. limit on the production of $\psi\mu + X$ from B_c to ψK from B_u.

Results at various assumed B_c lifetimes

N(ψK) = 80 ± 9

B_u lifetime = 1.55 ps.

B_c lifetime(ps)	cτ^* cut μm	$1/\varepsilon_{rel}$ (stat+sys)	$N_{\psi\mu X}$	N_{bkg} (stat+sys)	$\frac{\sigma.BR(B_c^+)}{\sigma.BR(B_u^+)}$ 95% C.L.
0.25	60	3.11 ± .36	17	8.94 ± 1.57	0.71
0.50	60	1.96 ± .19	17	8.94 ± 1.57	0.44
0.75	85	2.30 ± .23	14	8.51 ± 1.50	0.42
1.00	85	1.90 ± .23	14	8.51 ± 1.50	0.35
1.20	100	1.82 ± .18	13	7.68 ± 1.36	0.32
1.55	100	1.59 ± .14	13	7.68 ± 1.36	0.28

The theoretical prediction for the ratio σ.BR($B_c^+ \to J/\psi + \mu^+ X$) to ($\sigma$.BR($B_u^+ \to J/\psi + K$) ratio is obtained from the partial width for the decay of the B_c meson. The partial width was estimated using the ISGW model [46] by Lusignoli et. al. in Ref. [25].

$$, (B_c^+ \to J/\psi + \mu^+ + X) = 39 \times 10^{-15}\mathrm{GeV} \tag{6-3}$$

The theoretical prediction also assumes that;

$$\frac{\sigma(b \to B_c)}{\sigma(b \to B_{u,d,s})} = 10^{-3} \tag{6-4}$$

This value was obtained from perturbative QCD calculations done by Masetti et al. in Ref. [29].

B. Conclusion

The 95% upper limit on the $B_c \to J/\psi + \mu + X$ production relative to $B_u \to J/\psi + K$ in Fig. 6-1 shows that the measured limit is consistent with the theoretical prediction of B_c production. However if the excess in the observed events is assumed to be from B_c's then the measured production cross-section is two times the theoretical prediction.

C. Future Prospects

Run II of the Tevatron is expected to collect about one fb^{-1} of data. This increase in the luminosity will enable one to firmly establish the existence of the B_c meson not only using the $B_c \to J/\psi + \ell + X$ channel, but also with the exclusive channel $B_c \to J/\psi + \pi$. The increased statistics will open avenues for lifetime measurements and the exclusive mode could be used to measure the B_c mass. These measurements will be a good test of the theoretical models which predict the B_c properties.

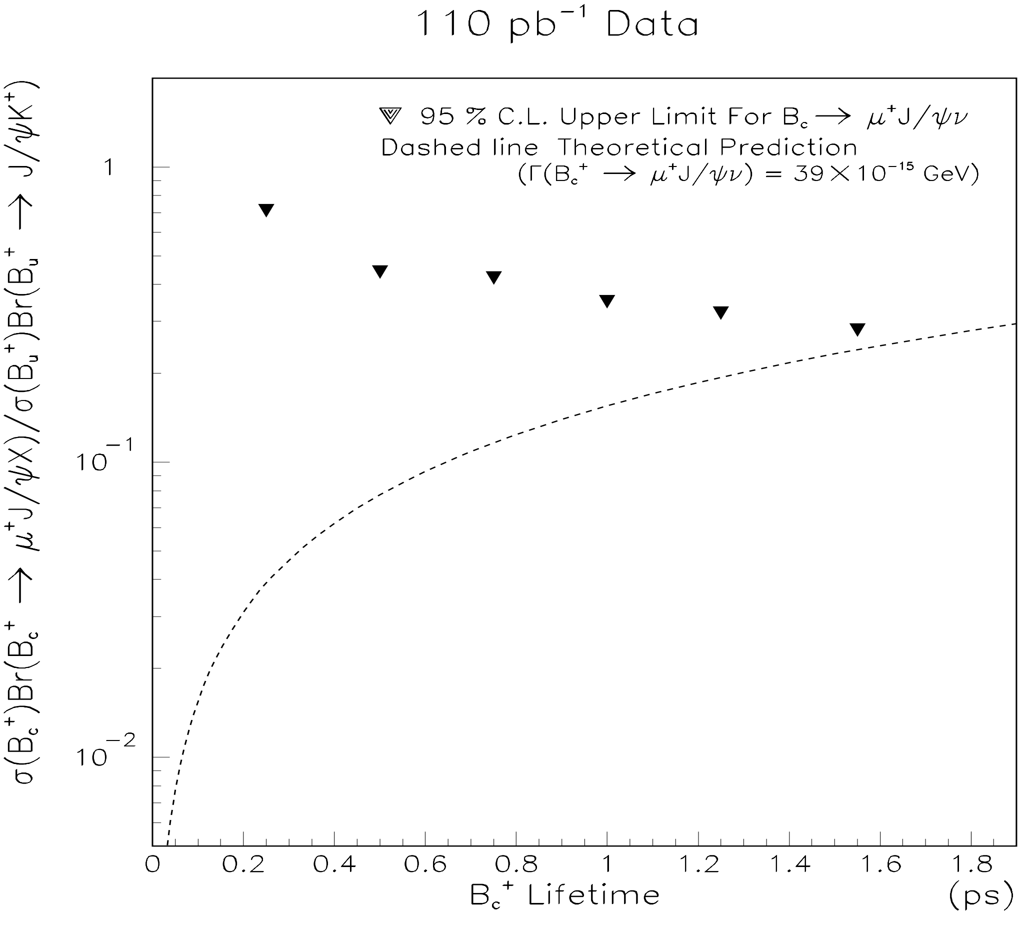

Figure 6-1. 95% C.L. upper limit on the $\sigma \times Br(B_c \to \psi\mu X)/\sigma \times Br(B \to \psi K)$ for the Run 1a and 1b data.

APPENDIX

APPENDIX A.

Checks on the Fake Rates

A. Introduction

We have searched for the B_c meson in the semileptonic mode, $B_c \rightarrow J/\psi \mu X$, where the J/ψ decays into $\mu\mu$. The signature of the B_c in this search was three muons from a displaced vertex. The major background to this search is due to fake muons, therefore an accurate estimate of the muon fake rate is an important issue in this analysis. In this chapter we describe the checks that were performed on the muon fake rate calculations used in the B_c analysis.

B. Check of the Fake Rates

The data used to perform the checks on the muon fake rates comes from the Run 1b inclusive-electron and inclusive-muon triggers. The data sets are described in Ref. [61]. The b purity of these data sets was enhanced by requiring that the jet containing the triggered lepton be tagged by SECVTX [62].

Our aim was to check if we could correctly predict the number of fake muon in the SECVTX-tagged single-lepton data sets. Two daughter leptons from a B decay should have opposite charges because if one lepton came from the semileptonic decay of the B then the other lepton will come from the sequential decay of a charm particle. We paired the triggered lepton in an event with an other lepton in the same event. If the other lepton (henceforth called the tagged lepton) has the same charge as the triggered lepton, it must either be a fake lepton or must come from the other B in the event. The fake rate was checked by counting the number of same-sign pairs of triggered and tagged muons in data. These pairs were required to have a mass less than 5.0 GeV/c^2 to reduce the contribution of tagged muons from the other B in the event ($B\bar{B}$ contribution). The number of such pairs obtained from data was compared with the number of pairs due to the predicted fakes and the $B\bar{B}$.

The cuts applied on the triggered leptons for the single-electron and the single-muon data sets are listed below:

- For electron sample :
  - electron in SVX
  - electron passes single-electron L2 trigger
  - $\mathrm{P}_T > 6.0$ GeV/c
  - $\mathrm{E}_T > 7.5$ GeV
  - $\mathrm{E}_{had}/\mathrm{E}_{EM}$(3 towers) < 0.04
  - LSHR < 0.2
  - Δx of track and CES wire cluster < 1.5 cm
  - Δz of track and CES strip cluster < 3.0 cm
  - strip profile $\chi^2 < 10$
  - wire profile $\chi^2 < 10$
  - electron track is a part of SECVTX tag
- For muon sample :
  - muon in SVX
  - muon passes single-muon L2 trigger
  - $\mathrm{P}_T > 8.0$ GeV/c
  - CMUP type (CMUSTYP = 3)
  - χ^2_x(CMU) < 9
  - χ^2_z(CMU) < 12
  - χ^2_x(CMP) < 9
  - muon track is a part of SECVTX tag

The P_T distributions of the triggered leptons for Monte Carlo and data are shown in Fig. A-1.

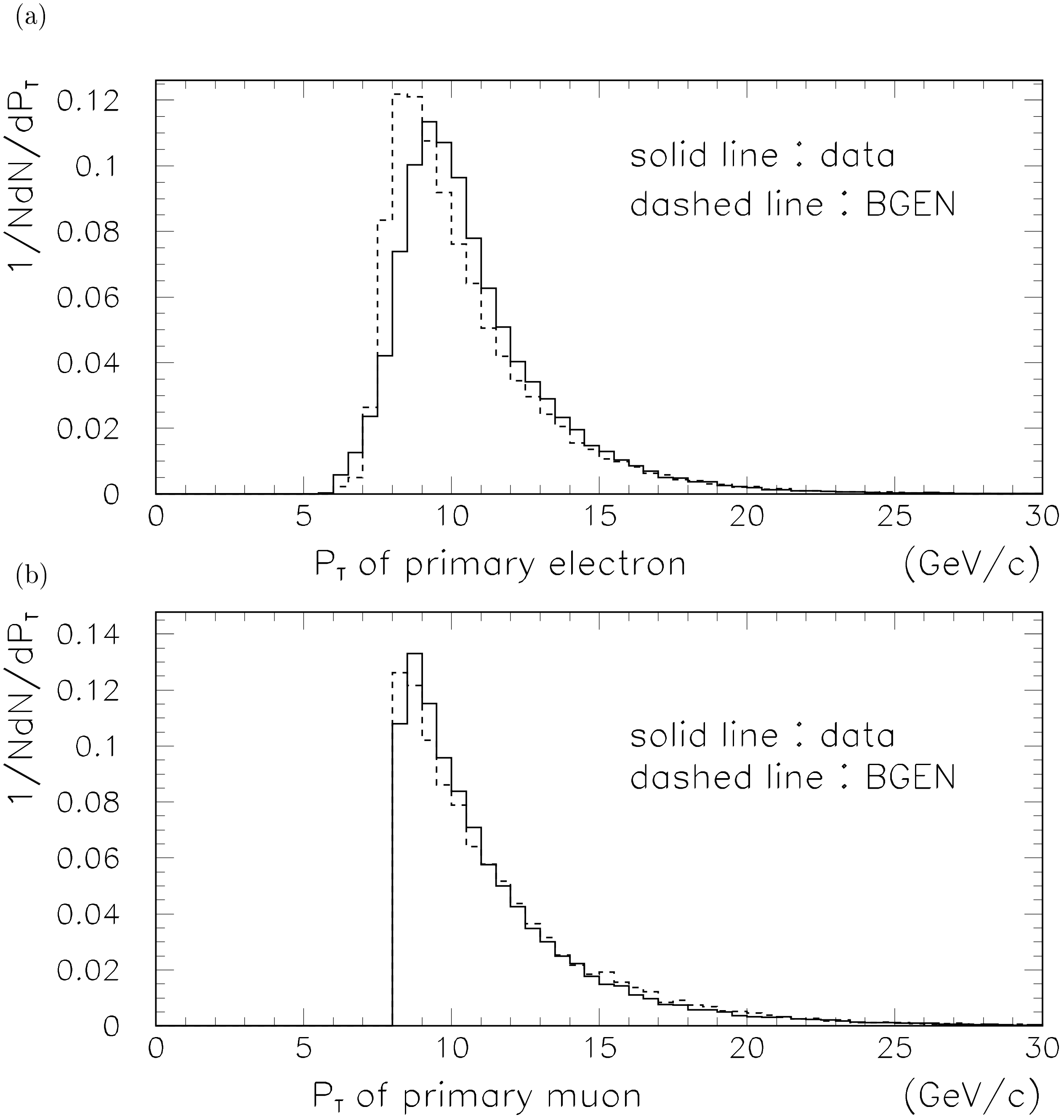

Figure A-1. P$_T$ distribution for the triggered lepton; (a) for SECVTX-tagged single e sample and (b) for SECVTX-tagged single μ sample. The solid line is for data and the dashed line is for BGENERATOR Monte Carlo.

1. Fake Muon Tag Rate

A muon can be mimicked either by hadron punch-through or decay in flight. The background due to the hadron punch-through is obtained by summing the probability of the CTC tracks in the given sample to punch-through to the CMP chambers. This calculation is described in detail in Chapter 5.

The fake rate due to decay in flight (DIF) is estimated by using Monte Carlo. PYTHIA was used to generate $B\bar{B}$ pairs. Data thus generated were passed through a filter. This filter simulated the CFT 7.5 GeV and CFT 12.0 GeV momentum thresh holds on the lepton at the generator level. Events passing this filter were simulated through the detector using CDFSIM. In CDFSIM the kaons and the pions were forced to decay in any region upstream of the CMU chambers. The P_t-dependent rate at which the tracks will fake a muon due to decay in flight is obtained by dividing the number of tracks pointing to the CMUP fiducial region in a particular P_t bin by the weighted sum of CMUP muons observed in the same bin. The weighted sum of the CMUP muons in that bin is obtained by summing the probability of the muons' tracks to decay within the region upstream of the CMU chambers. This weighting is needed because all the tracks were forced to decay in the Monte Carlo simulation. This calculation is described in detail in Chapter 5. Figure A-2a shows the rate at which a track will mimic a muon if it is assumed to be a pion and Figure A-2b shows the rate at which a track will mimic a muon if it is assumed to be a kaon.

2. Mass of the Primary Lepton and the Tagged Muon.

The solid circles in Figure A-3a show the invariant mass of the triggered muon and the tagged muon for data for the same-sign pairs and Fig. A-3b shows the mass distribution for the opposite-sign pairs. The dashed histograms in the two figures show the contribution from the fake muons. Figure A-4 shows the same set of plots for the triggered electron and the tagged muon pairs.

The number triggered μ and tagged μ pairs and the number of triggered μ and predicted fake muon pairs are listed in the tables A-1 for the SECVTX-tagged single-muon data. Table A-2 lists the same numbers for the SECVTX-

Table A-1. Number of triggered μ and tagged μ pairs and number of triggered e and expected fake μ pairs for the SECVTX-tagged single μ sample

	same side		opposite side	
	tag	expected fake	tag	expected fake
same sign	123	90 ± 10.0	165	49.1 ± 4.2
opposite sign	873	148.2 ± 10.6	307	51.4 ± 3.7

Table A-2. Number of triggered e and tagged μ pairs and number of triggered μ and expected fake μ pairs for the SECVTX-tagged single e sample

	same side		opposite side	
	tag	expected fake	tag	expected fake
same sign	61	44.6 ± 4.2	181	44.0 ± 3.8
opposite sign	465	55.0 ± 5.1	340	47.3 ± 4.5

tagged single-electron data. The same side and the opposite side pairs are defined as follows;

- Same side : mass(triggered ℓ + tagged μ) < 5 GeV/c^2.
- Opposite side : mass(triggered ℓ + tagged μ) > 5 GeV/c^2.

The contribution to the triggered lepton and the tagged muon pair due to the tagged muons from the other B in the event is discussed in sub-section A-B-4.

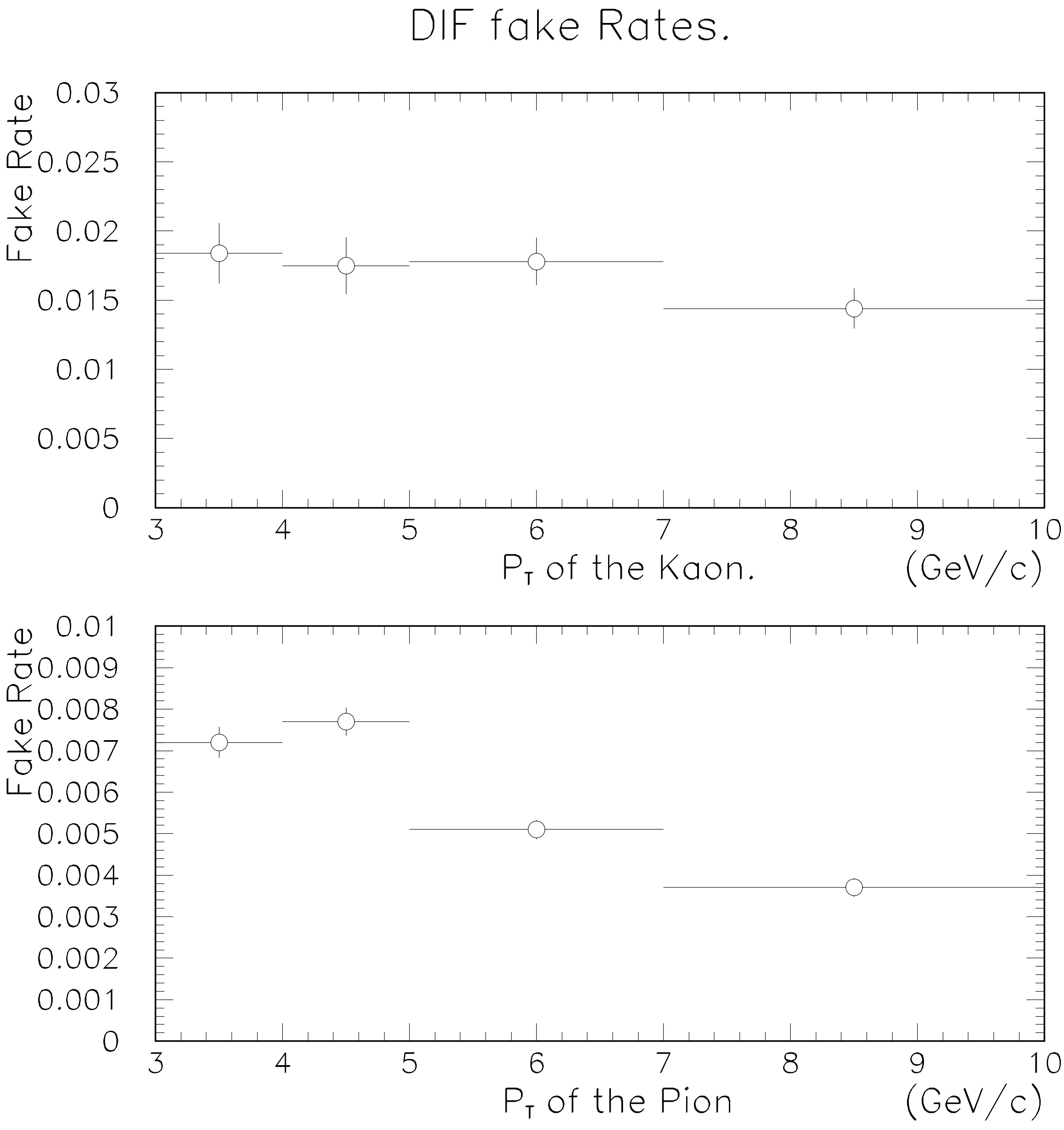

Figure A-2. (a) The probability for a kaon to be identified as a muon due to decay in flight (b) The probability for a pion to be identified as a muon due to decay in flight.

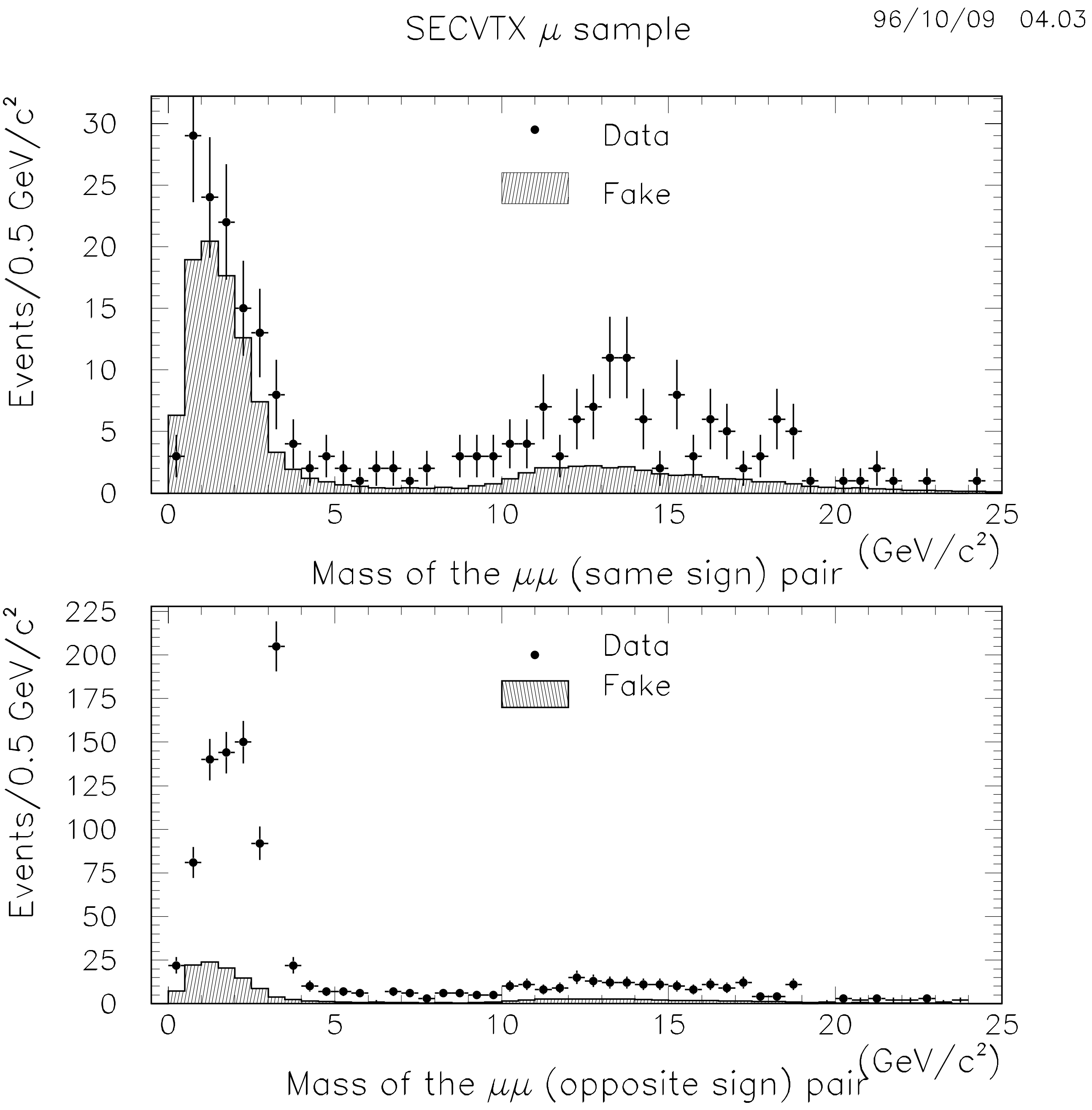

Figure A-3. (a) The mass distribution of the same sign triggered μ and tagged μ pairs from data and the predicted fake μ contribution to it. (b)The mass distribution of the opposite sign triggered μ and tagged μ pairs and the predicted fake μ contribution to it.

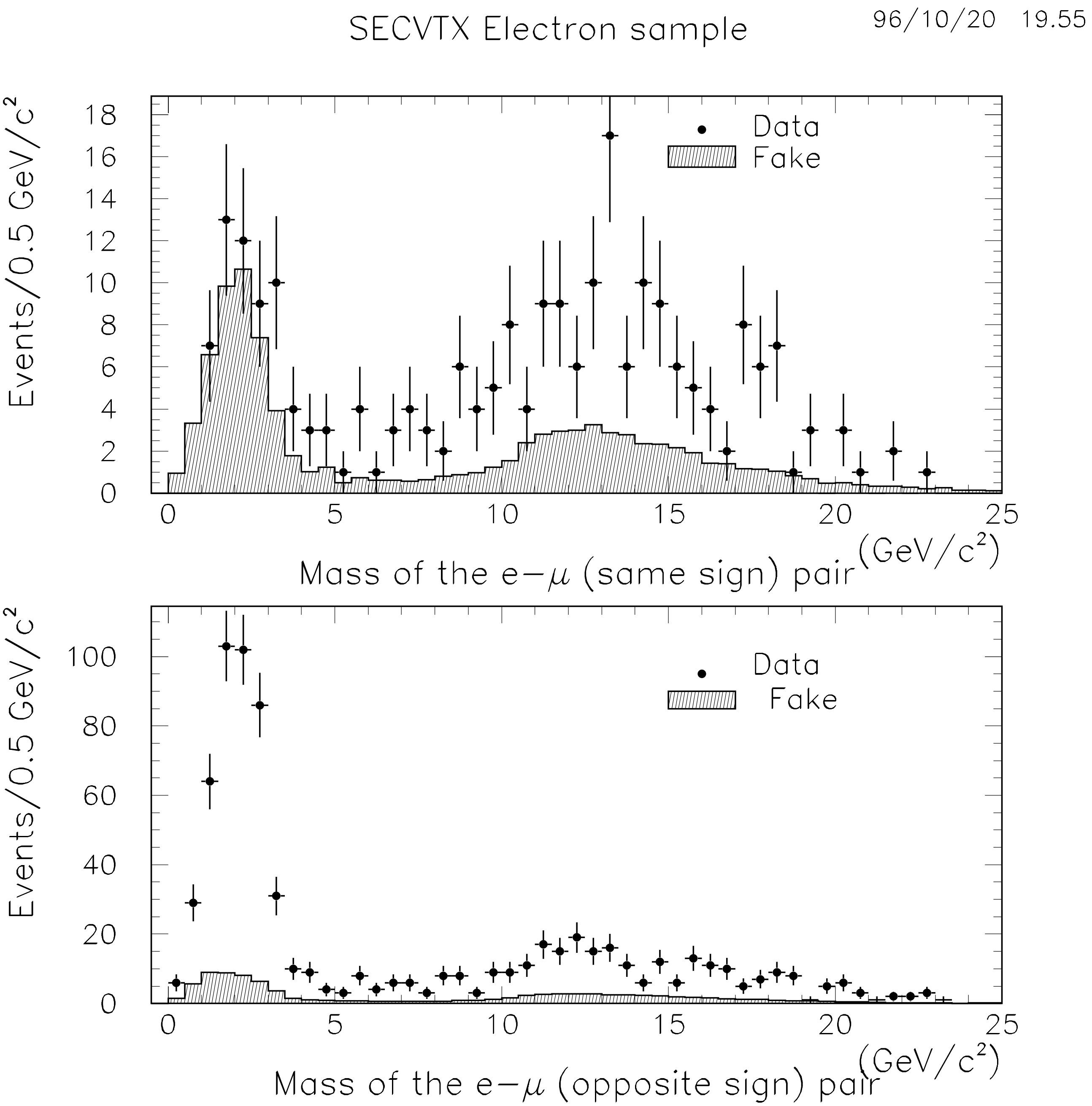

Figure A-4. (a) The mass distribution of the same sign triggered e and tagged μ pairs from data and the predicted fake μ contribution to it. (b)The mass distribution of the opposite sign triggered μ and tagged μ pairs and the predicted fake μ contribution to it.

3. The K and π Fractions

A very crucial element of the estimates of the fake muons described above is the K and the π fractions in the data sample; where the K fraction is $= N_K/(N_K + N_\pi)$ and π fraction is $= N_\pi/(N_K + N_\pi)$. For the purpose of this analysis the K and the π fraction was determined from Monte Carlo simulation. $B\bar{B}$ events were generated using PYTHIA and were decayed using CLEOMC. The events were required to pass the single-lepton trigger filter and were simulated through the detector using QFL. The tracks in the simulated data were identified as kaons and pions by matching their P_t with kaons and pions at the generator level. For the same sign pair the π fraction for tracks with $P_t > 3.0$ GeV/c was .72±.04 and for the opposite sign it was $.83 \pm .04$.

We check the K and the π fraction obtained from CLEO Monte Carlo using the dE/dx distribution in data. We used the most recent version of the code to get the dE/dx distribution [63]. The expected charge in the CTC (QCTC) for the pion hypothesis was subtracted from the expected QCTC for the electron and the kaon hypothesis. The difference for the two cases was divided by the expected QCTC width for the pions, and the results were plotted as a histogram for three momentum bins. The histograms were fitted to Gaussians and their mean and RMS width (σ) were noted. Next, the difference of the observed QCTC for the tracks in data and the expected QCTC for the pion hypothesis divided by the expected QCTC width for the pions was plotted as a histogram. This histogram was fitted to three Gaussians; the mean and sigma of one was fixed to 0.0 and 1.0 respectively (for the pions). The mean and sigma of the other two Gaussians were fixed to the means and $(1^2 + \sigma^2)^{.5}$ respectively from the fits done earlier. This was done for three momentum bins (3-4 GeV/c, 4-6 GeV/c and 6-10 GeV/c.). Figure A-5 shows the fits for the same sign pairs for the three momentum bins. Figure A-6 shows the fits for the opposite sign pairs for the three momentum bins. The π fraction for the three momentum bins for the two cases are listed in Table A-3.

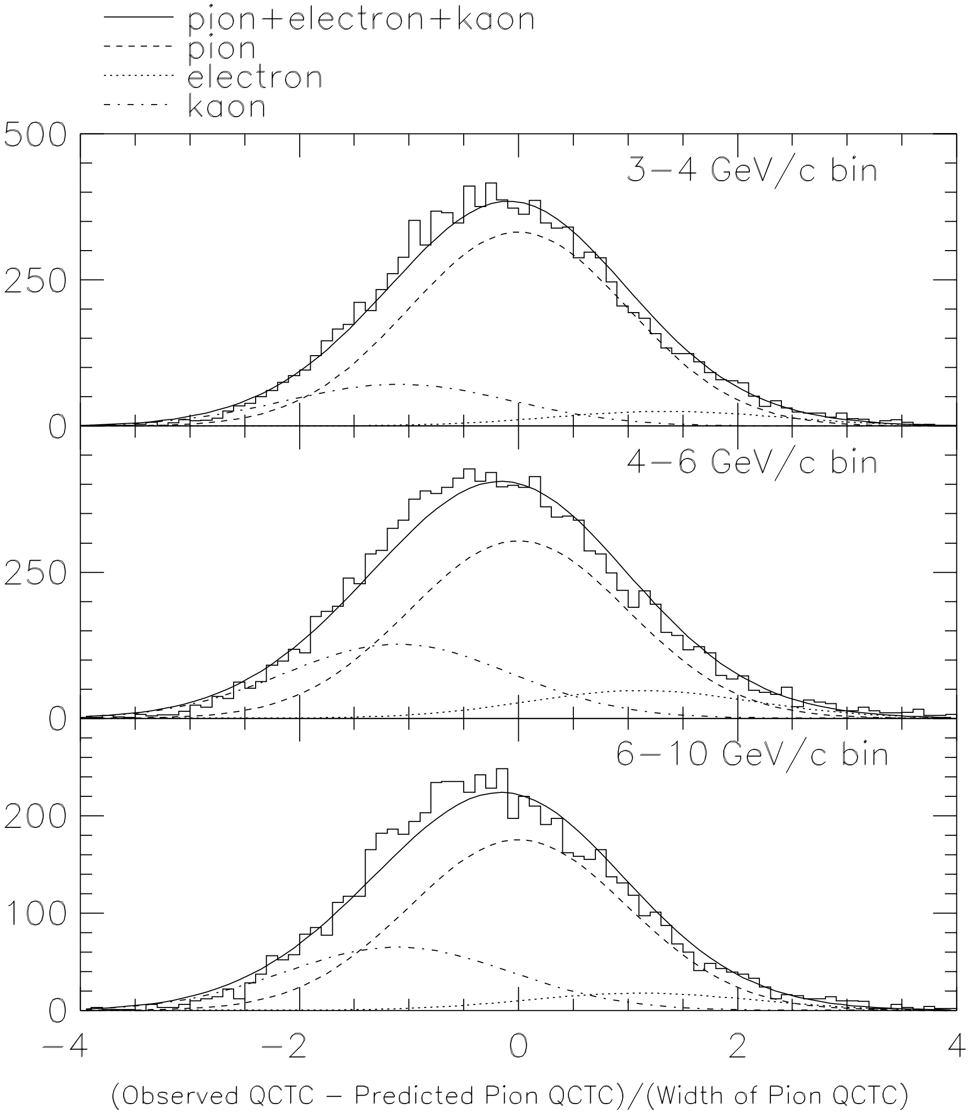

Figure A-5. dE/dx plot for same sign pairs for momentum for 3-4, 4-6, and 6-10 GeV/c momentum bins.

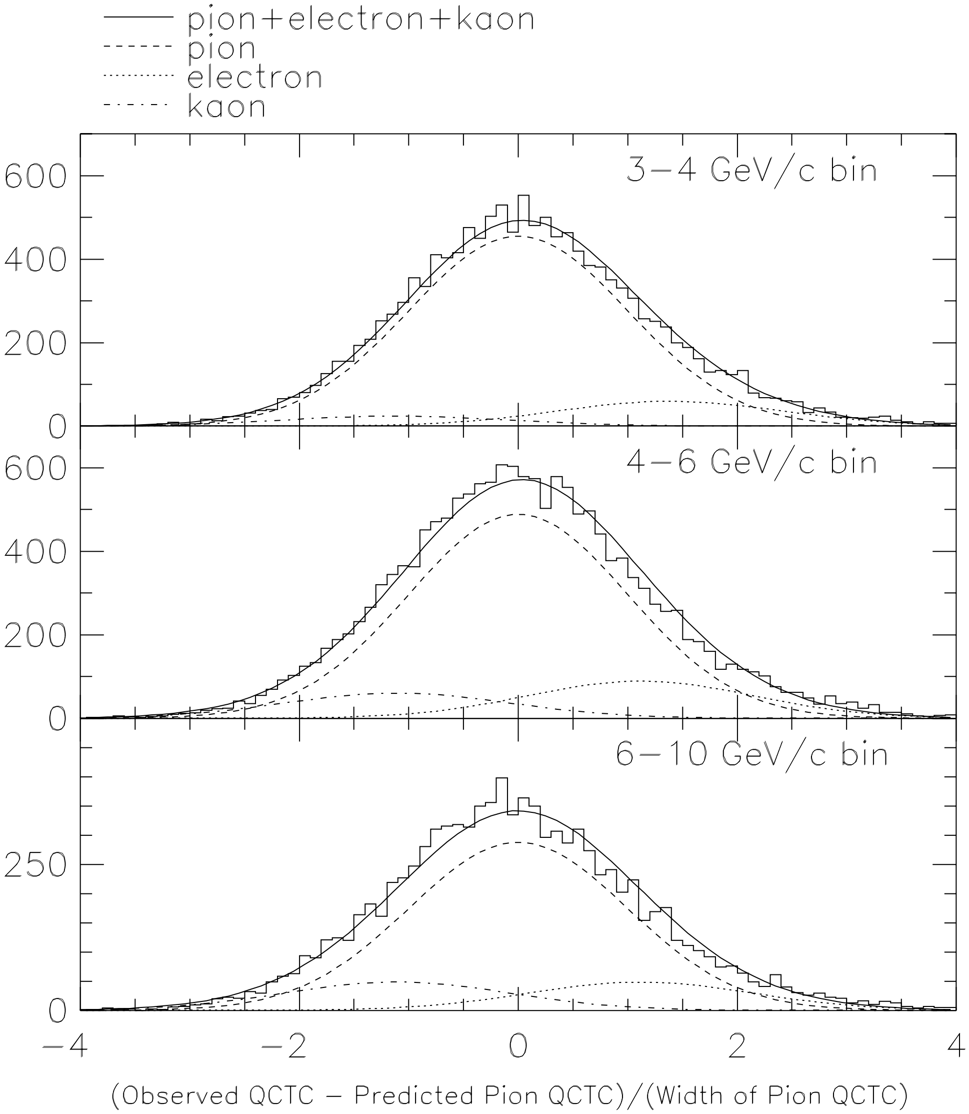

Figure A-6. dE/dx plot for opposite sign pairs for momentum for 3-4, 4-6, and 6-10 GeV/*c* momentum bins.

Table A-3. π Fraction from dE/dx plots for the opposite sign and and same sign pairs for different momenta. The π fraction is defined as $N_\pi/(N_K + N_\pi)$.

	π Fraction 3-4 GeV/c bin	π Fraction 4-6 GeV/c bin	π Fraction 6-10 GeV/c bin
Opposite Sign	0.95±.01	0.89±.01	0.79±.02
Same Sign	0.82±.01	0.70±.01	0.69±.02

4. Contribution from $B\bar{B}$

The contribution to the triggered and the tagged lepton pair due to the tagged lepton from the other B in the event was studied using $b\bar{b}$ Monte Carlo generated from BGENERATOR. We set the minimum $\mathrm{P}_t(b) > 8$ GeV/c in BGENERATOR. The B mesons were decayed by CLEO. Mixing of neutral B mesons was turned on using $x_d = 0.71$ and $x_s = 10$. Events with lepton $\mathrm{P}_t > 6$ GeV/c were selected at the generator level using the ELEFILT module or the MUOFILT module [61]. These filter modules simulate the 7.5 GeV/c CFT threshold curve of the Level 2. The selected events were simulated through the detector using QFL. The SECVTX options for this data set were changed as follows

- cone size of JETS cluster : 1.0
- cone size for tracks to be vertexed : 0.7
- E_T(jet) > 10 GeV
- $L_{xy}/\sigma_{L_{xy}} > 2$.

5. Normalization of Monte Carlo Events

The Monte Carlo was normalized to data using the triggered and tagged lepton invariant mass above 5 GeV/c. The normalization factor F can be written as

$$F = \frac{(N^{SS}_{tag} - N^{SS}_{fake}) + (N^{OS}_{tag} - N^{OS}_{fake})}{N^{SS}_{MC} + N^{OS}_{MC}}. \tag{A-1}$$

where N_{MC} is the number of events contained in the Monte Carlo sample. N_{tag} is the number of tags and N_{fake} is the number of expected fake events in the data. ^{SS} and ^{OS} mean the same sign and the opposite sign, respectively. All these number are for the opposite side pairs (i.e. M(trig. l and tagged l) > 5 GeV/c^2).

C. Final Results

The total number of the predicted lepton pairs for a particular data set is obtained by adding the fake and the $B\bar{B}$ predictions for that set. Figure A-7a shows the fake μ and the fake μ + $B\bar{B}$ contribution for the same-sign pairs and Fig. A-7b shows the same for the opposite-sign pairs for the single-muon sample. Figure A-8 shows the same set of plots for the single-electron sample. Table A-4 shows the expected fake μ plus the $B\bar{B}$ contribution to the same side case for the SECVTX-tagged single-electron and single-muon data sets. The number of pairs with the same sign from data match the predicted number with in the given errors. This shows that we estimate the muon fake rate correctly. The number of pairs with opposite sign from data do not match the predictions. This is probably due to the fact that the sequential decay of the charm particles are not simulated correctly in our Monte Carlo programs. The disagreement does not show any inconsistency in the fake rate calculations.

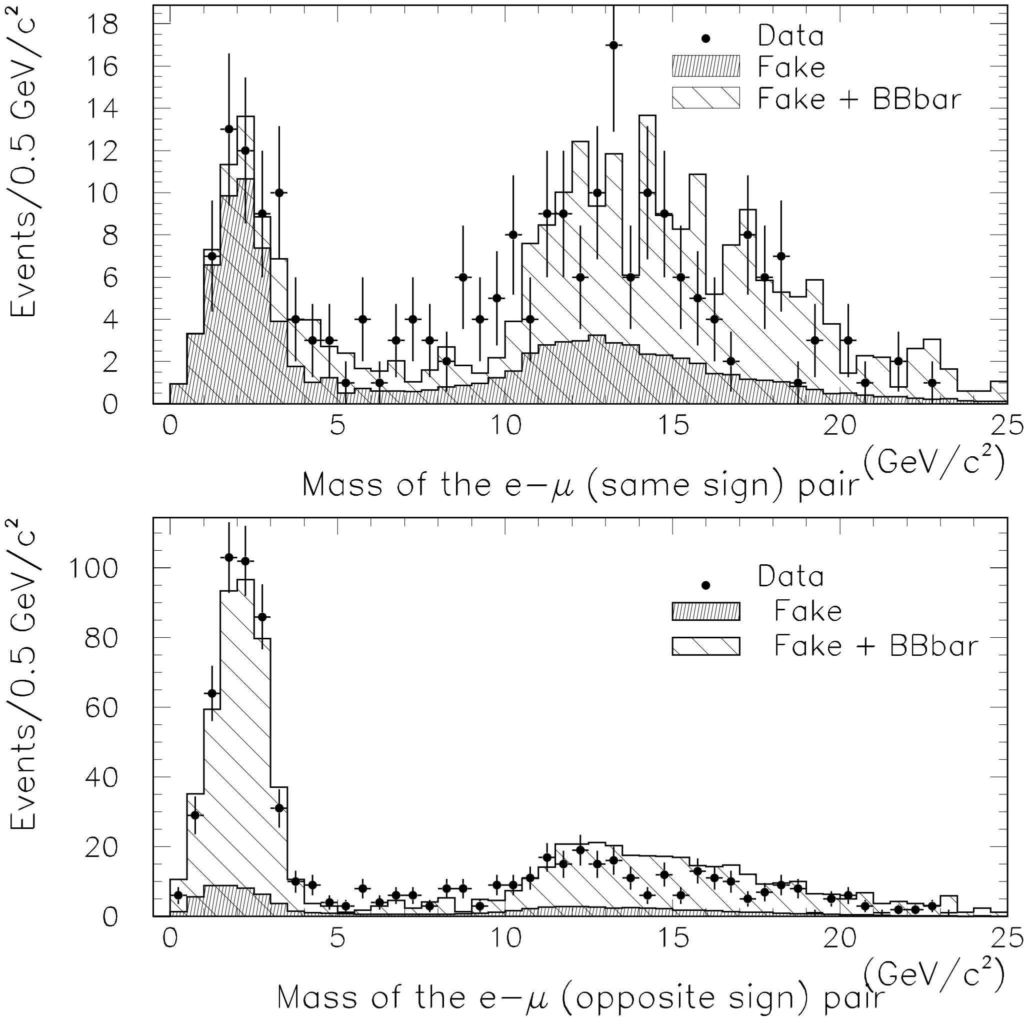

Figure A-7. Mass distribution of the triggered lepton(e) + tagged μ in SECVTX-tagged single e sample. The shaded histograms in the plots show the contribution from fake μ and fake μ plus $B\bar{B}$ (a) for same sign pair and (b) for opposite sign pair.

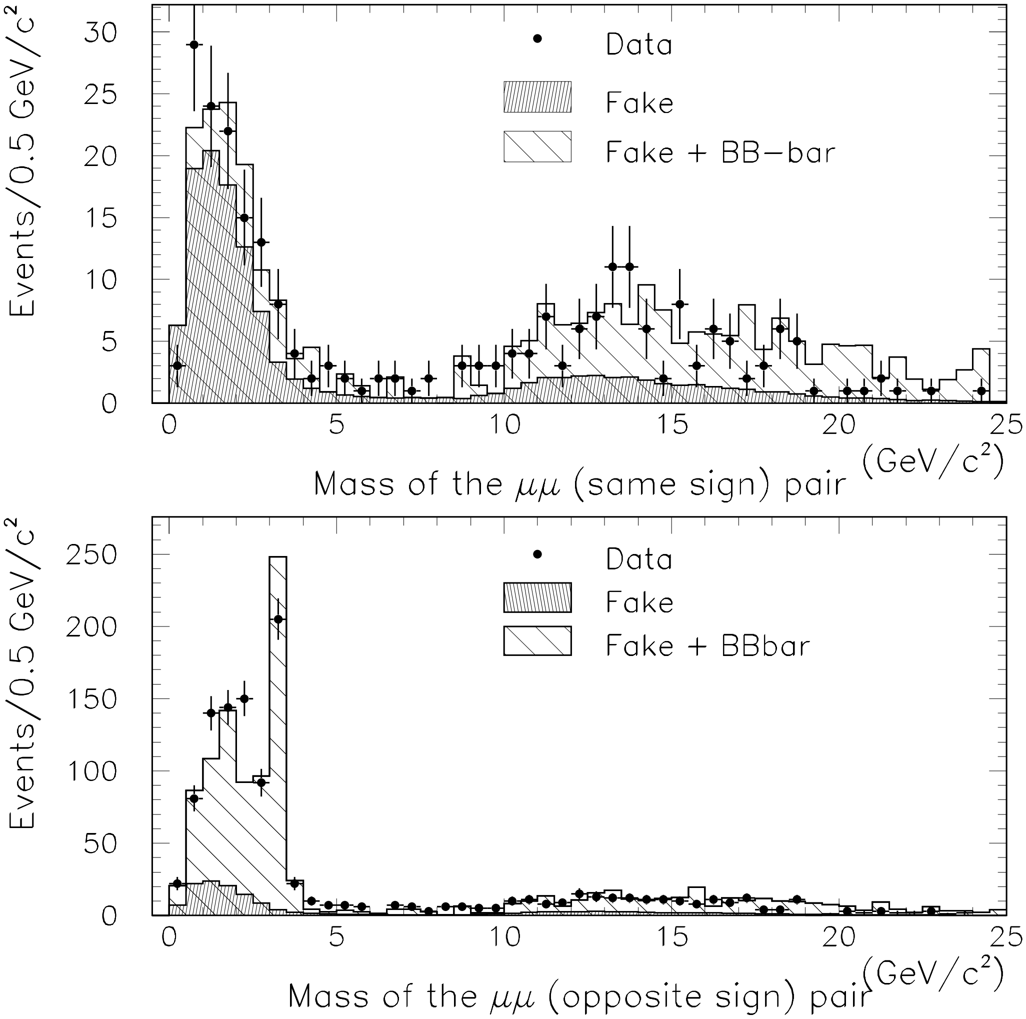

Figure A-8. Mass distribution of the triggered lepton(μ) + tagged μ in SECVTX-tagged single μ sample. The shaded histograms in the plots show the contribution from fake μ and fake μ plus $B\bar{B}$ (a) for same sign pair and (b) for opposite sign pair.

Table A-4. The number of same side triggered lepton and tagged μ pairs and the number of expected same side pairs of triggered lepton and fake μ plus pairs from $B\bar{B}$ contribution for the single-e and single-μ data sets.

	single-e sample		single-μ sample	
	tag	expected fake + $b\bar{b}$	tag	expected fake+ $b\bar{b}$
same sign	61	59.9 ± 5.7	123	119.5 ± 12.8
opposite sign	465	424.0 ± 24.4	873	770.0 ± 58.5

.

BIBLIOGRAPHY

[1] Eichten E et al. *Phys. Rev. D* **17** 3090 (1979), **21** 203 (1980)

[2] Godfrey S, Isgur N *Phys. Lett. B* **32** 189 (1985)

[3] Richardson J L *Phys. Lett. B* **82** 338 (1979)

[4] Martin A *Phys. Lett. B* **93** 338 (1980)

[5] Quigg C, Rosner J L *Phys. Lett. B* **71** 153 (1977)

[6] Buchmüller W, Tye S-H H *Phys. Rev. D* **24** 132 (1981)

[7] Shifman M A et al. *Nucl. Phys. B* **24** 345,448 (1979)

[8] Rienders L J et al. *Phys. Rep.* **127** 1 (1985)

[9] Narison S. *Phys. Lett. B* **198** 104 (1987)

[10] Dominguez C A et al. *Phys. Lett. B* **197** 423 (1987), **199** 596 (1987)

[11] Shuryak E V *Nucl. Phys. B* **198** 83 (1982)

[12] Aliev T M et al. *Sov. J. Nucl. Phys.* **38** 936 (1983)

[13] Reinders L J *Phys. Rev. D* **38** 947 (1988)

[14] Shifman M A *Sov. Phys. Uspekhi* **30** 91 (1987)

[15] Eichten E; Preprint FERMILAB-Conf-85/29-T (1985)

[16] Kwong W, Rosner J L *Phys. Rev. D* **38** 279 (1988)

[17] Eichten E J, Quigg C; Preprint FERMILAB-PUB-94/032-T

[18] Richardson J *Phys. Lett. B* **82** 272 (1979)

[19] Kwong W, Rosner J L *Phys. Rev. D* **44** 212 (1991)

[20] Particle Data Book *Phys. Rev. D* **45** S1 (1992)

[21] Eichten E J, Feinberg F *Phys. Rev. Lett* **23** 2724 (1981)

[22] Gershtein S S, et al. *Sov. J. Nucl. Phys.* **48** 327 (1988)

[23] Chen Y-Q, Kuang Y-P *Phys. Rev. D* **46** 1165 (1992)

[24] Gershtein S S, et al. *Phys. Usp.* **38** 1 (1995) also avalable as preprint hep-ph/9504319

[25] Lusignoli M, Masetti M *Z. Phys. C* **51** 549 (1991)

[26] Metzler S, et al.; CDF document CDF/ANAL/BOTTOM/CDFR/3541, submitted to PRL

[27] Marchesini G. et al. Available as hep-ph/9607393 on LANL preprint server

[28] Lusignoli M, et al. *Phys. Lett. B* **266** 142 (1991)

[29] Mesetti M, Sartogo F; Preprint hep-ph/9503491

[30] Berezhnoy A V et al.; Preprint hep-ph/9504302

[31] Kolodziej K, et al. *Phys. Lett. B* **355** 337 (1995)

[32] Chang C-H, et al.; Preprint hep-ph/9602411

[33] Chang C-H, et al. *Phys. Lett. B* **364** 78 (1995)

[34] Bauer G, et al.; CDF document CDF/ANAL/BOTTOM/CDFR/3561

[35] Alexopoulos T., et al. *Phys. Rev. D* **48** 984 (1993)

[36] Abe F et al. *Phys. Rev. Lett.* **73** 225 (1994)

[37] Abe F et al. *Phys. Rev. D* **50** 2966 (1995)

[38] Abe F et al. *Nucl. Instrum. Meth.* **A271** 387 (1988)

[39] Amidei D et al. *Nucl. Instrum. Meth.* **A350** 73 (1994)

[40] Laasko M et al. *Nucl. Instrum. Meth.* **A326** 214 (1993)

[41] Azzi P, et al.; Radiation Damage Esperience at CDF with SVX , Proceedings of the International Symposium on Development and Application of Semiconductor Tracking Detectors (Hiroshima, Japan October 10-13, 1995)

[42] Kajfasz E in the Proceedings of Third International Workshop on Vertex Detectors, May 1994, Lake Monroe, Indiana, USA

[43] DeJongh F, Hans R; CDF document CDF/ANAL/TRIG/CDFR/1999

[44] Marriner J; CDF document CDF/DOC/SECVTX/PUBLIC/1996

[45] Sphicas P; CDF document CDF/DOC/BOTTOM/CDFR/2655

[46] Nason P, et al. *Nucl. Phys.* **B303** 607(1988) and *Nucl. Phys.* **B327** 49 (1988)

[47] Mangano M et al. *Nucl. Phys.* **B373** 295 (1992)

[48] Lewis J D; CDF document CDF/DOC/MONTECARLO/PUBLIC/2724

[49] Isgur N, et al. *Phys. Rev. D* **39** 799 (1989)

[50] Shapiro M; CDF document CDF/ANAL/MONTECARLO/PUBLIC/1810

[51] Stephan P P; CDF document CDF/ANAL/TRIGGER/CDFR/3070

[52] Singh P P; CDF document CDF/ANAL/BOTTOM/CDFR/3393

[53] Smith D; Ph.D. Thesis, University of Illinois (1989)

[54] Carroll A S et al. *Phys Lett* **B80** 319 (1979)

[55] Denisov S P et al. *Nucl. Phys.* **B61** 62 (1973)

[56] CDF document SIMGUIDE.MEM

[57] Alexopoulos T et al. *Phys. Rev. Lett* **64** 991 (1990)

[58] Suzuki J, Kim S; CDF document CDF/ANAL/BOTTOM/CDFR/3287

[59] Zech G *Nucl Instm. Meth.* **A277** 608 (1989)

[60] Anyway-Wiese C; Ph.D. Thesis UCLA, May 1995

[61] Paulini M, et al.; CDF document CDF/ANAL/BOTTOM/CDFR/3757

[62] Yao W, et al. CDF document CDF/ANAL/SEC_VTX/CDFR/2716

[63] Peters M. D.; CDF document CDF/ANAL/BOTTOM/CDFR/3807